

AD-A129 794

TIME DOMAIN TECHNIQUES IN THE SINGULARITY EXPANSION
METHOD(U) VIRGINIA POLYTECHNIC INST AND STATE UNIV
BLACKSBURG W A DAVIS ET AL. MAY 83 AFWL-TR-82-156

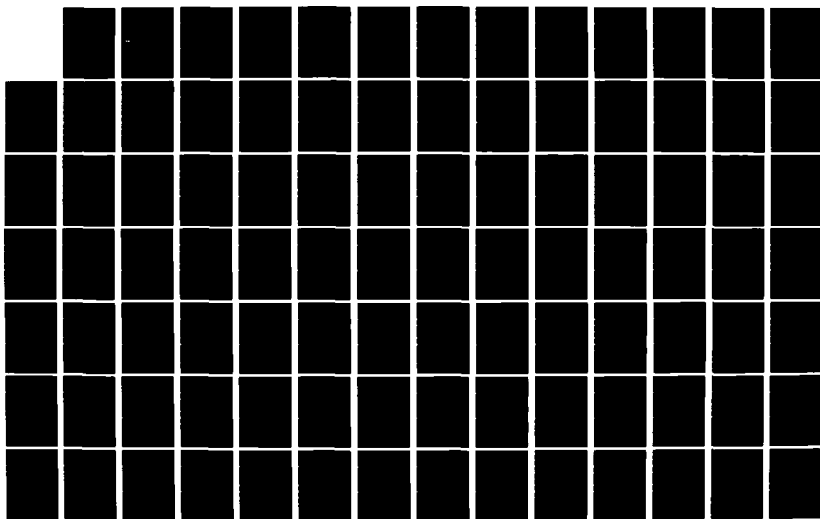
1/2

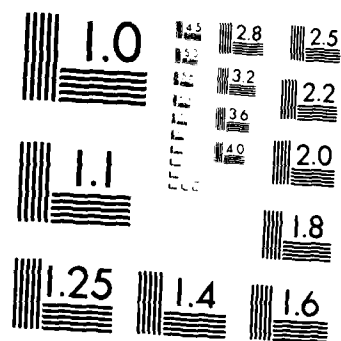
UNCLASSIFIED

F29601-81-K-0019

F/G 12/1

NL





MICROCOPY RESOLUTION TEST CHART
NATIONAL BUREAU OF STANDARDS-1963-A

ADA 129794

TIME DOMAIN TECHNIQUES IN THE SINGULARITY EXPANSION METHOD

W. A. Davis
D. J. Riley

Virginia Polytechnic Institute & State University
Blacksburg, VA 24061

May 1983

Final Report

Approved for public release; distribution unlimited.



DMC FILE COPY

AIR FORCE WEAPONS LABORATORY
Air Force Systems Command
Kirtland Air Force Base, NM 87117

83 06 27 037

AFWL-TR-82-156

This final report was prepared by the Virginia Polytechnic Institute and State University, Blacksburg, Virginia under Contract F29601-81-K-0019, Job Order 37630144 with the Air Force Weapons Laboratory, Kirtland Air Force Base, New Mexico. Mr William D. Prather (NTAA) was the Laboratory Project Officer-in-Charge.

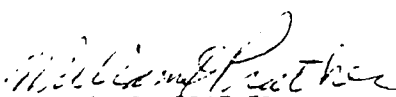
When Government drawings, specifications, or other data are used for any purpose other than in connection with a definitely Government-related procurement, the United States Government incurs no responsibility or any obligation whatsoever. The fact that the Government may have formulated or in any way supplied the said drawings, specifications, or other data, is not to be regarded by implication, or otherwise in any manner construed, as licensing the holder, or any other person or corporation; or as conveying any rights or permission to manufacture, use, or sell any patented invention that may in any way be related thereto.

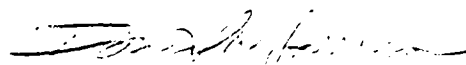
This report has been authored by a contractor of the United States Government. Accordingly, the United States Government retains a nonexclusive, royalty-free license to publish or reproduce the material contained herein, or allow others to do so, for the United States Government purposes.

The Public Affairs Office has reviewed this report, and it is releasable to the National Technical Information Service, where it will be available to the general public, including foreign nationals.

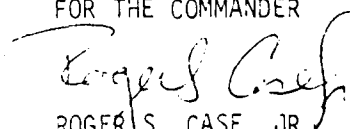
If your address has changed, if you wish to be removed from our mailing list, or if your organization no longer employs the addressee, please notify AFWL/NTAA, Kirtland AFB, NM 87117 to help us maintain a current mailing list.

This report has been reviewed and is approved for publication.


WILLIAM D. PRATHER
Project Officer


DAVID W. GARRISON
Lt Colonel, USAF
Chief, Applications Branch

FOR THE COMMANDER


ROGER S. CASE, JR
Lt Colonel, USAF
Chief, Aircraft and Missiles Division

DO NOT RETURN COPIES OF THIS REPORT UNLESS CONTRACTUAL OBLIGATIONS OR NOTICE ON A SPECIFIC DOCUMENT REQUIRES THAT IT BE RETURNED.

UNCLASSIFIED

SECURITY CLASSIFICATION OF THIS PAGE (When Data Entered)

REPORT DOCUMENTATION PAGE		READ INSTRUCTIONS BEFORE COMPLETING FORM
1. REPORT NUMBER AFWL-TR-82-156	2. GOVT ACCESSION NO.	3. RECIPIENT'S CATALOG NUMBER
4. TITLE (and Subtitle) TIME DOMAIN TECHNIQUES IN THE SINGULARITY EXPANSION METHOD	5. TYPE OF REPORT & PERIOD COVERED Final Report	
	6. PERFORMING ORG. REPORT NUMBER	
7. AUTHOR(s) W. A. Davis D. J. Riley	8. CONTRACT OR GRANT NUMBER(s) F29601-81-K-0019	
9. PERFORMING ORGANIZATION NAME AND ADDRESS Virginia Polytechnic Institute & State University Blacksburg, VA 24061	10. PROGRAM ELEMENT, PROJECT, TASK AREA & WORK UNIT NUMBERS 64711F/37630144	
11. CONTROLLING OFFICE NAME AND ADDRESS Air Force Weapons Laboratory (NTAA) Kirtland Air Force Base, NM 87117	12. REPORT DATE May 1983	
	13. NUMBER OF PAGES 140	
14. MONITORING AGENCY NAME & ADDRESS (if different from Controlling Office)	15. SECURITY CLASS. of this report Unclassified	
	15a. DECLASSIFICATION/DOWNGRADING SCHEDULE	
16. DISTRIBUTION STATEMENT (of this Report) Approved for public release; distribution unlimited.		
17. DISTRIBUTION STATEMENT (of the abstract entered in Block 20, if different from Report)		
18. SUPPLEMENTARY NOTES		
19. KEY WORDS (Continue on reverse side if necessary and identify by block number) Singularity Expansion Method SEM Interaction and Coupling Electromagnetic Theory		
20. ABSTRACT (Continue on reverse side if necessary and identify by block number) The use of the singularity expansion method (SEM) to calculate the time-domain response of an object to an incident electromagnetic wave has shown the promise of being extremely useful. However, the work to date has been hindered by the requirement for very large matrices which limited the application to one-dimensional geometries with relatively few unknowns. This study extends the applicability of time domain SEM to two dimensions and extends numerical time-domain techniques in general.		

DD FORM 1473

EDITION OF 1 NOV 55 IS OBSOLETE

UNCLASSIFIED

SECURITY CLASSIFICATION OF THIS PAGE (When Data Entered)

TABLE OF CONTENTS

<u>Chapter</u>	<u>page</u>
I. INTRODUCTION	1
II. FUNDAMENTAL INTEGRAL EQUATIONS OF ELECTROMAGNETICS	5
Introduction	5
Mathematical Formalism	6
III. FUNDAMENTAL CONCEPTS OF THE SINGULARITY EXPANSION METHOD	14
Introduction	14
Space-Frequency Techniques	16
Natural Frequencies and Modes	16
Coupling Coefficients and Entire Functions	18
Space-Time Techniques	21
Natural Frequencies, Natural Modes, and Stability Considerations	21
Coupling Coefficients	33
IV. EIGENSOLUTION METHODS FOR THE TRANSITION MATRIX	39
Introduction	39
Root Searching Methods	41
Muller's Method	42
Contour Integration	45
Polynomial Matrix Reduction	47
Laguerre's Method	49
Matrix Eigenvalue Methods	51
Similarity Transform Methods	51
The LR Transformation	52
The QR Transformation	54
Iterative Eigenvector Methods	56
Single Vector Power Methods	57
Multiple Vector Power Methods	60
V. WIRE-STRUCTURE ANALYSIS	68
Introduction	68
Space-Frequency Techniques	69
Excitation Models	75
Thin-Wire Kernel Approximation	73

Electric Field Distribution	73
Space-Time Techniques	79
Transient Current Response	85
TD-SEM Pole Distribution	85
Effect of Varying the Time Sampling	
Distance	93
Pole Shift by Kernel Decoupling	96
VI. TRANSIENT ANALYSIS OF THIN, PERFECT CONDUCTING	
RECTANGULAR PLATES	99
Introduction	99
Mathematical Formalism	101
Standard Gridding Scheme	107
Shifted Gridding Scheme	115
TD-SEM Pole Distribution	119
VII. CONCLUSIONS	128
REFERENCES	131

TABLE OF FIGURES

	<u>page</u>
Figure 5.1: Wire geometry.	70
Figure 5.2: Current distribution on a 2 meter dipole antenna with a radius of 0.01 meters. The number of unknowns was 31, and the frequency of operation was 75 MHz. . . .	77
Figure 5.3: Effect of the exact and approximate kernels on the current distribution of a 1 meter antenna with a radius of 0.02 meters. The number of unknowns was 49, and the frequency of operation was 214.3 MHz.	80
Figure 5.4: Scattered tangential electric field distribution of a 1 meter antenna with a radius of 0.02 meters. The number of unknowns was 19, and the frequency of operation was 209.8 MHz.	81
Figure 5.5: Transient current distribution on one of two feed segments of a 1 meter antenna with a radius of 0.00754 meters. The number of unknowns was 22.	86
Figure 5.6: Pole distribution for 18 unknowns. The length of the scatterer was 1 meter, and the radius was 0.005 meters.	88
Figure 5.7: Eigenvalue structure for 18 unknowns. The length of the scatterer was 1 meter, and the radius was 0.005 meters.	90
Figure 5.8: First layer pole distribution found by S. I. for 32 unknowns. The scatterer was 1 meter in length, and the radius was 0.005 meters.	91
Figure 5.9: Execution time requirements on an IBM 3032 computer using FORTRAN H EXTENDED (OPT=2) for various eigensolution methods.	92
Figure 5.10: Storage requirements for various eigensolution methods.	94

Figure 5.11:	Pole movement due to kernel decoupling. The scatterer was 1 meter in length with a radius of 0.005 meters. The number of unknowns was 10.	98
Figure 6.1:	Plate geometry.	102
Figure 6.2:	Annular propagation of active regions due to the time difference ($p-p'$). . .	104
Figure 6.3:	Standard gridding scheme.	108
Figure 6.4:	Current density component corresponding to the direction of incident polarization calculated on the center patch of a 1 meter square plate. No boundary conditions have been enforced. A standard gridding scheme has been used with 16 patches for each current component. The pulse width was 4.9 light meters, and the choice $c\Delta t=0.7\Delta$ was made.	111
Figure 6.5:	Current density component corresponding to the direction of incident polarization calculated on the center patch of a 1 meter square plate. The normal component of the current density has been set to zero at the edges. A standard gridding scheme has been used with 16 patches for each current component. The width of the incident pulse was 4.9 light meters, and the choice $c\Delta t=0.7\Delta$ was made.	112
Figure 6.6:	Current density component corresponding to the direction of incident polarization calculated on the center patch of a 1 meter square plate. Normal components of the current density have been set to zero at the edges; parallel components have been extrapolated at the edges. A standard gridding scheme has been used with 16 patches for each current component. A comparison has been made with Bennett's model. The incident pulse was 4.9 light meters wide, and the choice $c\Delta t=0.7\Delta$ was made.	113
Figure 6.7:	Shifted gridded scheme.	116

- Figure 6.8: Unstable current density distribution obtained from the shifted gridding scheme for $c\Delta t=\Delta$. The component corresponding to the direction of incident polarization on the center patch is shown. A total of 12 patches have been used for each current density component. 120
- Figure 6.9: Current density component corresponding to the direction of incident polarization calculated on the center patch of a 1 meter square plate. A shifted gridding scheme has been used with 12 patches for each current component. The incident pulse was 4.9 light meters wide, and a comparison with the standard grid model has been made. 121
- Figure 6.10: Poles for a 1 meter square plate discretized with a shifted gridding scheme. The total number of patches for each component of the current density was 2, and the choice $c\Delta t=0.7\Delta$ was made. 122
- Figure 6.11: Poles for a 1 meter square plate discretized with a shifted gridding scheme. The total number of patches for each component of the current density was 6, and the choice $c\Delta t=0.7\Delta$ was made. 123
- Figure 6.12: Poles for a 1 meter square plate discretized with a shifted gridding scheme. The total number of patches for each component of the current density was 12, and the choice $c\Delta t=0.7\Delta$ was made. 124
- Figure 6.13: Comparison of TD-SEM poles (shifted grid, 12 patches for each current density component, and $c\Delta t=0.7\Delta$) with available frequency-domain poles. The results are for a 1 meter square plate. 127

Chapter I

INTRODUCTION

The calculation of natural frequencies (poles) and natural modes (free oscillations) of structures is a fundamental problem of many disciplines. Until recently, the mathematical study of these parameters has unfortunately been limited to canonic geometries which lend themselves to eigensolution by separation of variable techniques. The singularity expansion method (SEM) removes this geometrical restriction by enabling one to obtain the natural frequencies and natural modes of an arbitrary object. The SEM also enables one to determine the response of the object to an arbitrary forcing function directly from an appropriate expansion of the modal and pole structure.

The basic theoretical foundations of the SEM were initially presented using frequency-domain techniques applied to electromagnetic equations by Baum [1]. Baum's development was subsequently extended by Marian and Latham [2]; and rigorous mathematical justification of some of the basic foundations has recently been presented by Ramm [3]. Analytic frequency-domain SEM results for the perfect conducting spherical scatterer were originally obtained by Baum [1], and numerical frequency-domain results for thin, per-

fect conducting cylindrical surfaces were initially presented by Tesche [4].

Interest in time-domain techniques in the SEM has not been as widespread as frequency-domain methods; however, several varied contributions have recently been made toward establishing the versatility of time-domain methods. A time-domain method analogous to the original frequency-domain method may be found in Baum [5]. The applicability of this method, however, has been somewhat limited due to the level of difficulty of the describing equations. Van Blaricum and Mittra [6] developed a rather unique method whereby the natural responses may be obtained using Prony's method [7] once the transient response of the object is known. An obvious complication with this method is that the determination of the transient response can be a non-trivial problem. An alternate time-domain method which sidesteps the complications of the above methods has been introduced by Cordaro and Davis [8]. This method, known as time-domain SEM (TD-SEM), enables one to find the natural responses directly from the finite-difference representation of the governing integral equations cast in a matrix eigenvalue form. Unfortunately, the matrices generated tend to be quite large, and hence the previous work has been limited to one-dimensional geometries discretized with relatively few unknowns. The

results which have been obtained, however, indicate that the Cordaro-Davis method is capable of producing a great deal of information quite efficiently. The intent of this study is to extend the applicability of TD-SEM, and extend numerical time-domain techniques in general.

Toward establishing this intent, the following (principal) set of tasks are defined: (1) determine stability criteria for various finite difference representations of electromagnetic equations, (2) develop simple time-domain expressions for determining the SEM coupling coefficients (these are parameters which couple the natural frequencies and modes to the incident forcing function), (3) develop an eigensolution algorithm which will solve the large scale matrices generated by TD-SEM, (4) obtain a pole distribution for the linear scatterer discretized with a large number of unknowns, (5) apply TD-SEM to the two-dimensional rectangular plate problem. The outline for establishing these tasks is as follows.

The fundamental governing equations of electromagnetics are developed in integral form in Chapter 2 using dyadic Green's function theory. The equations are initially developed in general, and are then specialized to describe thin, perfect conducting surfaces. An effort has been made to keep the development brief by leaving several intermediate

steps to the references. This is done since the application and solution of the final results is the principal intent of this work and not the mathematical subtleties of the development.

The basic concepts of the frequency-domain SEM and the time-domain method of Cordaro and Davis are presented in Chapter 3. Numerical solution techniques and stability techniques for the time-domain equations are also presented. The stability discussion, as applied to these equations, is presented for the first time.

A variety of eigensolution methods applicable to the matrices generated by the Cordaro-Davis method are presented in Chapter 4. The discussion culminates with the development of an eigensolution algorithm for large matrices in block companion form.

The techniques developed in the previous chapters are applied in Chapters 5 and 6 to two canonic examples. In Chapter 5, the one-dimensional, thin, perfect conducting wire is considered in both the frequency- and time-domains; current, electric field, and pole distributions for a large number of unknowns are presented. In Chapter 6, the two-dimensional rectangular plate is analyzed in the time-domain; time-domain pole distributions are introduced for the square plate.

Chapter II

FUNDAMENTAL INTEGRAL EQUATIONS OF ELECTROMAGNETICS

2.1 INTRODUCTION

Singular integral equations (or singular integro-differential equations) represent a powerful and widely used approach to the solution of both antenna and electromagnetic scattering problems. A variety of methods may be used to obtain these equations. Poggio and Miller [9] rigorously develop the necessary results using the vector Green's theorem [10]. In this formalism, the concept of incident and scattered fields in conjunction with equivalent sources develops in a natural way. In this chapter, the frequency-domain equations are developed from linear system foundations. Although, perhaps, this approach is less rigorous than the method of Poggio and Miller, it yields fundamental results readily, without extensive vector manipulations. The time-domain representations of these equations are then obtained by inverse Fourier transform techniques. These general frequency- and time- domain results are finally specialized to describe thin, perfectly conducting surfaces.

2.2 MATHEMATICAL FORMALISM

The mathematical formulation of electromagnetic phenomena is fundamentally dependent on a concise set of equations known as Maxwell's equations. The complexity of these equations is highly dependent on the host medium. We will restrict our discussion throughout to a homogeneous, linear, and isotropic medium. For such a medium, Maxwell's equations may be written in differential form in the frequency-domain as (a vector will be denoted by a single bar; a frequency-domain quantity will be denoted by a tilde)

$$\begin{aligned}
 \nabla \times \tilde{\mathbf{E}}^t(\bar{\mathbf{r}}; \omega) &= -j\omega\mu_0 \tilde{\mathbf{H}}^t(\bar{\mathbf{r}}; \omega) - \tilde{\mathbf{M}}^t(\bar{\mathbf{r}}; \omega) \\
 \nabla \times \tilde{\mathbf{H}}^t(\bar{\mathbf{r}}; \omega) &= j\omega\epsilon_0 \tilde{\mathbf{E}}^t(\bar{\mathbf{r}}; \omega) + \tilde{\mathbf{J}}^t(\bar{\mathbf{r}}; \omega) \\
 \nabla \cdot \tilde{\mathbf{E}}^t(\bar{\mathbf{r}}; \omega) &= \tilde{\rho}^t(\bar{\mathbf{r}}; \omega)/\epsilon_0 \\
 \nabla \cdot \tilde{\mathbf{H}}^t(\bar{\mathbf{r}}; \omega) &= \tilde{\mathbf{m}}^t(\bar{\mathbf{r}}; \omega)/\mu_0
 \end{aligned}
 \tag{2-1}$$

Note that the time dependence, $\exp\{j\omega t\}$, has been suppressed. The total electric and magnetic field intensities are denoted by $\tilde{\mathbf{E}}^t(\bar{\mathbf{r}}; \omega)$ and $\tilde{\mathbf{H}}^t(\bar{\mathbf{r}}; \omega)$, the total electric and magnetic current densities are denoted by $\tilde{\mathbf{J}}^t(\bar{\mathbf{r}}; \omega)$ and $\tilde{\mathbf{M}}^t(\bar{\mathbf{r}}; \omega)$, and the parameters $\tilde{\rho}^t(\bar{\mathbf{r}}; \omega)$, $\tilde{\mathbf{m}}^t(\bar{\mathbf{r}}; \omega)$, ϵ_0 , μ_0 , ω , and $\bar{\mathbf{r}}$ denote, respectively, total electric and magnetic charge densities, electric permittivity, magnetic permeability, frequency, and observation position.

In the case of scattering by an obstacle, we may decompose the total fields and sources as

$$\vec{E}^t(\vec{r};\omega) = \vec{E}^{inc}(\vec{r};\omega) + \vec{E}^s(\vec{r};\omega) \quad (2-2a)$$

$$\vec{H}^t(\vec{r};\omega) = \vec{H}^{inc}(\vec{r};\omega) + \vec{H}^s(\vec{r};\omega) \quad (2-2b)$$

$$\vec{J}^t(\vec{r};\omega) = \vec{J}^s(\vec{r};\omega) + \vec{J}(\vec{r};\omega) \quad (2-2c)$$

$$\vec{M}^t(\vec{r};\omega) = \vec{M}^s(\vec{r};\omega) + \vec{M}(\vec{r};\omega) \quad (2-2d)$$

$$\vec{p}^t(\vec{r};\omega) = \vec{p}^s(\vec{r};\omega) + \vec{p}(\vec{r};\omega) \quad (2-2e)$$

$$\vec{m}^t(\vec{r};\omega) = \vec{m}^s(\vec{r};\omega) + \vec{m}(\vec{r};\omega) \quad (2-2f)$$

where \vec{E}^{inc} , \vec{H}^{inc} denote the incident fields which \vec{J}^s , \vec{M}^s , \vec{p}^s , and \vec{m}^s give rise to, and \vec{E}^s , \vec{H}^s are the scattered fields due to the sources \vec{J} , \vec{M} , \vec{p} , and \vec{m} induced on the scatterer (for dielectric scattering these sources are interpreted as effective sources that replace the obstacle). The scattered fields \vec{E}^s , \vec{H}^s obey, then, the vector Helmholtz equations

$$\nabla \times \nabla \times \vec{E}^s(\vec{r};\omega) - k^2 \vec{E}^s(\vec{r};\omega) = -j\omega\mu_0 \vec{J}(\vec{r};\omega) - \nabla \times \vec{M}(\vec{r};\omega) \quad (2-3a)$$

and

$$\nabla \times \nabla \times \vec{H}^s(\vec{r};\omega) - k^2 \vec{H}^s(\vec{r};\omega) = -j\omega\epsilon_0 \vec{M}(\vec{r};\omega) + \nabla \times \vec{J}(\vec{r};\omega) \quad (2-3b)$$

where k is the wavenumber, $\omega\sqrt{\epsilon_0\mu_0}$.

The fields which satisfy (2-3) may be found by convolving the impulse response of (2-3) with the forcing functions

present. The impulse response is obtained by determining the dyadic Green's function, $\bar{\bar{G}}(\bar{r}, \bar{r}'; \omega)$ (a double bar will denote a dyadic), which satisfies

$$\nabla \times \nabla \times \bar{\bar{G}}(\bar{r}, \bar{r}'; \omega) - k^2 \bar{\bar{G}}(\bar{r}, \bar{r}'; \omega) = \delta(\bar{r}, \bar{r}') \bar{\bar{I}} \quad (2-4)$$

Here, $\bar{\bar{I}}$ denotes a unit dyadic, \bar{r}' denotes the source position, and $\delta(\bar{r}, \bar{r}')$ denotes a three-dimensional Dirac delta distribution. The solution of equation (2-4) is given by [11]

$$\bar{\bar{G}}(\bar{r}, \bar{r}'; \omega) = (\bar{\bar{I}} + \frac{1}{k^2} \nabla \nabla) \tilde{\bar{G}}(\bar{r}, \bar{r}'; \omega) \quad (2-5)$$

where $\tilde{\bar{G}}(\bar{r}, \bar{r}'; \omega)$ is the free-space Green's function

$$\frac{e^{-jk|\bar{r} - \bar{r}'|}}{4\pi |\bar{r} - \bar{r}'|} \quad (2-6)$$

The scattered fields $\bar{E}^s(\bar{r}; \omega)$ and $\bar{H}^s(\bar{r}; \omega)$ may now be explicitly represented by

$$\bar{E}^s(\bar{r}; \omega) = \int_{V'} \bar{\bar{G}}(\bar{r}, \bar{r}'; \omega) \cdot [-j\omega\epsilon_0 \bar{J}(\bar{r}'; \omega) - \nabla \times \bar{M}(\bar{r}'; \omega)] d\bar{r}' \quad (2-7a)$$

and

$$\bar{H}^s(\bar{r}; \omega) = \int_{V'} \bar{\bar{G}}(\bar{r}, \bar{r}'; \omega) \cdot [-j\omega\epsilon_0 \bar{M}(\bar{r}'; \omega) + \nabla \times \bar{J}(\bar{r}'; \omega)] d\bar{r}' \quad (2-7b)$$

where V' denotes the volume occupied by the scatterer.

We substitute, next, equations (2-7a,b) into equations (2-2a,b). Using the vector identities $\nabla' \times \tilde{\mathbf{M}} = \nabla' \times (\tilde{\mathbf{G}} \tilde{\mathbf{M}}) - \nabla' \tilde{\mathbf{G}} \times \tilde{\mathbf{M}}$, $(\nabla' \tilde{\mathbf{G}}) \cdot \nabla' \times \tilde{\mathbf{M}} = -\nabla' \cdot (\nabla' \tilde{\mathbf{G}} \times \tilde{\mathbf{M}})$, and the relation $\nabla \tilde{\mathbf{G}}(\bar{\mathbf{r}}, \bar{\mathbf{r}}'; \omega) = -\nabla' \tilde{\mathbf{G}}(\bar{\mathbf{r}}, \bar{\mathbf{r}}'; \omega)$, we obtain the following space-frequency representations for the total electric and magnetic fields:

$$\begin{aligned} \tilde{\mathbf{E}}^t(\bar{\mathbf{r}}; \omega) = & \tilde{\mathbf{E}}^{inc}(\bar{\mathbf{r}}; \omega) + \frac{1}{j\omega\epsilon_0} \int_{V'} [k^2 \tilde{\mathbf{I}} + \nabla \nabla'] \cdot \tilde{\mathbf{J}}(\bar{\mathbf{r}}') \tilde{\mathbf{G}}(\bar{\mathbf{r}}, \bar{\mathbf{r}}'; \omega) d\bar{\mathbf{r}}' \\ & - \frac{1}{k^2} [k^2 \tilde{\mathbf{I}} + \nabla \nabla'] \cdot \left\{ \int_S \hat{\mathbf{n}}_{out} \times \tilde{\mathbf{M}}(\bar{\mathbf{r}}') \tilde{\mathbf{G}}(\bar{\mathbf{r}}, \bar{\mathbf{r}}'; \omega) ds' \right. \\ & \left. + \int_{V'} \tilde{\mathbf{M}}(\bar{\mathbf{r}}') \times \nabla' \tilde{\mathbf{G}}(\bar{\mathbf{r}}, \bar{\mathbf{r}}'; \omega) d\bar{\mathbf{r}}' \right\} \quad \bar{\mathbf{r}} \notin V' \end{aligned} \quad (2-8a)$$

and

$$\begin{aligned} \tilde{\mathbf{H}}^t(\bar{\mathbf{r}}; \omega) = & \tilde{\mathbf{H}}^{inc}(\bar{\mathbf{r}}; \omega) + \frac{1}{j\omega\mu_0} \int_{V'} [k^2 \tilde{\mathbf{I}} + \nabla \nabla'] \cdot \tilde{\mathbf{M}}(\bar{\mathbf{r}}') \tilde{\mathbf{G}}(\bar{\mathbf{r}}, \bar{\mathbf{r}}'; \omega) d\bar{\mathbf{r}}' \\ & + \frac{1}{k^2} [k^2 \tilde{\mathbf{I}} + \nabla \nabla'] \cdot \left\{ \int_S \hat{\mathbf{n}}_{out} \times \tilde{\mathbf{J}}(\bar{\mathbf{r}}') \tilde{\mathbf{G}}(\bar{\mathbf{r}}, \bar{\mathbf{r}}'; \omega) ds' \right. \\ & \left. + \int_{V'} \tilde{\mathbf{J}}(\bar{\mathbf{r}}') \times \nabla' \tilde{\mathbf{G}}(\bar{\mathbf{r}}, \bar{\mathbf{r}}'; \omega) d\bar{\mathbf{r}}' \right\} \quad \bar{\mathbf{r}} \notin V' \end{aligned} \quad (2-8b)$$

The integration over the surface, S , denotes integration over the surface bounding the volume V' .

The space-time representations of the electric and magnetic fields may be obtained by inverse Fourier transforming the frequency dependence found in expressions (2-8a) and (2-8b) [9]. They are given by

$$\begin{aligned} \epsilon_0 \frac{\partial}{\partial t} \bar{\mathbf{E}}^t(\bar{\mathbf{r}}; t) &= \epsilon_0 \frac{\partial}{\partial t} \bar{\mathbf{E}}^{inc}(\bar{\mathbf{r}}; t) + \frac{1}{4\pi} \int_{V'} \left[-\frac{\bar{\mathbf{I}}}{c^2} \frac{\partial^2}{\partial t^2} + \nabla \nabla \right] \cdot \frac{\bar{\mathbf{J}}(\bar{\mathbf{r}}'; \tau)}{R} d\bar{\mathbf{r}}' \\ &+ \frac{1}{4\pi\epsilon_0} \int_{R^1} \left\{ \left[-\frac{\bar{\mathbf{I}}}{c^2} \frac{\partial^2}{\partial t^2} + \nabla \nabla \right] \cdot \left[\int_S \hat{\mathbf{n}}_{out} \times \frac{\bar{\mathbf{M}}(\bar{\mathbf{r}}'; \tau)}{R} ds' \right. \right. \\ &\left. \left. + \int_{V'} \left(\bar{\mathbf{M}}(\bar{\mathbf{r}}'; \tau) \times \frac{(\bar{\mathbf{r}} - \bar{\mathbf{r}}')}{R^3} + \frac{\partial}{\partial \tau} \bar{\mathbf{M}}(\bar{\mathbf{r}}'; \tau) \times \frac{(\bar{\mathbf{r}} - \bar{\mathbf{r}}')}{cR^2} \right) d\bar{\mathbf{r}}' \right] \right\} dt \Big|_{\bar{\mathbf{r}} \neq V'} \end{aligned} \quad (2-9a)$$

$$\tau = t - R/c$$

and

$$\begin{aligned} \mu_0 \frac{\partial}{\partial t} \bar{\mathbf{H}}^t(\bar{\mathbf{r}}; t) &= \mu_0 \frac{\partial}{\partial t} \bar{\mathbf{H}}^{inc}(\bar{\mathbf{r}}; t) + \frac{1}{4\pi} \int_{V'} \left[-\frac{\bar{\mathbf{I}}}{c^2} \frac{\partial^2}{\partial t^2} + \nabla \nabla \right] \cdot \frac{\bar{\mathbf{M}}(\bar{\mathbf{r}}'; \tau)}{R} d\bar{\mathbf{r}}' \\ &- \frac{1}{4\pi\epsilon_0} \int_{R^1} \left\{ \left[-\frac{\bar{\mathbf{I}}}{c^2} \frac{\partial^2}{\partial t^2} + \nabla \nabla \right] \cdot \left[\int_S \hat{\mathbf{n}}_{out} \times \frac{\bar{\mathbf{J}}(\bar{\mathbf{r}}'; \tau)}{R} ds' \right. \right. \\ &\left. \left. + \int_{V'} \left(\bar{\mathbf{J}}(\bar{\mathbf{r}}'; \tau) \times \frac{(\bar{\mathbf{r}} - \bar{\mathbf{r}}')}{R^3} + \frac{\partial}{\partial \tau} \bar{\mathbf{J}}(\bar{\mathbf{r}}'; \tau) \times \frac{(\bar{\mathbf{r}} - \bar{\mathbf{r}}')}{cR^2} \right) d\bar{\mathbf{r}}' \right] \right\} dt \Big|_{\bar{\mathbf{r}} \neq V'} \end{aligned} \quad (2-9b)$$

$$\tau = t - R/c$$

where $R = |\bar{\mathbf{r}} - \bar{\mathbf{r}}'|$, c denotes the speed of light in vacuum, and the parameter τ denotes the time delay associated with a wave propagating over a scatterer. The notation $(\partial/\partial \tau) \bar{\mathbf{M}}(\bar{\mathbf{r}}'; \tau)$ should be interpreted as $(\partial/\partial \tau) \bar{\mathbf{M}}(\bar{\mathbf{r}}'; t)$ evaluated at $\tau = t$. Expressions (2-9a,b) are known as the space-time electric and magnetic field integral expressions (EFIE, MFIE); whereas expressions (2-8a,b) are the space-frequency representations of the EFIE and MFIE.

The representations presented are general expressions which are valid for an arbitrary scatterer positioned in the previously assumed medium for all \bar{r} such that $\bar{r} \neq \bar{r}'$. At the offending point $\bar{r} = \bar{r}'$, the expressions become singular and hence must be evaluated by considering the limit as \bar{r} approaches \bar{r}' [9,12]. The Cauchy or Hadamard principal value [13] is typically used for the description of these integrals. The frequency-domain representations of the electric and magnetic fields become in the Cauchy principal value sense (a single bar through the integral will denote a Cauchy integral)

$$\begin{aligned} \bar{E}^t(\bar{r};\omega) = & 2\bar{E}^{inc}(\bar{r};\omega) + \frac{2}{j\omega\epsilon_0} \text{FP} \int_{V'} [k^2 \bar{I} + \nabla\nabla] \cdot \bar{J}(\bar{r}') \bar{G}(\bar{r}, \bar{r}';\omega) d\bar{r}' \\ & - \frac{2}{k^2} [k^2 \bar{I} + \nabla\nabla] \cdot \left\{ \int_S \hat{n}_{out} \times \bar{M}(\bar{r}') \bar{G}(\bar{r}, \bar{r}';\omega) ds' \right. \\ & \left. - \int_{V'} \bar{M}(\bar{r}') \times \nabla \bar{G}(\bar{r}, \bar{r}';\omega) d\bar{r}' \right\} \quad \bar{r} \in V' \end{aligned} \quad (2-10a)$$

and

$$\begin{aligned} \bar{H}^t(\bar{r};\omega) = & 2\bar{H}^{inc}(\bar{r};\omega) + \frac{2}{j\omega\mu_0} \text{FP} \int_{V'} [k^2 \bar{I} + \nabla\nabla] \cdot \bar{M}(\bar{r}') \bar{G}(\bar{r}, \bar{r}';\omega) d\bar{r}' \\ & + \frac{2}{k^2} [k^2 \bar{I} + \nabla\nabla] \cdot \left\{ \int_S \hat{n}_{out} \times \bar{J}(\bar{r}') \bar{G}(\bar{r}, \bar{r}';\omega) ds' \right. \\ & \left. - \int_{V'} \bar{J}(\bar{r}') \times \nabla \bar{G}(\bar{r}, \bar{r}';\omega) d\bar{r}' \right\} \quad \bar{r} \in V' \end{aligned} \quad (2-10b)$$

Note that an interchange of primed to unprimed coordinates has been made. Similar factors of two appear in the time-domain representations, and FP denotes 'the finite part of'.

These results may be specialized to describe thin, perfect conducting surfaces [12]. On such a surface, the appropriate boundary conditions [10] are that the tangential total electric field is zero, i.e., $\hat{n} \times \tilde{\mathbf{E}}^t = 0$ (\hat{n} defined to be the outward normal unit vector on S), and that the tangential total magnetic field is equal to an equivalent surface current source, $\tilde{\mathbf{J}}_s$, i.e., $\hat{n} \times \tilde{\mathbf{H}}^t = \tilde{\mathbf{J}}_s$. With these boundary conditions, we may immediately write the space-frequency representations for the electric and magnetic fields on the surface S as

$$-\hat{n} \times \tilde{\mathbf{E}}^{\text{inc}}(\vec{r}; \omega) = \frac{\hat{n} \times \text{FP}}{j\omega\epsilon_0} \int_S [k^2 \tilde{\mathbf{I}} + \nabla \nabla] \cdot \tilde{\mathbf{J}}_s(\vec{r}'; \omega) \tilde{\mathbf{G}}(\vec{r}, \vec{r}'; \omega) d\vec{r}' \quad (2-11a)$$

and

$$\tilde{\mathbf{J}}_s(\vec{r}; \omega) = 2\hat{n} \times \tilde{\mathbf{H}}^{\text{inc}}(\vec{r}; \omega) - 2\hat{n} \times \int_S \tilde{\mathbf{J}}_s(\vec{r}'; \omega) \times \nabla \tilde{\mathbf{G}}(\vec{r}, \vec{r}'; \omega) ds' \quad (2-11b)$$

Similarly, the space-time representations are given by

$$-\epsilon_0 \hat{n} \times \frac{\partial}{\partial t} \mathbf{E}^{\text{inc}}(\vec{r}; t) = \frac{\hat{n}}{4\pi} \times \text{FP} \int_S \left[\frac{-\tilde{\mathbf{I}} \partial^2}{c^2 \partial t^2} - \nabla \nabla \right] \cdot \frac{\tilde{\mathbf{J}}_s(\vec{r}'; t)}{R} d\vec{r}' \quad (2-12a)$$

$$t = t - R/c$$

and

$$\begin{aligned} \vec{J}_s(\vec{r};t) = & 2 \hat{n} \times \vec{H}^{inc}(\vec{r};t) + \frac{\hat{n}}{2\pi} \times \int_S [\vec{J}_s(\vec{r}';\tau) \times \frac{(\vec{r}-\vec{r}')}{R^3} \\ & + \frac{\partial}{\partial \tau} \vec{J}_s(\vec{r}';\tau) \times \frac{(\vec{r}-\vec{r}')}{cR^2}] ds' \Big|_{\tau=t-R/c} \end{aligned} \quad (2-12b)$$

Note that the equivalent magnetic surface current, \vec{M}_s , does not appear in these expressions. \vec{M}_s is related to the total electric field by

$$\vec{M}_s = -\hat{n} \times \vec{E}^t \quad (2-13)$$

which vanishes for perfect conducting surfaces. Note, also, that for good conductors the effective current source \vec{J} may be replaced by $\sigma \vec{E}^t$ (σ denotes the conductivity of the obstacle), and therefore terms involving $\hat{n} \times \vec{J}$ also tend to zero.

As a final remark, we note that the term $2\hat{n} \times \vec{H}^{inc}$ appearing in expression (2-12b) is commonly known as the physical optics approximation for the current density \vec{J}_s . This approximation is useful for testing the validity of results obtained from expressions (2-12a,b) when no results for comparison exist.

Chapter III

FUNDAMENTAL CONCEPTS OF THE SINGULARITY EXPANSION METHOD

3.1 INTRODUCTION

The motivation for the singularity expansion method (SEM) is essentially based on experimental observations which have established that the transient surface currents generated on structures (scatterers) by arbitrary excitation are primarily in the form of damped sinusoids; the particular shape being dependent on the form of excitation and the specific geometry of the structure under consideration. By assuming that a scatterer can be uniquely specified mathematically by an associated modal and pole structure, and that the form of the excitation is known, the SEM enables one to determine the surface currents directly from an appropriate expansion of these parameters. Specifically, the expansion was found to require knowledge of four parameters [1]: the natural frequencies and corresponding natural modes, the structure of the incident wave, and scalar coefficients that couple the natural resonances to the incident wave (coupling coefficients). Since the form of the excitation is assumed to be known, the natural frequencies, natural modes, and coupling coefficients need to be determined in order to establish an SEM representation of the problem.

Mathematically, the expansion for the space-frequency surface currents induced by delta function excitation on finite, perfect conducting objects in free space is given by [1]

$$\tilde{U}(\bar{r};s) = \sum_{\alpha} \tilde{n}_{\alpha} \tilde{v}_{\alpha}(\bar{r})(s-s_{\alpha})^{-m_{\alpha}} + \tilde{W}(\bar{r};s) \quad (3-1a)$$

In the time-domain, this representation becomes

$$\bar{U}(\bar{r};t) = \sum_{\alpha} \bar{n}_{\alpha} \bar{v}_{\alpha}(\bar{r}) s_{\alpha}^t + \bar{W}(\bar{r};t) \quad (3-1b)$$

In these equations, s is a complex variable which is related to the frequency, ω , by $\text{Im}\{s\}=\omega$, $\tilde{U}(\bar{r};s)$, $\bar{U}(\bar{r};t)$ denote the space-frequency and space-time surface currents, \tilde{n}_{α} denotes the coupling coefficient associated with the pole s_{α} , $\tilde{v}_{\alpha}(\bar{r})$, $\bar{v}_{\alpha}(\bar{r})$ denote the natural mode vectors associated with s_{α} , $\tilde{W}(\bar{r};s)$ denotes an entire function and $\bar{W}(\bar{r};t)$ denotes the corresponding time-transformed function, m_{α} denotes the multiplicity of the pole s_{α} , and the summations are over all poles. In Section 3.2.1, we consider space-frequency techniques for obtaining the natural frequencies, and natural modes. In Section 3.2.2, we present space-frequency techniques for obtaining the coupling coefficients, and briefly discuss entire functions. In Section 3.3.1, we develop the Cordaro-Davis method for obtaining the natural responses.

Available techniques for analyzing the stability of various finite difference approximation schemes are also discussed in that section. And in Section 3.3.2, we present transient matrix methods for determining the coupling coefficients.

3.2 SPACE-FREQUENCY TECHNIQUES

3.2.1 Natural Frequencies and Modes

An arbitrary Fredholm integral equation of the first kind (e.g., expression (2-11a)) may be cast in the general form

$$\int_{R^3} \tilde{\tilde{\Gamma}}(\bar{r}, \bar{r}'; s) \cdot \tilde{\tilde{U}}(\bar{r}'; s) d\bar{r}' = \tilde{\tilde{I}}(\bar{r}; s) \quad (3-2)$$

where $\tilde{\tilde{\Gamma}}(\bar{r}, \bar{r}'; s)$ denotes a dyadic kernel, $\tilde{\tilde{U}}(\bar{r}'; s)$ denotes the desired unknown, and $\tilde{\tilde{I}}(\bar{r}; s)$ denotes an arbitrary forcing function.

For simplicity, we will write these integral equations using the inner product notation [1]

$$\langle \tilde{\tilde{\Gamma}}(\bar{r}, \bar{r}'; s); \tilde{\tilde{U}}(\bar{r}'; s) \rangle = \tilde{\tilde{I}}(\bar{r}; s) \quad (3-2a)$$

where the appropriate operation between the kernel and unknown will be given above the comma separating these parameters, and the integration is with respect to the common spatial variable.

A natural mode, $\tilde{v}_\alpha(\bar{r})$, satisfies equation (3-2a) in the absence of a forcing function. We may write

$$\langle \tilde{\Gamma}(\bar{r}, \bar{r}'; s_\alpha); \tilde{v}_\alpha(\bar{r}') \rangle = 0 \quad (3-3)$$

where s_α denotes the corresponding complex natural frequency.

The parameters s_α and $\tilde{v}_\alpha(\bar{r})$ may be found by discretizing equation (3-3) using a method of moments [14] formalism. We obtain

$$(\tilde{\Gamma}_{n,m}(s_\alpha)) \cdot (\tilde{v}_n)_\alpha = (\bar{0}_n) \quad (3-4)$$

where n, m are positive integers, $(\tilde{\Gamma}_{n,m}(s_\alpha))$ denotes an n by m matrix, $(\tilde{v}_n)_\alpha$ denotes the unknown mode vector of length n , and $(\bar{0}_n)$ is a zero vector of length n . The magnitude of both n and m is dependent on how refined the discretization is.

Equation (3-4) represents a homogeneous system of equations. Such a system has a solution if and only if the matrix $(\tilde{\Gamma}_{n,m}(s_\alpha))$ is singular. Hence, the natural frequencies, s_α , may be found by solving

$$\det [\tilde{\Gamma}_{n,m}(s_\alpha)] = 0. \quad (3-5)$$

The natural modes may now be found from equation (3-4) using the results of equation (3-5).

Equation (3-5) is, in general, extremely complicated to solve. Numerical solution techniques typically use either a function iteration root searching technique (Section 4.2.1) or a contour integration [15] (Section 4.2.2) method. The use of contour integration allows one to locate desired roots by partitioning the complex plane.

3.2.2 Coupling Coefficients and Entire Functions

The following derivation for obtaining the SEM coupling coefficients patterns a development due to Baum [5].

Associated with the coupling coefficient, \tilde{h}_α , is a coupling vector, $\tilde{u}_\alpha(\vec{r})$. The coupling vector is defined to be the conjugate adjoint of the natural mode, $\tilde{v}_\alpha(\vec{r})$, and hence satisfies

$$\langle \tilde{u}_\alpha(\vec{r}'); \tilde{v}(\vec{r}, \vec{r}'; s_\alpha) \rangle = 0. \quad (3-6)$$

By applying the method of moments, we have

$$(\tilde{u}_\alpha)_\alpha \cdot (\tilde{v}_{n,m}(s_\alpha)) = (\tilde{0}_n). \quad (3-7)$$

The kernel is now expanded in a Taylor series about $s=s_\alpha$ as

$$\tilde{\tilde{I}}(\bar{r}, \bar{r}'; s) = \sum_{l=0}^{\infty} (s-s_{\alpha})^l \tilde{\tilde{I}}_{l,\alpha}(\bar{r}, \bar{r}') \quad (3-8a)$$

$$\tilde{\tilde{I}}_{l,\alpha}(\bar{r}, \bar{r}') = \frac{1}{l!} \frac{\partial^l}{\partial s^l} \tilde{\tilde{I}}(\bar{r}, \bar{r}'; s) \Big|_{s=s_{\alpha}} \quad (3-8b)$$

The forcing function is similarly expanded as

$$\tilde{\tilde{I}}(\bar{r}; s) = \sum_{l=0}^{\infty} (s-s_{\alpha})^l \tilde{\tilde{I}}_{l,\alpha}(\bar{r}) \quad (3-9)$$

$$\tilde{\tilde{I}}_{l,\alpha}(\bar{r}) = \frac{1}{l!} \frac{\partial^l}{\partial s^l} \tilde{\tilde{I}}(\bar{r}; s) \Big|_{s=s_{\alpha}}$$

Assuming only a first order pole, we may write the response from equation (3-1a) as

$$\tilde{\tilde{U}}(\bar{r}; s) = \tilde{\tilde{u}}_{\alpha} \tilde{\tilde{v}}_{\alpha}(\bar{r}) (s-s_{\alpha})^{-1} + \tilde{\tilde{U}}'(\bar{r}; s) \quad (3-10)$$

where $\tilde{\tilde{U}}'(\bar{r}; s)$ denotes some analytic function about $s=s_{\alpha}$.

By substituting (3-9), (3-10) and (3-11) into the basic equation (3-2a) and matching powers of $(s-s_{\alpha})^l$, we obtain

$$\langle \tilde{\tilde{I}}_{0,\alpha}(\bar{r}, \bar{r}'); \tilde{\tilde{u}}_{\alpha} \tilde{\tilde{v}}_{\alpha}(\bar{r}) \rangle = 0 \quad (3-11a)$$

and

$$\langle \tilde{\tilde{I}}_{1,\alpha}(\bar{r}, \bar{r}'); \tilde{\tilde{u}}_{\alpha} \tilde{\tilde{v}}_{\alpha}(\bar{r}) \rangle + \langle \tilde{\tilde{I}}_{0,\alpha}(\bar{r}, \bar{r}'); \tilde{\tilde{U}}'(\bar{r}; s) \rangle = \tilde{\tilde{I}}_{0,\alpha}(\bar{r}) \quad (3-11b)$$

Operating on (3-12b) from the left by $\tilde{\tilde{u}}_{\alpha}(\bar{r})$ yields

$$\langle \tilde{\mathbf{L}}_\alpha(\vec{r}); \tilde{\mathbf{I}}_{1,\alpha}(\vec{r}, \vec{r}'); \tilde{\mathbf{h}}_\alpha \tilde{\mathbf{v}}_\alpha(\vec{r}) \rangle = \langle \tilde{\mathbf{L}}_\alpha(\vec{r}); \tilde{\mathbf{I}}_{0,\alpha}(\vec{r}) \rangle \quad (3-12)$$

since

$$\begin{aligned} \langle \tilde{\mathbf{L}}_\alpha(\vec{r}); \tilde{\mathbf{I}}_{0,\alpha}(\vec{r}, \vec{r}'); \tilde{\mathbf{U}}'(\vec{r}'; s) \rangle = \\ \int_{R^3} d\vec{r}' \left[\int_{R^3} d\vec{r} \tilde{\mathbf{L}}_\alpha(\vec{r}) \cdot \tilde{\mathbf{I}}_{0,\alpha}(\vec{r}, \vec{r}') \right] \cdot \tilde{\mathbf{U}}'(\vec{r}'; s) = 0 \end{aligned} \quad (3-13)$$

by equation (3-6). Therefore,

$$\tilde{\mathbf{h}}_\alpha = \frac{\langle \tilde{\mathbf{L}}_\alpha(\vec{r}); \tilde{\mathbf{I}}_{0,\alpha}(\vec{r}) \rangle}{\langle \tilde{\mathbf{L}}_\alpha(\vec{r}); \tilde{\mathbf{I}}_{1,\alpha}(\vec{r}, \vec{r}'); \tilde{\mathbf{v}}_\alpha(\vec{r}) \rangle} \quad (3-14)$$

is the expression for the coupling coefficient at $s=s_\alpha$.

The coupling coefficients relate the incident waveform to the modal structure of an object. They indicate which modes are excited and the extent to which they are excited. Baum [5] has discussed two different, but ultimately equivalent, types of these coupling coefficients in order to treat two different philosophical interpretations as to how modes are activated. In one interpretation, all modes are excited simultaneously across an object no matter where on the object the excitation originated. In the other interpreta-

tion, modes in various regions cannot be excited until the incident wave has reached those regions. We will not pursue these types further here.

The entire function, \tilde{W} , associated with the pole, s_α , is necessary for equation (3-1a) to be mathematically valid. Its form and use are not well understood, however. Typically, the entire function is omitted by the empiric justification of obtaining current distributions directly from a set of poles which are in good agreement with the distributions obtained by standard methods [5,16]. The physical significance of the inclusion or omission of the entire function requires further consideration.

3.3 SPACE-TIME TECHNIQUES

3.3.1 Natural Frequencies, Natural Modes, and Stability Considerations

In the time-domain, electromagnetic integral equations of the first kind may be written in general form as

$$\int_{R^3} \int_{R^1} \tilde{\Gamma}(\bar{r}, \bar{r}'; t-t') \cdot \bar{U}(\bar{r}'; t') dt' d\bar{r}' = \bar{I}(\bar{r}; t) \quad (3-15)$$

where $\tilde{\Gamma}(\bar{r}, \bar{r}'; t-t')$ denotes a retarded dyadic Green's function [11], $\bar{U}(\bar{r}'; t)$ denotes the desired unknown, and $\bar{I}(\bar{r}; t)$ denotes an arbitrary forcing function.

For illustrative purposes, we will restrict the discussion in this section to thin, perfect conducting surfaces for which integral expression (2-12a) is appropriate. The discussion will also be limited to rectangular (x, y, z) coordinate systems. A similar development applies to other expressions which may be cast in the form of equation (3-15), and other coordinate systems.

Since the spatial differential operators appearing in expression (2-12a) are with respect to the unprimed coordinates, the following variation of this expression is valid:

$$\epsilon_0 \vec{n} \times \frac{\partial}{\partial t} \vec{E}^{inc}(\vec{r}; t) = \vec{n} \times \left[\frac{1}{c^2} \frac{\partial^2}{\partial t^2} - \nabla^2 \right] \cdot \int_S \frac{\vec{J}_s(\vec{r}'; t - R/c)}{4\pi R} d\vec{r}' \quad (3-16)$$

Here, \vec{n} is the outward normal on some arbitrary surface S . The integral over this surface is commonly known as the magnetic vector potential. By letting $\vec{A}(\vec{r}; t)$ denote this potential, we may write (3-16) as

$$\epsilon_0 \vec{n} \times \frac{\partial}{\partial t} \vec{E}^{inc}(\vec{r}; t) = \vec{n} \times \left[\frac{1}{c^2} \frac{\partial^2}{\partial t^2} - \nabla^2 \right] \cdot \vec{A}(\vec{r}; t). \quad (3-16a)$$

The current density, $\vec{J}_s(\vec{r}; t - R/c)$, appearing in (3-16) is typically the unknown which is desired. However, for notational purposes, and stability analysis, expression (3-16a) is also of interest. This will become apparent as we progress.

In general, when a desired unknown appears buried within the integrand of an integral equation it is not possible to determine it analytically. To obtain a numerical solution, one generally begins by expanding this unknown in some suitable set of basis functions. If the function to be expanded is at least piecewise continuous over the region of interest, a suitable basis set would be a pulse expansion for the spatial variables. If the function is also reasonably well behaved through time, the temporal dependence may also be expanded as pulses. The function $\bar{J}_s(\bar{r}; t-R/c)$ generally satisfies these requirements, and hence a pulse expansion in both space and time is appropriate. It should be noted, however, that this approximation can become quite poor at surface edges due to the singular behavior of the current component parallel to the edge. Special care is required for such structures (Chapter 6).

The expansion of the current density may be written as

$$\bar{J}_s(\bar{r}; t-R/c) = \sum_{i=1}^N \sum_{p=-\infty}^{\infty} \bar{J}_{ip} P_{\Delta t}(t-p\Delta t-R/c) S_i(\bar{r}) \quad (3-17)$$

where

$$P_{\Delta t}(t-p\Delta t-R/c) = \begin{cases} 1, & \text{for } t \text{ in the time interval centered at } p\Delta t+R/c \\ 0, & \text{elsewhere} \end{cases}$$

$$S_i(\bar{r}) = \begin{cases} 1, & \text{for } \bar{r} \text{ in the space segment centered at } i\bar{r} \\ 0, & \text{elsewhere} \end{cases}$$

Here, $\bar{J}_{i,p}$ denotes the current amplitude coefficients; i denotes a general spatial index, i.e., i may represent one, two or three integer variables depending on the geometry of the problem; N denotes a general upper bound for the summations corresponding to each of integer variables which i represents; and $\Delta\bar{r}$ denotes a general spatial sampling distance, i.e., $\Delta\bar{r} = (\Delta x, \Delta y, \Delta z)$.

Expansion (3-17) enables one to write the vector potential appearing in expression (3-16a) explicitly as

$$\bar{A}(m\Delta, n\Delta, k\Delta; p\Delta t) = \sum_{m'=1}^{N_m} \sum_{n'=1}^{N_n} \sum_{k'=1}^{N_k} \sum_{p'=-\infty}^{\infty} \bar{J}_{m',n',k',p'} \cdot G_{m-m', n-n', k-k', (p-p')} \quad (3-18)$$

where

$$G_{\alpha, \beta, \delta, \eta} = \frac{\int_{(\alpha-1/2)\Delta}^{(\alpha+1/2)\Delta} \int_{(\beta-1/2)\Delta}^{(\beta+1/2)\Delta} \int_{(\delta-1/2)\Delta}^{(\delta+1/2)\Delta} \frac{p_{\Delta t} \{ \eta - (u^2 + v^2 + w^2)^{1/2} / c \}}{4\pi (u^2 + v^2 + w^2)^{1/2}} du dv dw,$$

m , n , and k being positive integers which are bounded by N_m , N_n , and N_k respectively, and p is an unbounded integer (by causality, p may be restricted to positive integers). Note that in this expansion we have tacitly assumed that the spatial sampling distance is uniformly equal to some constant, Δ , so that the continuous variables, (x, y, z) , correspond to

the discrete variables, $(m\Delta, n\Delta, k\Delta)$. This is typically, but not necessarily, done.

The current coefficients appearing in (3-18) are the desired parameters. They may be extracted by approximating the continuous differential operators appearing in (3-16a) by central finite difference operators. A thorough discussion of finite difference approximation (FDA) techniques may be found in Ames [17].

In passing, it is worthwhile to note that it is possible to establish an analytic equivalence between the finite difference formulation of a time-domain problem and the basis set formulation of the equivalent frequency-domain problem by using inverse transform techniques. This equivalence is satisfying since it establishes that finite difference techniques are not simply convenient mathematical tools for the solution of time-domain problems, but are appropriate, physically meaningful, methods of solution.

By using finite differences, the time derivative of the vector potential may be written as

$$\frac{1}{c^2} \frac{\partial^2}{\partial t^2} \bar{A}(\bar{r}; t) = \frac{1}{(c\Delta t)^2} [\bar{A}(\bar{r}; (p+1)\Delta t) + \bar{A}(\bar{r}; (p-1)\Delta t) - 2\bar{A}(\bar{r}; p\Delta t)] + O((\Delta t)^2) \quad (3-19)$$

where $O((\Delta t)^2)$ denotes the order of the truncation error introduced in the FDA. The spatial operators may be similarly differenced (Section 5.3, and Sections 6.3, 6.4).

Expression (3-16a) may now be written as ($p=1,2,\dots$)

$$\begin{aligned} \hat{n} \times \bar{A}(\bar{r};(p+1)\Delta t) = & (c\Delta t)^2 [\hat{n} \times \nabla(\nabla \cdot \bar{A}(\bar{r};p\Delta t))] \\ & - \hat{n} \times \bar{A}(\bar{r};(p-1)\Delta t) + 2\hat{n} \times \bar{A}(\bar{r};p\Delta t) + \\ & \epsilon_0 (c\Delta t)^2 \hat{n} \times \frac{\partial}{\partial t} \bar{E}^{inc}(\bar{r};p\Delta t) + O(\Delta t)^2 \end{aligned} \quad (3-20)$$

This formulation establishes an explicit or time-marching finite time-differenced scheme for the vector potential. An explicit scheme allows one to find future values in terms of previous results without the need for a matrix inversion. Note that the values of the vector potential at two previous times are required.

By substituting expression (3-18) into the difference equation for the vector potential and manipulating the summations, we may obtain an explicit expression for the current density coefficients, $\bar{J}_{i,p}$ (general spatial index i). An explicit expression for these coefficients for the linear thin-wire problem may be found in Section 5.3. In this section, we consider a general expression for these coefficients which is suitable for an arbitrary geometry. The formulation will naturally lead into a discussion of stability methods for finite difference schemes.

By translating the continuous temporal and spatial operators appearing in expression (3-16a) to central finite dif-

ference operators, and by using expansion (3-13) to represent the vector potential, the following general representation for the current density coefficients is obtained (note that the notation, \bar{T}_{p+1} , used to represent all discrete functions is interpreted as $\bar{T}(m\Delta, n\Delta, k\Delta, (p+1)\Delta t)$):

$$0 = \sum_{p'=-1}^{N_T} B_{p'} \bar{J}'_{p-p'} + \bar{F}_{p+1}$$

or

$$\bar{J}'_{p+1} = B_{-1}^{-1} \left[\sum_{p'=0}^{N_T} B_{p'} \bar{J}'_{p-p'} + \bar{F}_{p+1} \right] \quad (3-21)$$

where B_p denotes coefficient matrices corresponding to different times (B_{-1} is a diagonal matrix corresponding to \bar{J}'_{p+1}); \bar{F}_{p+1} denotes the forcing function at the $(p+1)$ -th time step; and N_T denotes an integer which is one fewer than the number of time steps required for a wave to propagate across the maximum distance of the structure; in other words, if, for example, six time steps are required for a wave to travel this maximum distance, N_T would be five since the summation begins at zero. The prime, \bar{J}'_{p+1} , indicates a vector of the current density coefficients of every spatial point of interest on the structure. And as a final remark, we note that the rank of the B matrices is dependent on the particular geometry of the problem being studied. For con-

venience, we define the rank of these matrices to be some integer, N .

To obtain the natural frequencies and natural modes, we are interested in equation (3-21) in the absence of a forcing function, i.e.,

$$\bar{J}'_{p+1} = \sum_{p'=0}^{N_T} C_p \bar{J}'_{p-p'} \quad (3-22)$$

where $C_p = (B_{-1})^{-1} B_p$. The solution of this difference equation may be obtained by z transform techniques. For simple poles, the solution is given by

$$\bar{J}'_{p+1} = z_x^{p+1} \bar{v}_x \quad (3-23)$$

where $z_x = \exp\{s_x \Delta t\}$ denotes the transient representation of the pole, s_x , and \bar{v}_x denotes a vector spatially describing the natural mode. For poles of multiplicity $m_x, m_x \neq 1$, the solution is given by

$$(\bar{J}'_{p+1})^{m_x} = (p+1)^{m_x} z_x^{p+1} \bar{v}_{x,m_x} \quad (3-24)$$

where \bar{v}_{x,m_x} denotes the natural mode vector corresponding to a pole of multiplicity m_x . Note that entire functions do not appear in this development; a pole structure only is the basis for this method. Pole clusters may attempt to model an entire function however, and therefore entire functions

may still be significant although they are not explicitly represented in the formalism.

By substituting equation (3-23) (assuming first order poles) into (3-22), we obtain

$$\left[I - \sum_{p'=0}^{N_T} C_{p'} z_{\alpha}^{-(p'+1)} \right] \bar{v}_{\alpha} = 0 . \quad (3-25)$$

This is a homogeneous system of equations. The poles may be found from

$$\det \left[I - \sum_{p'=0}^{N_T} C_{p'} z_{\alpha}^{-(p'+1)} \right] = 0 . \quad (3-26)$$

The modes may now be found from (3-25).

There is an alternative to this z transform solution technique. Any finite difference scheme in the form of equation (3-22) may be condensed into an equivalent two-level matrix form [17] by introducing a state vector, \bar{K}_p for the p -th time step, such that (T denotes transpose)

$$\bar{K}_p^T = \left[\bar{J}_p^T, \bar{J}_{p-1}^T, \dots, \bar{J}_{p-N_T}^T \right], \quad (3-27)$$

a state transition matrix, Φ , such that

$$\Phi = \begin{bmatrix} C_0 & C_1 & \dots & C_{N_T} \\ I & 0 & \dots & 0 \\ 0 & I & \dots & \vdots \\ \vdots & \vdots & \ddots & \vdots \\ 0 & \dots & 0 & I & 0 \end{bmatrix}, \quad (3-28)$$

and forming

$$\bar{K}_{p+1} = \Phi \bar{K}_p. \quad (3-29)$$

A discussion of error propagation, or a stability analysis of finite difference schemes is appropriate at this time. A discrete finite difference representation of a continuous problem may yield an unstable (unbounded) solution when certain relationships between the sampling distances used for different variables are not satisfied. For hyperbolic equations (wave equations, e.g., equation (3-16)) the relation between the time sampling (Δt) and spatial sampling (Δ , assuming a uniform sampling distance in all directions) distances are of interest. It has been shown by Courant, Friedrichs and Lewy (CFL) [17] that the time sampling distance for these equations can be at most equal to the spatial distance, i.e., $\Delta t = \Delta$. This is the most lax restriction possible; it can tighten considerably depending on how the

discretization is implemented. Two methods are available to analyze the stability of finite difference schemes for linear equations. We consider these now.

The state transition matrix appearing in equation (3-29) contains all the information of the finite difference approximation (including boundary conditions). A stability analysis of the difference scheme may be done by examining the magnitude of the eigenvalues of this matrix. If all the eigenvalues are less or equal to one in magnitude, errors will not grow through time and hence the solution will be bounded. This technique is known as matrix stability analysis. The matrix stability method is useful for testing if a known CFL condition yields a stable solution. It does not predict, in general, the specific numerical value required for stability. An alternate method may be used to determine, or at least approximate, this value.

A simple method known as Fourier stability analysis may be used to determine the stability criterion for an uncompressed difference scheme (e.g., equation (3-20) or (3-22) instead of equation (3-29)). The method analyzes only the specific difference equation and hence ignores the influence of boundary conditions. Since boundary conditions can influence the stability of a scheme, the Fourier method is not considered as thorough as the matrix method. However, since

a specific number, whether exact or approximate, for the CFL condition is readily produced, this method provides useful a priori information about a particular difference formulation. The matrix method may always be used to confirm the stability criterion given.

In brief, the Fourier method examines the propagating effect of a single row of errors along some arbitrary line of the FDA. This is accomplished by determining an exponential solution for the difference scheme from discrete separation of variable techniques. For a stable solution, restrictions on the exponential solution must be enforced. A one-dimensional example may be found in Section 5.3. Two-dimensional examples may be found in Sections 6.3, 6.4.

Stability alone does not imply convergence of the FDA to the true solution. For a thorough discussion on matrix and Fourier stability methods and convergence requirements one should refer to Ames [17].

The stability of physical problems is mathematically described by the location of poles in the complex plane. The stability of the finite difference representation of electromagnetic expressions is dependent on the magnitude of the eigenvalues of the state transition matrix. Hence, we anticipate some relation to exist between these eigenvalues and the true poles.

The relation follows simply by considering the solution of the difference equation, equation (3-24), applied to the state transition formulation. For first order poles, we may write

$$z_{\alpha}^{p+1} \bar{K}_{\alpha} = \phi z_{\alpha}^p \bar{K}_{\alpha} \quad (3-30)$$

or

$$z_{\alpha} \bar{K}_{\alpha} = \phi \bar{K}_{\alpha} . \quad (3-31)$$

This represents an algebraic eigenvalue problem for the eigenvalue, z_{α} , and the eigenvector, \bar{K}_{α} . It can be shown that the natural mode, \bar{v}_{α} , and \bar{K}_{α} are related to one another by

$$\bar{K}^T = \left[z_{\alpha}^{N_T} \bar{v}_{\alpha}^T, z_{\alpha}^{N_T-1} \bar{v}_{\alpha}^T, \dots, \bar{v}_{\alpha}^T \right] \quad (3-32)$$

The poles, s_{α} , may be found by solving

$$s_{\alpha} = \ln(z_{\alpha})/\Delta t . \quad (3-33)$$

3.3.2 Coupling Coefficients

A method has been presented which determines the natural frequencies and natural modes. To complete the SEM form of solution we need to determine the coefficients that couple

the natural frequencies and modes to the incident forcing function. Two different formulations of these coupling coefficients are possible in the time-domain. Cordaro [18] has suggested a method to obtain an exact representation of the coefficients when a complete set of distinct eigenvalues (first order poles) is known. This is accomplished by using eigenvector decomposition techniques. The basic method may be extended to obtain an approximation to the coefficients when only a partial set of distinct eigenparameters is known. An alternate formulation for a partial set of poles is a time-domain analog of the frequency-domain technique previously presented (Section 3.2.2). We will initially consider Cordaro's method.

Define a state vector, \bar{U}_p , to represent a normal incident forcing function at the p-th time step as

$$\bar{U}_p^T = [\bar{F}_p, 0, \dots, 0]^T. \quad (3-34)$$

Here, \bar{F}_p and 0 are $1 \times N$ row vectors.

Note that for a delta or impulse excitation only \bar{U}_0 is nonzero. The state current distribution may now be written explicitly as (a state representation of the forcing function has been added to equation (3-29))

$$\begin{aligned}
\bar{K}_1 &= \bar{U}_0 \\
\bar{K}_2 &= \phi \bar{U}_0 + \bar{U}_1 \\
&\vdots \\
\bar{K}_m &= \sum_{i=0}^{m-1} \phi^{m-i-1} \bar{U}_i
\end{aligned} \tag{3-35}$$

where m is some arbitrary time step. By assuming a full set of distinct eigenvalues, Λ , and corresponding eigenvectors, Γ , we may decompose ϕ as

$$\phi = \Gamma \Lambda \Gamma^{-1} . \tag{3-36}$$

Equation (3-35) may now be written as

$$\bar{K}_m = \Gamma \sum_{i=0}^{m-1} \Lambda^{m-i-1} \Gamma^{-1} \bar{U}_i . \tag{3-37}$$

Since only the first N components of the eigenvectors correspond to the natural modes, we introduce a vector, \bar{T}_p , to spatially describe only the first N components of the state current vector \bar{K}_p (the first N components define \bar{U}'_p). We may write (assuming an impulse excitation)

$$\bar{T}_p = [I, 0, \dots, 0] \Gamma \Lambda^{p-1} \Gamma^{-1} \bar{U}_0 . \tag{3-38}$$

Here, I and O denote $N \times N$ identity and zero matrices.

Next, we let M be defined to be the unnormalized natural mode matrix and \bar{C} be defined to be the unnormalized vector of coupling coefficients. They are given respectively by

$$M = \Gamma^{-T} [I, 0, \dots, 0]^T , \tag{3-39}$$

$$\bar{c} = r^{-1} \bar{u}_0. \quad (3-40)$$

Combining these results yields

$$\bar{T}_p = M^T \Lambda^{p-1} \bar{c} \quad (3-41)$$

or equivalently

$$\bar{T}_p = \sum_{\alpha} z_{\alpha}^{p-1} \eta_{\alpha} \bar{v}_{\alpha} \quad (3-42)$$

where the pole s_{α} is related to z_{α} by equation (3-33), η_{α} denotes the coupling coefficients, and \bar{v}_{α} denotes the corresponding natural modes. Equation (3-42) is the desired SEM representation.

When only a partial set of eigenvalues is known, the decomposition of \ddagger as given by equation (3-36) is not possible exactly since the inverse which appears only exists in a generalized or pseudo inverse sense. Therefore, only a least squares approximation to the coupling coefficients is possible in this case.

This complication may be avoided by developing a time-domain formulation for the coupling coefficients analogous to the frequency-domain method (Section 3.2.2). We begin by replacing $\ddagger(r, r'; s)$ by a matrix function $T(z)$ defined by

$$T(z) = \begin{bmatrix} z^{N_T+1} & z^{N_T} & \dots & z^{(N_T-1)} \\ I & C_1 & \dots & C_{N_T-1} \end{bmatrix}. \quad (3-43)$$

By following similar power series expansions, we then define $T_{1,\alpha}(z_\alpha)$ in analogy with $\bar{T}_{1,\alpha}(\bar{r}, \bar{r}')$ to be

$$T_{1,\alpha}(z_\alpha) = \begin{bmatrix} N_T & (N_T-1) & (N_T-i-1) \\ (N_T+1)z_\alpha I - \sum_{i=0}^{N_T-1} (N_T-1)C_i z_\alpha \end{bmatrix} \quad (3-44)$$

We define, next, the coupling vector, $\bar{u}_\alpha(\bar{r})$, to be the first block of N elements of the left eigenvector¹ corresponding to the α -th eigenvalue of the state transition matrix.

By replacing the frequency-domain inner product operations by matrix multiplications, we may write the coupling coefficient at $z=z_\alpha=\exp\{s_\alpha \Delta t\}$ as

$$u_\alpha(z_\alpha) = \frac{\bar{u}_\alpha^T \bar{I}(z_\alpha)}{\bar{u}_\alpha^T (T_{1,\alpha}(z_\alpha) \bar{u}_\alpha)} \quad (3-45)$$

where $\bar{I}(z_\alpha)$ is the forcing function vector evaluated at z_α .

It should be noted that when each of the sub-matrices of the state transition matrix are symmetric, the first N rows of the left and right eigenvectors are identical to a normalization factor. This is not true for the remaining portion of these vectors, however, since it can be shown that

¹ Let p be the right eigenvector of the transpose of some matrix A corresponding to the eigenvalue λ . Then p satisfies $A^T p = \lambda p$. Now consider $(A^T p)^T = p^T A = \lambda^* p^T$. In this case, p is known as the left eigenvector of the matrix A . Hence, p is either the right eigenvector associated with the matrix A^T or the left eigenvector associated with the matrix A corresponding to the eigenvalue λ .

the left eigenvectors have a much more complicated structure than the right eigenvectors.

The matrix decomposition formulation is recommended when a full set of distinct eigenparameters is known; the left-right eigenvector formulation is recommended when a partial set is known.

In conclusion, we note that although the TD-SEM formulation for obtaining the natural frequencies and natural modes is relatively straightforward, a fundamental complication does underlie the method. Since the size of the transition matrix is highly dependent on the geometry and the level of discretization of a particular problem, it is possible, even for simple geometries, to generate a transition matrix which surpasses the high speed storage capabilities of the largest computers. A variety of techniques which attempt to handle this complication by taking advantage of the form of this matrix are presented in Chapter 4.

Chapter IV

EIGENSOLUTION METHODS FOR THE TRANSITION MATRIX

4.1 INTRODUCTION

The TD-SEM model is a straightforward and efficient method for determining the SEM parameters for simple geometries discretized with relatively few unknowns. This is accomplished by transforming the pole searching problem into an algebraic eigenvalue problem (Section 3.3.1). As the number of unknowns increase, however, the matrix which TD-SEM generates becomes unmanagably large, thereby making the search for eigenvalues difficult and complicated.

The matrix Φ , whose eigensolution is sought, is given by equation (3-28). Some comments are in order about the form and properties of this matrix.

Φ is known as a sparse matrix since it contains a large number of zero elements. It is in block upper Hessenburg, or more specifically, block Frobenius form [19]. A matrix in Frobenius form possesses no symmetry properties, and therefore, Φ unfortunately falls into the class of unsymmetric real matrices, or general real matrices. This is indeed a complication since the field of eigensolution methods is both narrowed and complicated for unsymmetric matrices due to the possibility of obtaining complex eigenvalues and generalized eigenvectors.

A matrix in Frobenius form possesses the property that it is its own companion matrix. In other words, the problem of determining the eigenvalues, λ , of Φ may be done in either of two possible forms. First, we may consider the full matrix and solve

$$\det [\Phi - \lambda I] = 0 \quad (4-1)$$

where I is the identity matrix; alternatively, we may solve

$$\det [\lambda^{N_T+1} I - \lambda^{N_T} C_0 - \dots - C_{N_T}] = 0. \quad (4-2)$$

where C_0, C_1, \dots, C_{N_T} denote the sub-matrices of the top row of the transition matrix. The former scheme generally leads to eigensolution methods, whereas the latter generally leads to root searching methods. An exception is an application of Laguerre's root searching method to a matrix in Hessenburg form [20].

Laguerre's method and various other root searching methods are discussed in Section 4.2. Eigensolution methods for unsymmetric matrices are presented in Section 4.3. A survey of eigensolution methods for symmetric matrices may be found in [21].

4.2 ROOT SEARCHING METHODS

We are required to find λ_i , $i=1,2,\dots,N_T(N_T+1)$, such that

$$\det [B_i] = 0 \quad (4-3)$$

where

$$B_i = [\lambda_i^{N_T+1} I - \lambda_i^{N_T} C_0 - \dots - C_{N_T}] \quad (4-4)$$

is an $N \times N$ polynomial matrix.

We consider three techniques for obtaining the roots of equation (4-3). In the first approach, (4-3) is solved directly. This requires root searching methods which utilize function iteration since the explicit coefficients of the characteristic equation are not known. Muller's method [22] represents a logical method for solution and is discussed in Section 4.2.1. An alternate method for obtaining these roots is to use the complex contour integration method of Singaraju, Giri, and Baum [15]. This technique is presented in Section 4.2.2. The third approach is to exploit polynomial matrix reduction methods [23] whereby the polynomial matrix (4-4) is iteratively reduced into a triangular polynomial matrix. The explicit characteristic equation is then the product of the diagonal polynomials. A wide selection

of efficient polynomial zero searching methods may then be used to find the roots. A polynomial matrix reduction method is discussed in Section 4.2.3.

An application of Laguerre's method is presented in Section 4.2.4. Since this technique does not utilize either form (4-3) or (4-4) we consider it to be independent of the methods previously mentioned. However, since the method is a zero searching method it logically belongs within Section 4.2.

4.2.1 Muller's Method

The following is a brief summary of the work due to Muller [22].

We are interested in determining the values of λ which satisfy $f(\lambda)=0$, for some function f . One begins the process with the values λ_i , h_i , k_i , $f(\lambda_i)$, $f(\lambda_{i-1})$, and $f(\lambda_{i-2})$, where λ_i , h_i , and k_i are some judicious initial guesses, and i is an iterative index; k_{i+1} is then determined by the formula

$$k_{i+1} = \frac{-2f(\lambda_i)\delta_i}{g_i + (g_i^2 - 4f(\lambda_i)\delta_i k_i [f(\lambda_{i-2})k_i - f(\lambda_{i-1})\delta_i + f(\lambda_i)]^{1/2}} \quad (4-5)$$

where

$$\delta_i = 1 + k_i, \quad (4-5a)$$

and

$$g_i = f(\lambda_{i-2})k_i^2 - f(\lambda_{i-1})\delta_i^2 + f(\lambda_i)(k_i + \delta_i) \quad (4-5b)$$

Then

$$\lambda_{i+1} = \lambda_i + h_{i+1}, \quad (4-5c)$$

$$h_{i+1} = k_{i+1} h_i, \quad (4-5d)$$

and

$$f(\lambda_{i+1}) \quad (4-5e)$$

are computed. The sign of the square root in the formula for k_{i+1} is chosen to make the denominator have the greater modulus. The formulas are derived by fitting a quadratic of the form, $b_0\lambda^2 + b_1\lambda + b_2$, through the following three points : $(\lambda_i, f(\lambda_i))$, $(\lambda_{i-1}, f(\lambda_{i-1}))$, $(\lambda_{i-2}, f(\lambda_{i-2}))$. The coefficients b_0 , b_1 , b_2 satisfy

$$b_0 \lambda_i^2 + b_1 \lambda_i + b_2 = f(\lambda_i)$$

$$b_0 \lambda_{i-1}^2 + b_1 \lambda_{i-1} + b_2 = f(\lambda_{i-1})$$

$$b_0 \lambda_{i-2}^2 + b_1 \lambda_{i-2} + b_2 = f(\lambda_{i-2}) \quad (4-5f)$$

The process iteratively continues until some specified criterion for acceptance of the root estimate is satisfied or an upper limit on the number of allowed iterations has been reached.

It is interesting to note that the convergence properties of Muller's method have never been proven for polynomials with orders greater than two. Nevertheless it is commonly used on relatively large polynomials with excellent results.

For our purpose, equation (4-3) denotes the function f discussed above. In general, only one determinant evaluation is required for each estimate at λ_1 . Excellent results (eight to ten digit agreement with known solutions) were obtained using this technique for systems which possessed approximately 110 roots. For higher order systems, however, fewer and fewer of the predicted roots had any relation to the actual roots. In particular, for a system which was known to have 225 roots, only 4 of the predicted roots had any relation to the actual roots. This breakdown is attributed to decreased separation in the roots of large systems (since by stability, all the eigenvalues must fall within the unit circle in the complex plane), coupled with the numerical roundoff errors associated with evaluating equation (4-3).

4.2.2 Contour Integration

The following brief summary is based on the work of Singaraju, Giri, and Baum [15].

If a function $f(\lambda)$ is meromorphic² in a simply-connected domain D containing a Jordan contour C , and $g(\lambda)$ is some analytic function within D , we may write using the residue theorem

$$\frac{1}{2\pi i} \int_C \frac{f'(\lambda)}{f(\lambda)} g(\lambda) d\lambda = \sum_{i=1}^{N_0} g(\lambda_{0_i}) \quad (4-6)$$

where λ_{0_i} is the i -th zero of $f(\lambda)$ in C , N_0 is the total number of zero's within C , and the prime denotes differentiation.

Since $g(\lambda)$ is an arbitrary analytic function, we let $g(\lambda) \equiv \lambda^k$, $k=0,1,\dots,N_0$. The zero's of $f(\lambda)$ in C may then be obtained from the non-linear system

$$\begin{bmatrix} \lambda_{0_1} + \lambda_{0_2} + \dots + \lambda_{0_{N_0}} \\ \lambda_{0_1}^2 + \lambda_{0_2}^2 + \dots + \lambda_{0_{N_0}}^2 \\ \vdots \\ \lambda_{0_1}^{N_0} + \lambda_{0_2}^{N_0} + \dots + \lambda_{0_{N_0}}^{N_0} \end{bmatrix} = \begin{bmatrix} I_1 \\ I_2 \\ \vdots \\ I_{N_0} \end{bmatrix} \quad (4-7)$$

² A meromorphic function is a function which may be represented as the quotient of two entire functions and which possesses poles only in the finite complex plane.

where

$$I_k = \frac{1}{2\pi i} \int_C \lambda^k \frac{f'(\lambda)}{f(\lambda)} d\lambda \quad k = 0, 1, 2, \dots, N_0 \quad (4-8)$$

This rather unique technique has been shown to be quite effective for obtaining the natural frequencies from the space-frequency formulation of the linear, thin-wire problem. In this formulation, the function $f(\lambda)$ mentioned above corresponds to $\det[Z(s_\alpha)]$, where s_α denotes the natural frequencies, and $Z(\cdot)$ denotes the moment method impedance matrix. If, for example, twenty unknowns are used for the discretization, then the evaluation of this determinate is basically equivalent to the evaluation of a twentieth degree polynomial. Numerically, this evaluation should not present many complications; whence, the evaluation of the contour integral (4-8) and the subsequent solution of the non-linear system (4-7) should be numerically quite stable.

The situation is a bit more complicated for the TD-SEM formulation of this problem. The determinate of equation (4-4) now denotes the function $f(\lambda)$ above. For a similar twenty unknown discretization, $f(\lambda)$ now corresponds to the evaluation of approximately a four hundredth degree polynomial. This represents a serious accuracy problem numerically. It was feared complications similar to those observed

with Muller's method would develop with this method when the determinate of equation (4-4) was evaluated prior to the integration, and therefore the method was not further pursued in this context. By interchanging the determinate and integral operations, however, it may be possible to avoid the numerical errors associated with the determinate evaluation. The interchange may effectively result in a 'numerical smoothing' which will give meaning to the evaluation of the determinate even for large scale problems. Confirmation of this conjecture is delayed to a future study.

4.2.3 Polynomial Matrix Reduction

A matrix of polynomials may be triangularized by using similar elimination methods to those associated with the reduction of standard matrices [23]. A simple example is the most efficient way to describe the method.

Example 4.1

We consider the matrix

$$\lambda^2 I - \lambda C_0 - C_1 = \begin{bmatrix} \lambda^2 - \lambda C_{011} - C_{111} & -\lambda C_{012} - C_{112} \\ -\lambda C_{021} - C_{121} & \lambda^2 - \lambda C_{022} - C_{122} \end{bmatrix} \quad (4-9)$$

where

$$C_0 = \begin{bmatrix} C_{011} & C_{012} \\ C_{021} & C_{022} \end{bmatrix} ; \quad C_1 = \begin{bmatrix} C_{111} & C_{112} \\ C_{121} & C_{122} \end{bmatrix}. \quad (4-9a)$$

By performing elementary operations, this matrix may be reduced to triangular form to yield the explicit characteristic equation

$$\begin{aligned} \lambda^4 - \lambda^3 (C_{022} + C_{011}) - \lambda^2 (C_{122} + C_{111} + C_{012} C_{021} - C_{011} C_{022}) \\ + \lambda (C_{011} C_{122} + C_{022} C_{111} - C_{012} C_{121} - C_{112} C_{021}) + (C_{122} C_{111} - C_{112} C_{121}) \end{aligned} \quad (4-10)$$

Any of a wide variety of polynomial zero searching methods may now be used to determine the roots.

This example establishes the basic technique. In theory it may be applied to a matrix of arbitrary size. Unfortunately, in practice the method numerically breaks down due to piling of the coefficients of the eliminated polynomials on the diagonal polynomials. This results in a wide dynamic range in the diagonal coefficients which causes simultaneous overflow and underflow. This was observed for systems with only 56 roots. A sophisticated machine based scaling system [24] could have partially controlled this dynamic range difficulty; however, it was feared it would simply

postpone the breakdown to a slightly larger system and was therefore not pursued.

4.2.4 Laguerre's Method

An application of Laguerre's method suitable to the eigenvalue problem has been developed by Parlett [20]. The following brief summary is based on his work.

Let λ be an approximation to a root of the polynomial $p(\lambda)$, where $p(\lambda)$ is of degree n . Laguerre's method requires $p(\lambda)$, $p'(\lambda)$, and $p''(\lambda)$ (prime denotes a derivative with respect to the argument) to obtain a better approximation. By defining

$$s_1(\lambda) = \frac{p'(\lambda)}{p(\lambda)} \quad \text{and} \quad s_2(\lambda) = \frac{(p'(\lambda))^2 - p(\lambda)p''(\lambda)}{(p(\lambda))^2} \quad (4-11)$$

Parlett derives

$$\lambda_{i+1} = \lambda_i - \frac{n}{s_{1+} + ((n-1)(ns_2 - s_1^2))^{1/2}} \quad (4-12)$$

where the square root which maximizes the absolute value of the denominator is chosen and n denotes the degree of the polynomial $p(\lambda)$ (for the details of this expression one should refer to Parlett [20]).

Several convergence properties have been proven for Laguerre's method. A listing may be found in Kelly [25].

Although the formulas given seem applicable only for polynomials, they may be used on a matrix in Hessenburg form by using Hyman's method [20] to recursively yield the required derivatives directly from this matrix. Unfortunately, Φ is in block upper Hessenburg form and not standard upper Hessenburg form. To use Hyman's method a transformation to standard upper Hessenburg form (Section 4.3.1) would be required. Such a transformation generally destroys the sparse properties of a matrix, thereby making use of Laguerre's method in this context unfeasible for determining the required eigenvalues.

In summary, the direct root searching methods tested which exploit the form of equation (4-3) (i.e., Muller's method, and the polynomial matrix method) were found to be useful only for relatively small systems due to root crowding and errors associated with the numerical process (in particular, the determinant evaluation). The contour integration technique may prove useful for large systems if the integration can numerically smooth the required determinate; the feasibility of this requires further consideration. Parlett's application of Laguerre's method is an excellent one for solving large sparse matrices in Hessenburg form. To

use this method on the transition matrix a transformation would be required. More powerful methods exist when such a transformation must be made.

4.3 MATRIX EIGENVALUE METHODS

Matrix eigenvalue methods typically fall in either of two categories: similarity transform methods or vector iterative methods. Although only the latter explicitly classifies the methods as iterative, similarity transform methods are iterative as well. Indeed, by Galois theory [26], the roots of any polynomial whose order is greater than four must necessarily be found iteratively. We will initially consider similarity transform methods and then conclude with vector iterative, or power, methods.

4.3.1 Similarity Transform Methods

Let P be a general matrix of order n . A similarity transformation (to create a similar matrix P_1)

$$P_1 = Q^{-1} P Q \quad (4-13)$$

where Q is any non-singular matrix of the same order as P , preserves the eigenvalues of the matrix P . A judicious choice of Q enables one to change the form of P so that its eigenvalues may be readily found, i.e., triangularize P .

Typically, the triangularization process requires several steps since only a few elements of P are operated on with each similarity transformation.

The most common triangularization routines available are the LR [27] and QR [28] algorithms. Both of these methods are relatively inefficient for fully populated, or dense matrices (few zero elements). However, when a matrix exhibits a certain pattern of zero's they become quite efficient. The desirable pattern of zero elements for general matrices is that which is associated with an upper Hessenburg matrix. To effectively use the QR or LR algorithms, then, one must initially transform the general matrix of interest to upper Hessenburg form. This reduction is accomplished by using either orthogonal transformations which require approximately $5n^3/3$ multiplications, or elementary stabilized transformations which require approximately $5n^3/6$ multiplications [29].

4.3.1.1 The LR Transformation

Let P_k be the matrix obtained from the $(k-1)$ -th transformation. P_k may be factored, or decomposed, as

$$P_k = L_k R_k \quad (4-14)$$

where L_k is a lower triangular matrix with unit diagonal elements and R_k is an upper triangular matrix. The updated iterate is then obtained by forming ($k=1,2,\dots$)

$$P_{k+1} = R_k L_k. \quad (4-15)$$

Combining (4-14) and (4-15) yields

$$P_{k+1} = L_k^{-1} P_k L_k \quad (4-16)$$

which establishes the similarity transform form and hence the preservation of the eigenvalues at each iteration. The ($k+1$)-th transformation may be stepped back to the original matrix P by writing

$$P_{k+1} = L_k^{-1} L_{k-1}^{-1} \dots L_1^{-1} P L_1 \dots L_{k-1} L_k. \quad (4-17)$$

It can be proven that the eigenvalues of smallest moduli tend to converge first and that the rate of convergence is dependent on the ratio of the moduli of neighboring eigenvalues [27]. By introducing origin shifts the convergence rate can be improved [19].

Approximately 2 to 3 LR transformations are required per eigenvalue. As eigenvalues are found, the amount of required computation steadily decreases due to smaller matrices which must be operated on. Approximately n^2 multiplica-

tions are required for the first few transformations, but only $3n^3$ to $4n^3$ multiplications (including the upper Hessenburg transformation) are required to obtain a full set of n eigenvalues.

A thorough theoretical discussion of the LR algorithm may be found in [19]; computational aspects may be found in [30].

The use of an orthogonal factorization introduces favorable stability and accuracy properties throughout the entire triangularization process [19]. Such a decomposition leads to the QR transformation.

4.3.1.2 The QR Transformation

When the lower triangular matrix used in the LR algorithm is replaced by an orthogonal matrix we obtain the most basic form of the QR algorithm. Letting Q_k be the k -th iterate orthogonal matrix we may write the basic steps as

$$P_k = Q_k R_k \quad (4-18)$$

and

$$P_{k+1} = R_k Q_k = Q_k^{-1} P_k Q_k = Q_k^T P_k Q_k. \quad (4-19)$$

The convergence properties of the QR method are similar to the LR in that convergence is toward the eigenvalues of least moduli, and approximately 1 to 2 double QR transformations [19] are required per eigenvalue. The orthogonal decomposition does require more computation, however. Approximately $5n^2$ multiplications are required for the first few double transformations; the entire process requires approximately $4n^3$ multiplications (including the upper Hessenburg transformation).

Although slightly more computation is required, the QR method is preferred over the LR due to its superior stability and accuracy properties for obtaining both single and multiple real and complex eigenvalues. This is the case when the original matrix is real. A version of both of these algorithms exists for complex matrices [19,30]. In practice, the complex LR algorithm has been preferred to the complex QR since it is somewhat simpler in content but comparable in stability and accuracy.

The LR and QR algorithms represent the most accurate and efficient methods available for obtaining a full set of eigenvalues from a dense matrix which has been transformed to upper Hessenburg form. A full set of corresponding eigenvectors may be obtained by accumulating the transformations used in the LR or QR reductions (this increases the number

of required multiplications by approximately a factor of two); a partial set may be obtained by using an inverse iteration method [19]. To use the LR or QR methods, however, matrices must generally be stored in full storage mode since similarity transformations typically destroy any sparse properties. Hence, these methods are only useful on matrices with orders less than a few hundred. The size of the transition matrix generated by TD-SEM can easily be on the order of thousands and therefore excludes itself from full eigensolution by these techniques. Only partial eigensolution by iterative eigenvector methods remain.

4.3.2 Iterative Eigenvector Methods

Iterative eigenvector, or power, methods may be used to find either a full, or more commonly, a partial set of eigenvalues and eigenvectors. Since only matrix multiplications, in general, are required by these methods any sparse properties of the original matrix may be taken advantage of. Iterative eigenvector methods may be divided into two classes: single vector and multiple vector methods. Both methods begin with an initial estimate or guess at an eigenvector which, hopefully, will iteratively converge to an actual eigenvector of the system. The corresponding eigenvalue is consequently found.

4.3.2.1 Single Vector Power Methods

The standard and inverse power methods represent the two single vector methods commonly used in practice. We will initially consider the standard method.

Let P be an unsymmetric matrix of order n with n independent eigenvectors. An arbitrary vector $\bar{u}^{(0)}$ (where (0) denotes the iteration number) may be expressed as a linear combination of these vectors, i.e.,

$$\bar{u}^{(0)} = c_1 \bar{q}_1 + c_2 \bar{q}_2 + \dots + c_n \bar{q}_n \quad (4-20)$$

where \bar{q}_i , c_i , $i=1,2,\dots,n$, denote the eigenvectors and arbitrary coefficients respectively. Postmultiplying P by $\bar{u}^{(0)}$ yields

$$\bar{u}^{(1)} = P\bar{u}^{(0)} = \sum_{i=1}^n c_i P\bar{q}_i = \sum_{i=1}^n \lambda_i c_i \bar{q}_i \quad (4-21)$$

where λ_i denotes the eigenvalue corresponding to \bar{q}_i . If the eigenvalues can be ordered as $|\lambda_1| > |\lambda_2| \geq \dots \geq |\lambda_n|$, then $\bar{u}^{(1)}$ should represent an approximation to the eigenvector \bar{q}_1 corresponding to the dominant eigenvalue λ_1 . This approximation will iteratively improve by forming

$$\bar{u}^{(k)} = P^k \bar{u}^{(0)} = \lambda_1^k c_1 \bar{q}_1 + \lambda_2^k c_2 \bar{q}_2 + \dots + \lambda_n^k c_n \bar{q}_n \quad (4-22)$$

since for a large enough k , $|\lambda_1|^k \gg |\lambda_2|^k$. The ratio $|\lambda_1|/|\lambda_2|$ determines how quickly the scheme will converge to some specified degree of accuracy. Convergence will be quite rapid if there exists good separation between these eigenvalues. Convergence will be very slow if this ratio is close to unity. A variety of modifications exist to speed convergence under various circumstances [19].

The inverse power method requires more computation than the standard power method, but allows one to approximate eigenvalues and eigenvectors other than the dominant ones. We begin the method with some scalar α , and some initial vector $\bar{u}^{(0)}$, and consider the iterative system ($k=0,1,2,\dots$)

$$\bar{u}^{(k+1)} = (P - \alpha I)^{-1} \bar{u}^{(k)} \quad (4-23)$$

where I is an identity matrix. Note that this is the standard power method applied to the matrix $(P - \alpha I)^{-1}$ which possesses the eigenvalues, $1/(\lambda_i - \alpha)$, $i=1,2,\dots,n$. The method converges to $1/(\lambda_j - \alpha)$, where λ_j is the eigenvalue closest to α .

From the convergence properties of the standard power method, we note the following properties of the inverse method. When α is zero, convergence is toward the least dominant eigenvalue of P . When the value of α is close to an eigenvalue, convergence will be quite rapid, but when α is a poor eigenvalue estimate, convergence may be quite slow.

In practice, the inverse observed in equation (4-23) is rarely explicitly determined. A decomposition or Gaussian elimination is used on the matrix $(P - \alpha I)$ which requires approximately $n^3/3$ multiplications. Another n^2 multiplications are required to determine each new $\bar{u}^{(k)}$ (eigenvector iterate). The standard power method does not necessitate a decomposition and is therefore more efficient than the inverse method for the same number of iterations. The number of iterations required for the inverse method, however, will be significantly smaller when a good guess at an eigenvalue is known. Typically, the two methods are used in conjunction with one another. The standard method determines a good initial guess which is then refined by the inverse method.

Once a single eigenvalue and eigenvector is known it may be filtered out of the original matrix by either purification or deflation [29]. The power methods above may then be used on this filtered matrix to find another eigenvalue and eigenvector. These may then be filtered out, and so on.

The state transition matrix is not only very sparse, but possesses a full set of eigenvalues whose moduli are less than unity. These two properties exclude the use of single vector power methods for the following two reasons: first, the purification or deflation processes which are required

to find several eigenvalues possess the unfortunate property that they destroy sparsity in general; second, the ratio of the moduli of neighboring eigenvalues is generally so close to unity that convergence is impractical in a reasonable amount of time. Experimental verification of these two complications has established that single vector power methods do not constitute a feasible method of solution for the large scale state transition matrix.

4.3.2.2 Multiple Vector Power Methods

Multiple vector methods are power methods which iterate with several vectors simultaneously. The name simultaneous iteration (S.I.) has been given to these methods.

Bauer [31] introduced the first S.I. concept, called 'Bi-Iteration'. This method solved the algebraic eigenvalue problem $P\bar{u}=\lambda\bar{u}$ for an arbitrary matrix P of order n . The idea of the method was to iterate with two sets of vectors, $\bar{u}_1, \bar{u}_2, \dots, \bar{u}_s$ and $\bar{q}_1, \bar{q}_2, \dots, \bar{q}_s$ ($s \leq n$) applied to P and P^H (H denotes Hermitian transpose) respectively. By maintaining \bar{u}_i and \bar{q}_j biorthonormal ($\bar{u}_i^H \bar{q}_j = \delta_{ij}$, where δ_{ij} is the Kronecker delta), it can be shown [31] that under certain conditions the \bar{u}_i converge to the right eigenvectors, and the \bar{q}_j converge to the left eigenvectors corresponding to the eigenvalues λ_i, λ_j .

Since the initial development of bi-iteration, emphasis has been placed on developing simplified versions with improved convergence properties. Rutishauser [32] developed an efficient computer implementable version for symmetric and positive definite matrices; an ALGOL listing may be found in Wilkinson [30]. Clint and Jennings [33] introduced a modification for unsymmetric matrices which improved convergence by using an 'interaction analysis'. An unsymmetric method which utilized an interaction analysis and required only one set of iteration vectors was subsequently developed by Jennings and Stewart [34]. The following discussion is an extension of the latter contribution.

Jennings and Stewart restrict the left and right iteration vectors to only the right set. For this set, the following iteration sequence is appropriate ($k=1,2,\dots$):

- i) $V_k = P U_{k-1}$
 - ii) $G_k = U_{k-1}^H U_k$
 - iii) $H_k = U_{k-1}^H V_k$
 - iv) $G_k D_k = H_k$
 - v) $D_k A_k = A_k \theta_k$
 - vi) $W_k = V_k A_k$
 - vii) U_k is W_k normalized.
- (4-24)

We introduce the following geometrical argument to justify this sequence of operations. Let

$$V_k = P U_{k-1} \quad (4-25)$$

where U_{k-1} contains an approximation to a subset of the eigenvectors of P . V_k may be decomposed into the sum of a projected matrix and an orthogonal matrix,

$$\begin{aligned} V_k &= V_k^{\text{proj.}} + V_k^{\text{ortho.}} \\ &= (U_{k-1} D_k) + V_k^{\text{ortho.}} \\ &= E_k T_k D_k + V_k^{\text{ortho.}} \end{aligned} \quad (4-26)$$

where E_k , T_k , and D_k are to be determined. Combining (4-25) and (4-26) yields

$$\begin{aligned} P U_{k-1} &= E_k T_k D_k + V_k^{\text{ortho.}} \\ &= E_k \partial_k T_k + V_k^{\text{ortho.}} \end{aligned} \quad (4-27)$$

if and only if

$$\partial_k T_k = T_k D_k \quad (4-28)$$

or

$$D_k A_k = A_k \partial_k \quad (4-29)$$

where $A_k = T_k^{-1}$. Equation (4-29) defines an eigenvalue problem for D_k ; the eigenvalues of D_k are given by the matrix θ_k , while the eigenvectors of D_k are given by the matrix A_k . D_k is found by solving the linear system

$$U_{k-1}^H V_k = (U_{k-1}^H U_{k-1}) D_k \quad (4-30)$$

The updated iterate is then

$$W_k = V_k A_k = U_{k-1} (D_k A_k) + V_k^{\text{ortho.}} A_k \quad (4-31)$$

where U_k is a normalized W_k . Note that in the iteration cycle an approximation which ignores the contribution of the second term on the right of equation (4-31) is made. This approximation is reasonable since the second term tends to zero as the number of iterations becomes large (due to A_k approaching a span of the projection space).

This sequence of steps is appropriate for a right eigenvector or V_k projection scheme. A similar sequence may be developed for a U_{k-1} projection scheme. In the latter case convergence is toward the reciprocal eigenvalues.

A few comments are in order about the sequence of steps in the iteration cycle. U_0 represents the initial guess to a dominant block of eigenvectors which may be with real numbers. The entire process proceeds in real arithmetic until the 'interaction matrix', D_k , possesses complex eigenvalues;

the process then becomes complex. When this transition is made, G_k becomes a positive definite Hermitian matrix for which a modified Cholesky decomposition has been developed to minimize the operations required for the solution of step iv.

If U_k contains s approximations to s eigenvectors ($s \leq n$, where n again is the order of the original matrix P), then the matrix θ_k contains s approximations to s eigenvalues. It can be shown [34] that the rate of convergence of the above sequence is dependent on the ratio $|\lambda_1|/|\lambda_{s+1}|$ and not on the ratio $|\lambda_1|/|\lambda_2|$ which governs the single vector methods. Convergence is toward the dominant eigenvalues.

For certain geometries (Section 5.3.2) the eigenvalues associated with the state transition matrix exhibit a well defined series of annular rings. Within each of these rings the eigenvalues are of comparable moduli. Between rings there is a significant jump in moduli. Since the convergence rate of the simultaneous iteration scheme above is dependent on the ratio of neighboring blocks of eigenvalues instead of the ratio of neighboring eigenvalues, and since the scheme requires only matrix multiplications which preserve sparsity, simultaneous iteration represents a reasonable method for obtaining a partial set of eigenvalues and eigenvectors for \ddagger . Theoretically, rings may be found one by one until a desired set is collected.

A complication with this method is the number of multiplications required per iteration. For a real arithmetic cycle approximately [29]

$$ncs + \frac{5}{2} ns^2 + \frac{31}{6} s^3 \quad (4-32)$$

multiplications are required. Here, c denotes the average number of nonzero elements in each row of the matrix whose eigensolution is sought, n denotes the order of this matrix, and s denotes the number of eigenvalues desired. For a complex cycle this number increases approximately by a factor of four.

As the order of the matrix whose eigenvalues are sought increases, the separation between neighboring blocks of eigenvalues typically decreases, and therefore, more iterations are required to obtain a specified degree of accuracy. It can be shown that the approximate number of required iterations (k) to obtain a certain degree of accuracy is

$$k \approx \ln \epsilon / \ln |\lambda_1 / \lambda_{s+1}| \quad (4-33)$$

where s denotes the block size, and ϵ denotes the accuracy desired, i.e., 0.0001, 0.001, etc.. Figure 5.9 (Section 5.3.2) illustrates size of the state transition matrix vs. execution time required on an IBM 3032 computer for a parti-

cular subset of eigenvalues. Figure 5.10 illustrates storage requirements for both the QR and S.I. methods.

A significant reduction in the number of multiplications required per iteration may be accomplished by taking advantage of the form of the eigenvectors associated with the transition matrix. For simplicity, equation (3-32) is repeated here as

$$\bar{K}_\alpha^T = [z_\alpha^{N_T-T} \bar{v}_\alpha^T, z_\alpha^{N_T-1} \bar{v}_\alpha^T, \dots, \bar{v}_\alpha^T] \quad (4-34)$$

where z_α denotes a particular eigenvalue, and \bar{v}_α denotes a vector spatially describing the natural mode. Since the entire state vector \bar{K}_α can be constructed once these two parameters are known, it should be possible to carry out the simultaneous iteration cycle with only a subset of the state vector. Under certain conditions this is possible and has been given the name 'sub' iteration.

The sub iteration modification may only be used after the proper form of the entire state vector has appeared. This can typically take several iterations since the vectors are constructed from the top down. A sophisticated computer program which incorporates this idea has shown that the desired form cannot be forced in general, it must appear naturally. Once the form appears, however, the use of sub iteration for the remaining iterations will drastically reduce

the execution time. A listing of this routine (which was designed for the solution of the thin-wire problem (Chapter 5)) may be found in Appendix A. Random sparse storage techniques [29] were used in this algorithm to store the state transition matrix.

Of all methods tested, simultaneous iteration with the sub iteration modification represents the only feasible method for the partial eigensolution of the large scale state transition matrix. The amount of computation time required using this scheme can admittedly become excessive as the system size becomes very great. However, it should be realized that even if it were possible to place these large matrices in the high speed store of the largest computers so that the efficient QR or LR algorithms could be used to find both the eigenvalues and eigenvectors, the amount of computation time would be at least as great if not greater than the time required by S.I.. This may be established simply by considering the total number of operations each scheme requires. The time required by the QR and LR methods would be for a full set of eigenparameters as opposed to the partial set given by S.I., however.

Chapter V

WIRE-STRUCTURE ANALYSIS

5.1 INTRODUCTION

Wire structures may be analyzed either as scatterers or antennas. When an incident wave propagating in space excites a response on the wire, we consider the structure to be a scatterer. When the wire is excited from small regions on the structure itself, it is considered an antenna.

In this chapter, we will consider both frequency- and time-domain numerical solution techniques. The discussions will be restricted to thin, perfect conducting wires situated in one-dimensional or linear geometries. Frequency-domain methods are presented in Section 5.2. By applying the widely used moment method [14] to the EFIE for thin, perfect conducting surfaces, the current and electric field distributions along the antenna are obtained. A discussion of excitation models is presented in Section 5.2.1; and a discussion of the applicability of the thin-wire kernel approximation is presented in Section 5.2.2. In Section 5.3, time-domain techniques are discussed. By using finite difference approximations, we obtain the transient current distribution associated with the antenna mode of operation; and by applying the TD-SEM method, we present the SEM pole

distribution associated with the scattering mode. The effect of varying the time-sampling distance used in the finite difference approximation on the pole locations is presented in Section 5.3.2.1. In Section 5.3.3, the effect of segment to segment (unknown to unknown) coupling through the kernel of the EFIE on the pole locations is discussed.

Extensive studies on approximate analytic solution techniques of linear wire structures have been given by King [35]. Numerical solution techniques have been given by Harrington [14], Poggio and Mayes [36], Thiele [37], and Mittra [38]. These provide excellent discussions of methods for obtaining most any desired antenna or scattering parameter other than the pole structure. A complete discussion and several references for obtaining the natural responses of objects in both the frequency- and time-domains may be found in Chapter 3.

5.2 SPACE-FREQUENCY TECHNIQUES

The appropriate expression which describes thin, perfect conducting structures is (2-11a). For one-dimensional problems with geometries similar to the geometry depicted in Figure 5.1, this expression may be written in terms of an unknown current, \tilde{I}_z , and magnetic vector potential, \tilde{A}_z , as

$$-\tilde{E}_z^{\text{inc}}(a, z, \omega) = \frac{1}{j\omega\epsilon_0} \left[k^2 + \frac{\partial^2}{\partial z^2} \right] \tilde{A}_z(a, z; \omega) \quad (5-1)$$

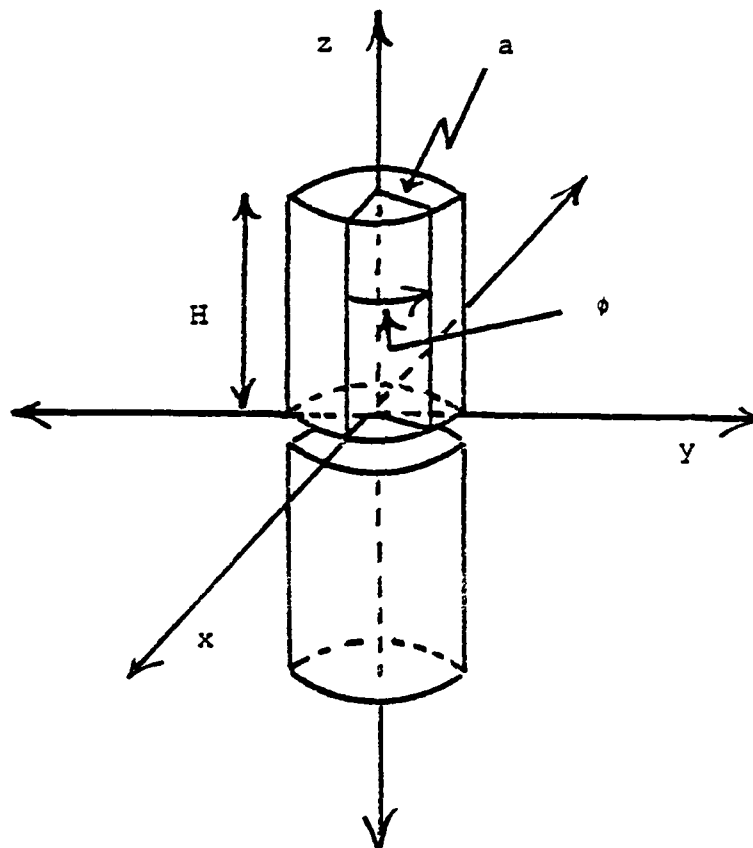


Figure 5.1: Wire geometry.

where

$$\tilde{A}_z(a, z, \omega) = \frac{1}{2\pi} \int_{-H}^H \int_0^{2\pi} \frac{\tilde{I}_z(z') e^{-jkR}}{4\pi R} d\phi' dz' \quad (5-1a)$$

with

$$R = ((z-z')^2 + 2a^2 - 2a^2 \cos \phi')^{1/2} \quad (5-1b)$$

Expression (5-1) was originally presented by Pocklington in 1897. Various alternate forms of the expression are possible by manipulating the position of the operator, $[k^2 + \partial^2 / \partial z^2]$. For numerical work, this operator is often preferred outside the integral so that integration of a more highly singular kernel is avoided. We will only consider the Pocklington form in this chapter.

The vector potential \tilde{A}_z may be written in terms of a Green's function, \tilde{G} , as

$$\tilde{A}_z(a, z; \omega) = \int_{-H}^H \tilde{G}(z, z'; \omega) \tilde{I}_z(z') dz' \quad (5-2)$$

where

$$\tilde{G}(z, z'; \omega) = \frac{1}{2\pi} \int_0^{2\pi} \frac{e^{-jkR}}{4\pi R} d\phi' \quad (5-3)$$

is commonly known as the exact kernel for the thin-wire problem. A computationally simpler kernel may be used under certain conditions. This kernel is defined to be the approximate thin-wire kernel, $\tilde{G}_a(z, z')$, and is given by

$$\tilde{G}_a(z, z') = \frac{1}{4\pi} \frac{e^{-jkR_a}}{R_a} \quad (5-4)$$

where

$$R_a = [(z-z')^2 + a^2]^{1/2} \quad (5-4a)$$

King [39] has noted that the results obtained for a tubular antenna are nearly identical for either this kernel or the exact one. It should be pointed out, however, that it is possible to obtain numerically unstable results using the approximate kernel (Section 5.2.2).

King [35] has analytically shown that the current distribution on a linear antenna is sinusoidal in form. Therefore, the use of the method of moments (MoM) [14] with a subsectional basis set of piecewise sinusoids is a sensible approach for obtaining numerical solutions for expression (5-1). A brief outline of how the choice of this basis set in conjunction with the MoM may be used for the discretization follows.

We let the structure of interest be uniformly divided into $(N+1)$ pieces each of length Δ . The current distribution may then be approximated as

$$\tilde{I}'(z') = \sum_{n=1}^N \tilde{I}_n S_n \quad (5-5)$$

where

$$S_n = \begin{cases} \frac{\sin(k(\Delta - |z' - z_n|))}{\sin k\Delta} & |z' - z_n| < \Delta \\ 0 & \text{otherwise} \end{cases} \quad (5-5a)$$

denotes the piecewise sinusoids, and the constants \tilde{I}_n are to be determined. By substituting this approximation into equation (5-2), we may write a discrete version of expression (5-1), after several straightforward manipulations, as

$$-E_z^{\text{inc}} = \sum_{n=1}^N \tilde{I}_n \tilde{L}_{\text{op}}(S_n) \quad (5-6)$$

where the operator $\tilde{L}_{\text{op}}(S_n)$ is given by

$$\frac{k}{j\omega\epsilon_0 \sin k\Delta} [\tilde{G}(z - (z_n + \Delta)) + \tilde{G}(z - (z_n - \Delta)) - 2\cos(k\Delta)\tilde{G}(z - z_n)]. \quad (5-6a)$$

Here, the arguments of the function G replace $(z - z')$ in either equation (5-1b) or (5-4a) depending on whether the exact or approximate kernel is used.

Following the McM formalism, we introduce a pulse testing function, w_m , such that

$$w_m = P_{\Delta}(z-z_m) \quad (5-7)$$

where

$$P_{\Delta}(z-z_m) = \begin{cases} 1 & |z-z_m| < \Delta/2 \\ 0 & \text{otherwise.} \end{cases} \quad (5-7a)$$

Equation (5-6) may now be written as

$$\langle w_m, -\tilde{E}_z^{\text{inc}} \rangle = \sum_{n=1}^N \tilde{I}_n \langle w_m, \tilde{L}_{\text{op}}(S_n) \rangle \quad (m = 1, 2, \dots, N) \quad (5-8)$$

where

$$\begin{aligned} \langle w_m, \tilde{L}_{\text{op}}(S_n) \rangle = & \\ & \frac{k}{j\omega\epsilon_0 \sin(k\Delta)} \int_{m\Delta-\Delta/2}^{m\Delta+\Delta/2} [\tilde{G}(z-(z_n+\Delta)) + \tilde{G}(z-(z_n-\Delta)) - 2 \cos(k\Delta) \tilde{G}(z-z_n)] dz \end{aligned} \quad (5-8a)$$

and $\langle w_m, -\tilde{E}_z^{\text{inc}} \rangle$ is similarly defined. Equation (5-8) has the matrix representation

$$\begin{bmatrix} \langle w_1, \tilde{L}_{op}(S_1) \rangle & \cdots & \langle w_1, \tilde{L}_{op}(S_N) \rangle \\ \vdots & & \vdots \\ \langle w_N, \tilde{L}_{op}(S_1) \rangle & \cdots & \langle w_N, \tilde{L}_{op}(S_N) \rangle \end{bmatrix} \begin{bmatrix} \tilde{I}_1 \\ \vdots \\ \tilde{I}_N \end{bmatrix} = \begin{bmatrix} \langle w_1, -\tilde{E}_z^{inc} \rangle \\ \vdots \\ \langle w_N, -\tilde{E}_z^{inc} \rangle \end{bmatrix} \quad (5-9)$$

The matrix with components $\langle w_m, \tilde{L}_{op}(S_n) \rangle$ is known as an impedance matrix \tilde{Z} , and the vector with components $\langle w_m, -\tilde{E}_z^{inc} \rangle$ is known as a voltage vector \tilde{V} . Using this notation, the current coefficients \tilde{I}_n may be found by forming

$$\tilde{I}_n = \tilde{Z}^{-1} \tilde{V} \quad (5-10)$$

assuming a non-singular impedance matrix.

All frequency-domain results in this chapter will be based on this model.

5.2.1 Excitation Models

The impedance matrix is invariant to the form of excitation; only the voltage vector reflects this. In the antenna mode, the excitation may be modeled in a variety of ways. The simplest is the delta function [37] gener-

which introduces a single entry of unity into the voltage vector; its position in the vector corresponds to the position of the excitation on the antenna. An alternate, and more rigorous, method of excitation modeling is the use of equivalent magnetic sources. This leads to magnetic frill [37] generators and belt [40] generators. The voltage vector reflects this form of excitation in the form of a distribution with unit area. Results induced by these different models are nearly identical everywhere over the structure except directly at the point where the excitation is originating. This point is somewhat critical to the overall analysis; however, since impedance and admittance characteristics are dependent on the magnitude of the current at this point. It has been found [40] that the magnetic source generator models yield impedance and admittance values in better agreement with experimental measurements than delta generator models. Figure 5.2 compares a delta generator with a magnetic belt generator for a half-wavelength antenna using the exact kernel. Numerically, the results differ only at and near the feed point; graphically the difference is indistinguishable.

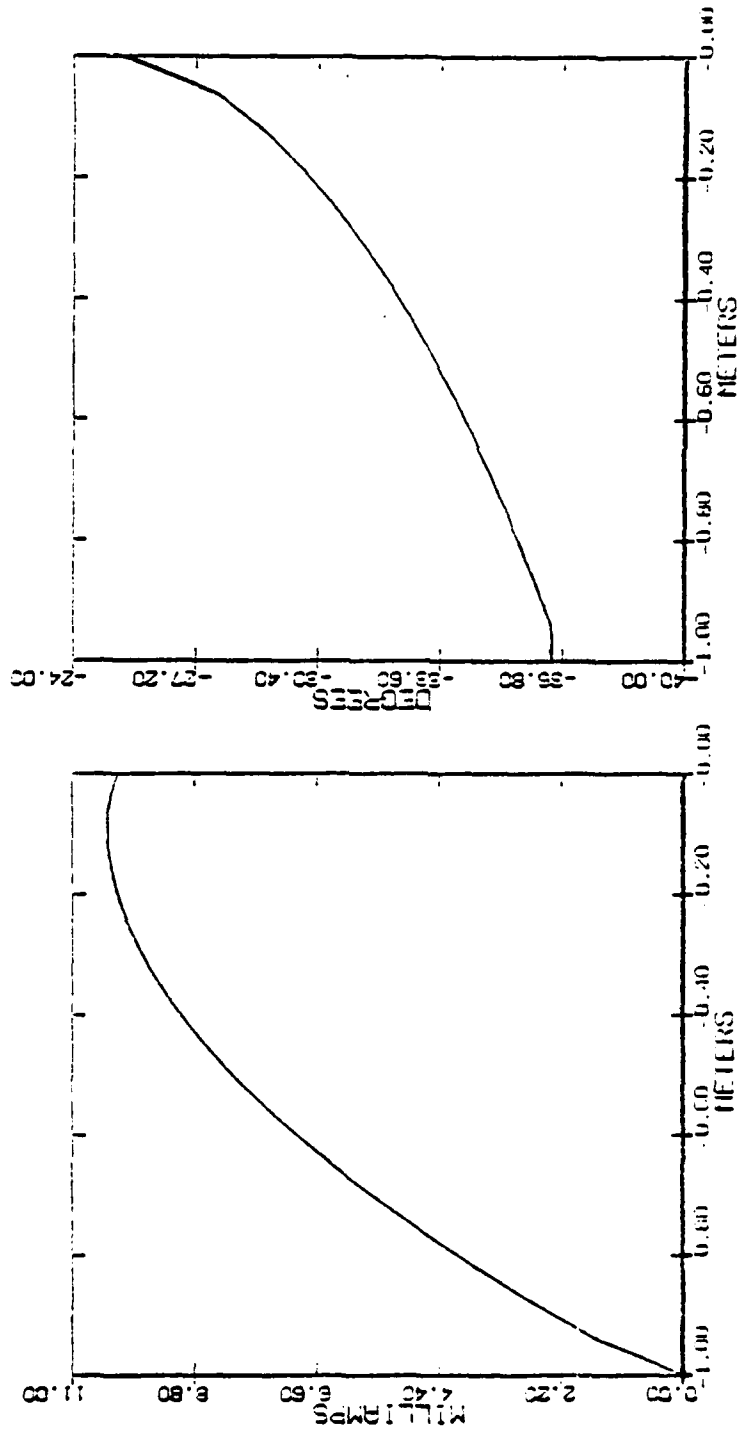


Figure 5.2a: Magnitude

Figure 5.2b: Phase

Figure 5.2: Current distribution on a 2 meter dipole antenna with a radius of 0.01 meters. The number of unknowns was 31, and the frequency of operation was 75 MHz.

5.2.2 Thin-Wire Kernel Approximation

Equation (5-4) denotes the thin-wire kernel approximation which is analytically valid for wires that are only a small fraction of a wavelength in diameter. A numerical complication can arise using this kernel even when the wire is electrically and hence the approximation analytically valid. When the sampling distance between unknowns is on the order of the radius of the structure, non-physical current oscillations may appear both at the end points and the feed point. Use of the exact kernel in such cases avoids this complication. Figure 5.3 compares the effect of the exact and approximate kernels on the current distribution of a 1 meter antenna. A belt generator was used for the excitation.

5.2.3 Electric Field Distribution

Once the current coefficients are obtained from equation (5-10), the scattered tangential electric field distribution may be found by evaluating

$$\tilde{E}_z^s(a, z; \omega) = \frac{30j}{\sin(kL)} \sum_{n=1}^N \tilde{I}_n \left[\frac{e^{-jkR_1}}{R_1} + \frac{e^{-jkR_2}}{R_2} - 2\cos(k\Delta) \frac{e^{-jkR_3}}{R_3} \right] \quad (5-11)$$

where

$$R_1 = [(z - (z_n + \Delta))^2 + a^2]^{1/2} \quad (5-11a)$$

$$R_2 = [(z - (z_n - \Delta))^2 + a^2]^{1/2} \quad (5-11b)$$

$$R_3 = [(z - z_n)^2 + a^2]^{1/2}. \quad (5-11c)$$

Note that the approximate thin-wire kernel has been used. Figure 5.4 shows $\tilde{E}_z^s(z)$ for a 1 meter antenna. A delta generator at the origin was used for the excitation.

5.3 SPACE-TIME TECHNIQUES

For one-dimensional structures corresponding to Figure 5.1, expression (2-12a) may be written as

$$\frac{\partial}{\partial t} E_z^{\text{inc}}(z; t) = \frac{1}{\epsilon_0} \left[\frac{1}{c^2} \frac{\partial^2}{\partial t^2} - \frac{\partial^2}{\partial z^2} \right] \int_{-H}^H \frac{I_z(z'; t - |z - z'|/c)}{4\pi R_a} dz' \quad (5-12)$$

where the approximate thin-wire kernel (equation (5-4)) has been used, and the current density appearing in expression (2-12a) has been replaced by the total current.

The discretization of this expression will follow the technique developed in Section 3.3.1. We assume (from expansion (3-17)) that the current distribution may be approximated as

$$I'(z'; t) = \sum_{n'=1}^N \sum_{p=-\infty}^{\infty} I_{n', p'} P_{\Delta t}(ct - p'\Delta t) P_{\Delta}(z' - n'\Delta) \quad (5-13)$$

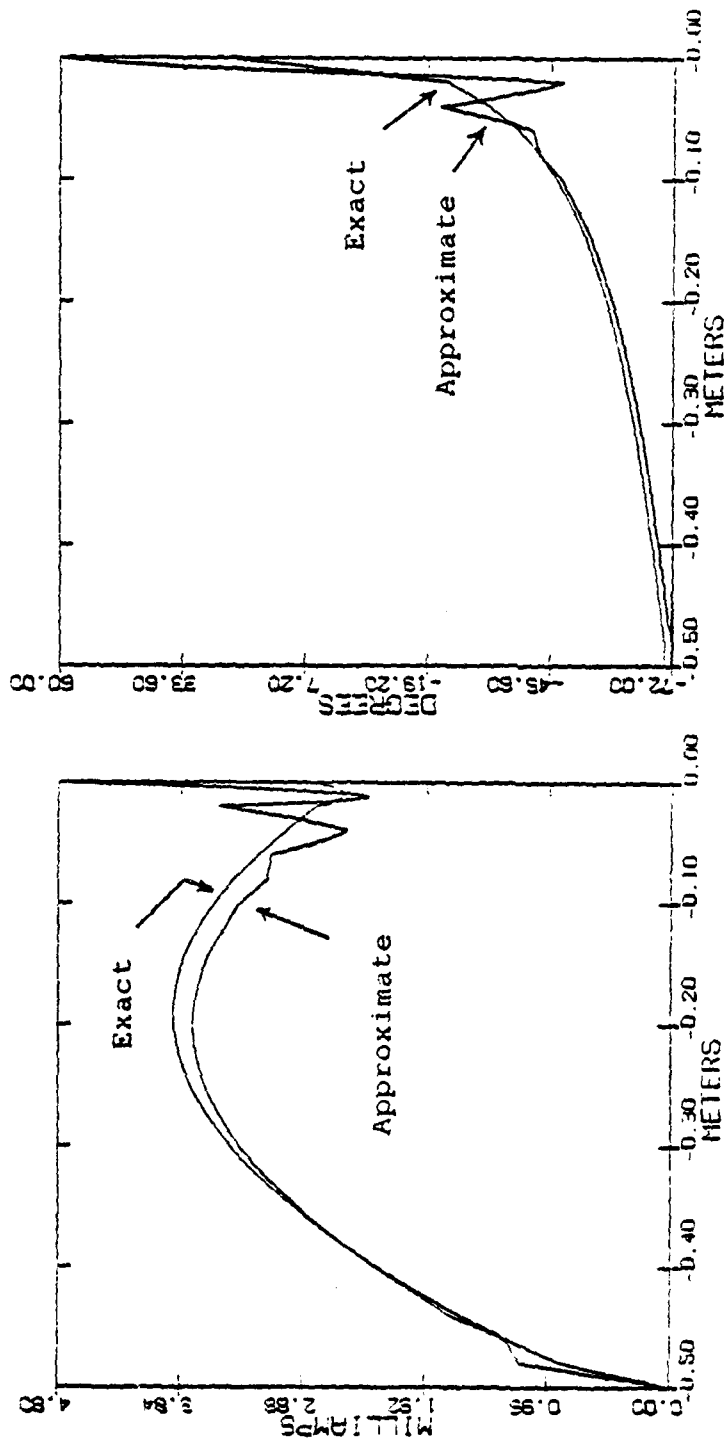


Figure 5.3a: Magnitude

Figure 5.3b: Phase

Figure 5.3: Effect of the exact and approximate kernels on the current distribution of a 1 meter antenna with a radius of 0.02 meters. The number of unknowns was 49, and the frequency of operation was 214.3 MHz.

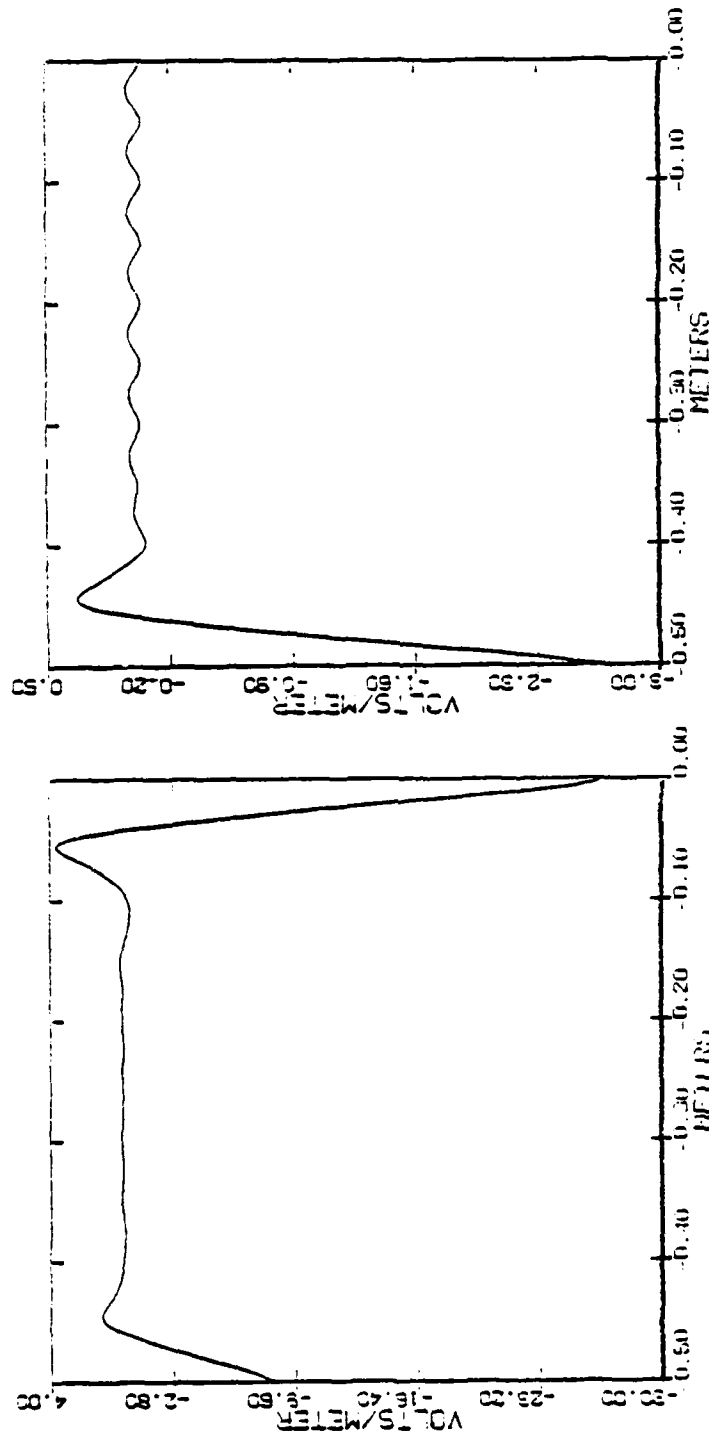


Figure 5.4a: Real Portion

Figure 5.4b: Imaginary Portion

Figure 5.4: Scattered tangential electric field distribution of a 1 meter antenna with a radius of 0.02 meters. The number of unknowns was 19, and the frequency of operation was 209.8 MHz.

where N denotes the number of unknowns used in the discretization. With this expansion, the discrete vector potential is given by

$$A_z(n\Delta; p\Delta t) = \sum_{n'=1}^N \sum_{p'=-\infty}^{\infty} I_{n',p'} P_{\Delta t}(c(p\Delta t) - p'(c\Delta t) - |n-n'|\Delta) \left[\frac{dz}{4\pi(a^2+z^2)^{1/2}} \right]_{(|n-n'|+1/2)\Delta}^{(|n-n'|-1/2)\Delta} \quad (5-14)$$

Note that the time pulse has been pulled out of the integral. This is valid only for very thin, linear structures.

By letting G_α denote the integral appearing in (5-14), and picking $p' = p - |n-n'|$ (note that this assumes the choice $c\Delta t = \Delta$), we may write the vector potential as

$$A_z(n\Delta; p\Delta t) = \sum_{n'=1}^N I_{n', p-|n-n'|} G_{|n-n'|} \quad (5-15)$$

where

$$G_\alpha = \frac{1}{4\pi} \ln \left[\frac{(\alpha+1/2)\Delta + ((\alpha+1/2)^2\Delta^2 + a^2)^{1/2}}{-(\alpha-1/2)\Delta + ((\alpha-1/2)^2\Delta^2 + a^2)^{1/2}} \right]. \quad (5-15a)$$

By transforming the continuous differential operators appearing in expression (5-12) to central finite difference operators, we obtain the following explicit scheme for the unknown current coefficients:

$$\begin{aligned}
I_{n,p+1} = & \frac{\Delta^2}{G_0} \left(\frac{\partial}{\partial t} E_z^{\text{inc}}(z;t) \right) + I_{n+1,p} + I_{n-1,p} - I_{n,p-1} + \\
& + \frac{1}{G_0} \sum_{\substack{n'=0 \\ n' \neq n}}^{N+1} G_{|n-n'|} \left[I_{n'+1,p-|n-n'|} + I_{n'-1,p-|n-n'|} - I_{n',p+1-|n-n'|} \right. \\
& \left. - I_{n',p-1-|n-n'|} \right] \begin{cases} n = 1, 2, \dots, N \\ p = 1, 2, \dots \end{cases} \quad (5-16)
\end{aligned}$$

where G_0 is the self patch kernel, and I_{-1} , I_{N+1} , I_{N+2} , I_0 are defined to be zero.

We now consider the choice $c\Delta t = \Delta$ by performing a Fourier stability analysis (Section 3.3.1) on the homogeneous differential equation for the vector potential. The vector potential is analyzed for simplicity; the stability requirement for the current equation is anticipated to be similar due to integral relation between the two. The following discussion outlines the technique.

We begin with the one-dimensional wave equation for the vector potential

$$\frac{1}{c^2} \frac{\partial^2}{\partial t^2} A_z = \frac{\partial^2}{\partial z^2} A_z \quad (5-17)$$

which in explicit differenced form becomes

$$\begin{aligned}
A_{z,n,p+1} = & r^2 \left(A_{z,n+1,p} + A_{z,n-1,p} - 2 A_{z,n,p} \right) \\
& + 2 A_{z,n,p} - A_{z,n,p-1} \begin{cases} n = 1, 2, \dots, N \\ p = 1, 2, \dots \end{cases} \quad (5-18)
\end{aligned}$$

where $r^2 = (c\Delta t/\Delta)^2$, and $A_{z_{n,p}} = A_z(n\Delta; p\Delta t)$. Discrete separation of variable techniques then leads us to a solution of the form

$$A_{z_{n,p}} = \omega^p \exp(j\alpha n\Delta) \quad (5-19)$$

where $\omega = \exp\{s\Delta t\}$ (s is arbitrary and may be complex), and α is an arbitrary real number. Clearly, for this solution to remain bounded for all p , the magnitude of ω must be bounded above by unity. By substituting this general solution into the basic equation (5-18), we obtain the following quadratic equation in ω :

$$\omega^2 - 2(1 - 2r^2 \sin^2(\alpha\Delta/2))\omega + 1 = 0 \quad (5-20)$$

From this equation, the magnitude of ω is less or equal to unity for $r \leq 1$. Therefore, the choice $c\Delta t = \Delta$ may yield a stable solution for the current coefficient difference equation (equation (5-16)). Certainty cannot be ascertained for the following two reasons: first, any appropriate boundary conditions have not been included in the analysis; and second, a difference equation for the vector potential has been considered rather than a difference equation for the current coefficients. The matrix stability method (Section 3.3.1) must be applied to the current difference scheme for this criterion to be numerically rigorous.

5.3.1 Transient Current Response

Figure 5.5 depicts the transient current response obtained from equation (5-16) on one of two feed segments for a 1 meter dipole antenna. The mathematical representation of the excitation used on each of these segments is given by

$$\frac{E_0}{2} \exp\left[-g^2(t-t_{\max})^2\right] \quad (5-21)$$

where E_0 is the free-space impedance 120π , t_{\max} is the time when the magnitude of the pulse peaks, and g is the compression factor of the pulse. The parameter t_{\max} was chosen to be 0.5 light meters (LM), and g was chosen so that the magnitude of the pulse at $t=0$ and $t=1$ LM was $0.0001/(60\pi)$ volts/meter.

5.3.2 TD-SEM Pole Distribution

The TD-SEM technique developed in Section 3.3.1 may be applied to the difference scheme of equation (5-16). The eigenvalues of the state transition matrix Φ may be found by the methods given in Chapter 4. The order of Φ for this problem is $N(N+1)$, where N represents the number of unknowns. For $N \leq 18$ full eigensolution by the QR transformation (Section 4.3.1.2) is recommended. For larger values of N , partial eigensolution by simultaneous iteration (Section 4.3.2.2) is recommended. Figure 5.6 shows the pole distri-

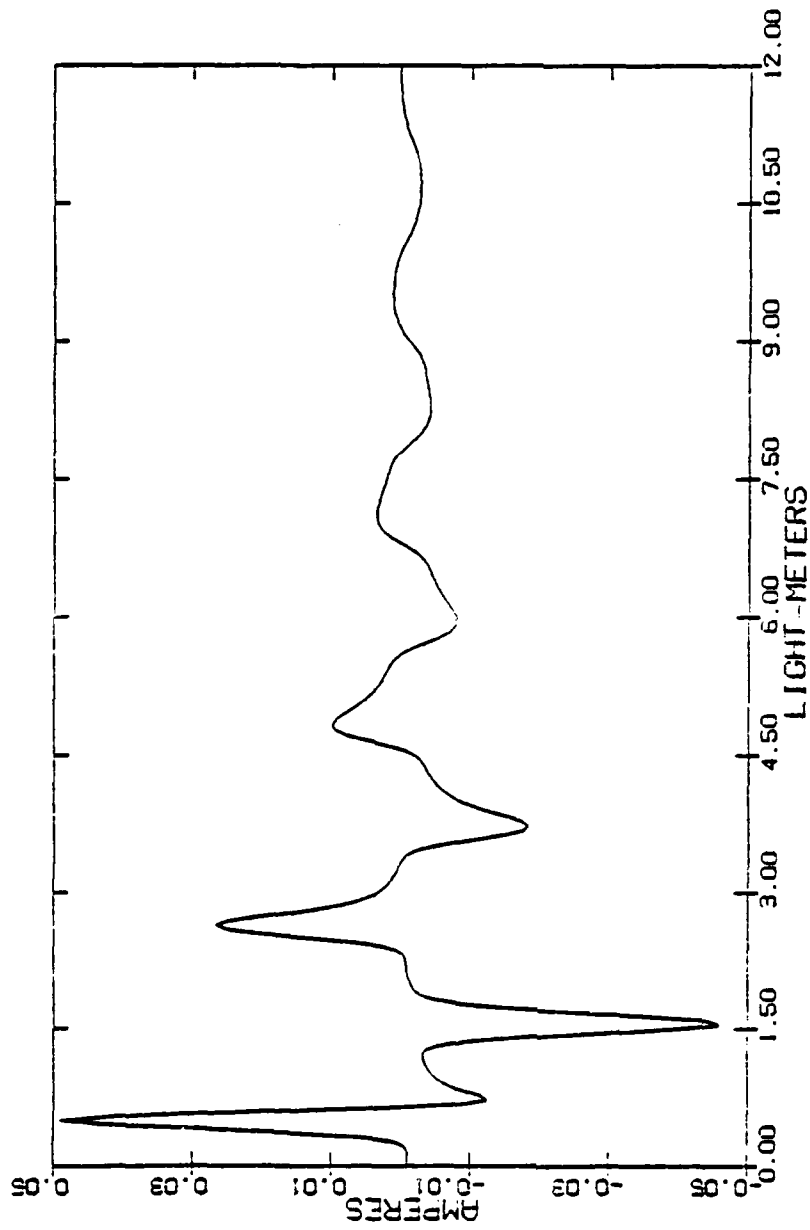


Figure 5.5: Transient current distribution on one of two feed segments of a 1 meter antenna with a radius of 0.00754 meters. The number of unknowns was 22.

bution obtained by TD-SEM (QR solution) for a 1 meter scatterer with a radius of 0.005 meters discretized with 18 unknowns such that $\Delta=1/(N+1)=1/19$. The results have been scaled by $1/(\pi c)$, and a comparison with the frequency-domain results of Singaraju, Giri and Baum [15] has been made. The results shown reflect only the second quadrant of poles since the complex conjugates may be obtained by symmetry.

A few remarks on the structure of the eigenvalues associated with this problem for the choice $c\Delta t=\Delta$ should be made. From stability, all eigenvalues must fall within the unit circle in the complex plane. Complex eigenvalues appear in groups of four which graphically define a square. Several groups of nearly identical moduli form annular rings. Real or purely imaginary eigenvalues appear in pairs of equal moduli but differing sign. The eigenvalues of interest are those with positive real components. Those with negative real components are conjectured to correspond to false poles which have no true physical meaning (this conjecture is discussed in Section 5.3.2.1). The layering structure of the poles corresponds to the annular ring structure of the eigenvalues. For an even number of unknowns, $2N$ of the eigenvalues in the outermost annular ring correspond to the significant poles contained within the first layer, while $2N-2$ eigenvalues correspond to the poles of the second layer.

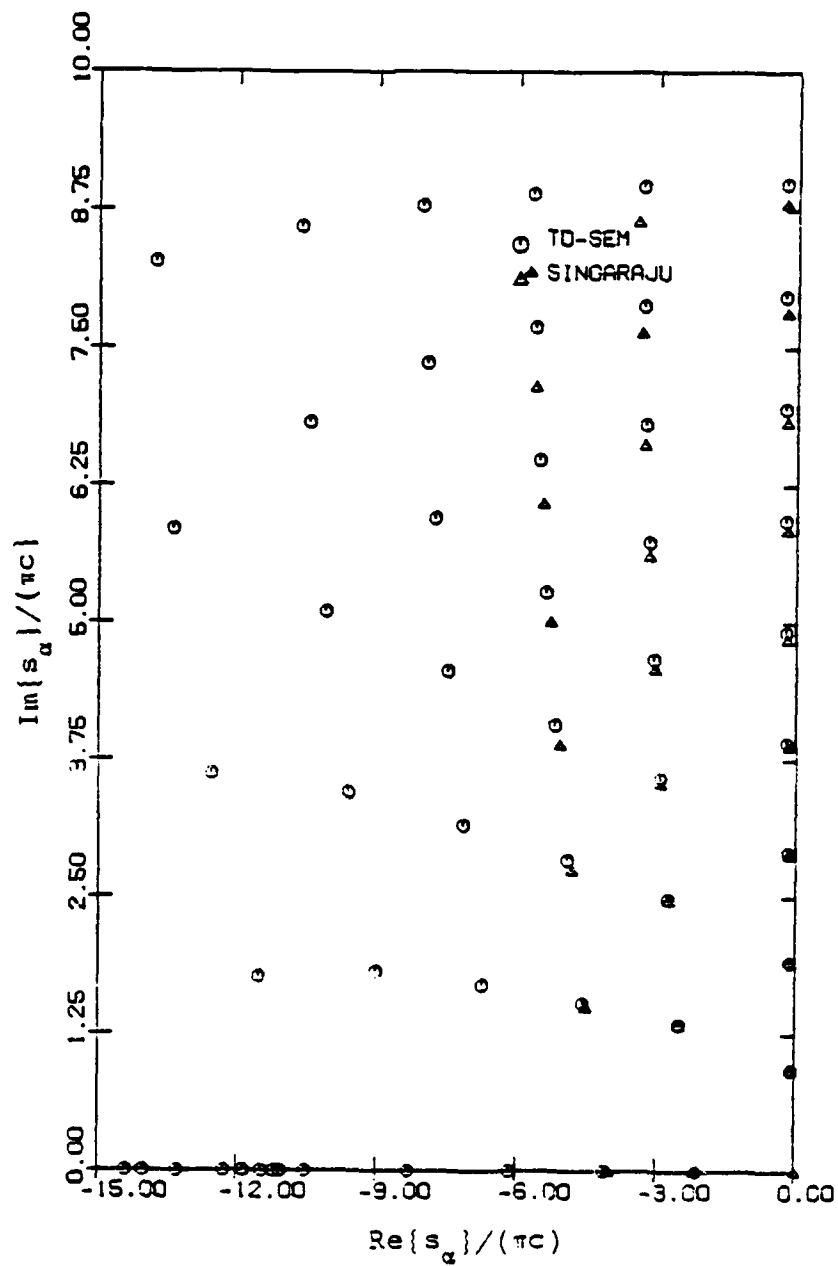


Figure 5.6: Pole distribution for 18 unknowns. The length of the scatterer was 1 meter, and the radius was 0.005 meters.

AD-A129 794

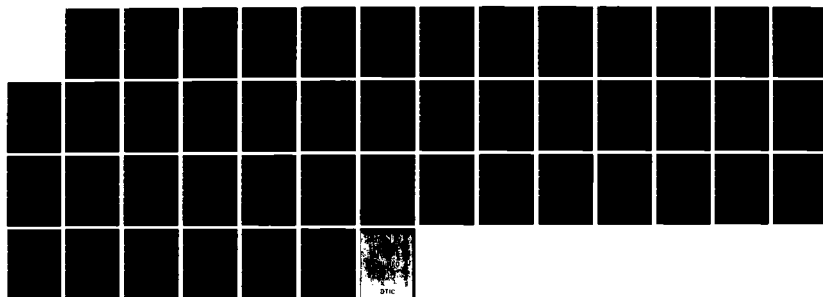
TIME DOMAIN TECHNIQUES IN THE SINGULARITY EXPANSION
METHOD(U) VIRGINIA POLYTECHNIC INST AND STATE UNIV
BLACKSBURG W A DAVIS ET AL. MAY 83 AFWL-TR-82-156
F29601-81-K-0019

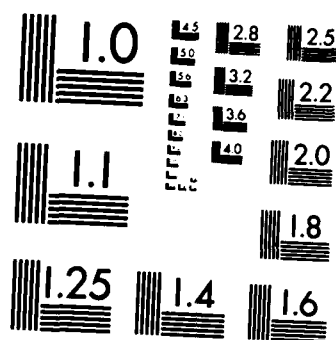
2/2

UNCLASSIFIED

F/G 12/1

NL





MICROCOPY RESOLUTION TEST CHART
NATIONAL BUREAU OF STANDARDS-1963-A

Further layers which are well defined have successively 4 fewer eigenvalues than the preceeding layer. For an odd number of unknowns a factor of 2 must be added to the numbers above. Figure 5.7 depicts the eigenvalue structure for 18 unknowns. The quadrant which is blocked off denotes the eigenvalues of interest.

Figure 5.8 shows the first layer pole distribution for 32 unknowns as found by simultaneous iteration techniques with the sub iteration modification. It should be noted that a simultaneous iteration algorithm may be used to find more layers than just the first. Additional layers may be found on a single computer execution or multiple, independent executions.

Figure 5.9 compares execution time requirements (on an IBM 3032 computer using FORTRAN H EXTENDED (OPT=2)) with the order of the state transition matrix for: full eigensolution by the QR algorithm (eigenvalues only), QR algorithm (both eigenvalues and eigenvectors), and first layer eigenvalues and eigenvectors by simultaneous iteration (assuming complex iteration cycles) with and without the sub iteration modification. IBM double precision was found to be necessary when the QR algorithm was used; IBM single precision was sufficient for the simultaneous iteration method. The curves in Figure 5.9 reflect these precision requirements.

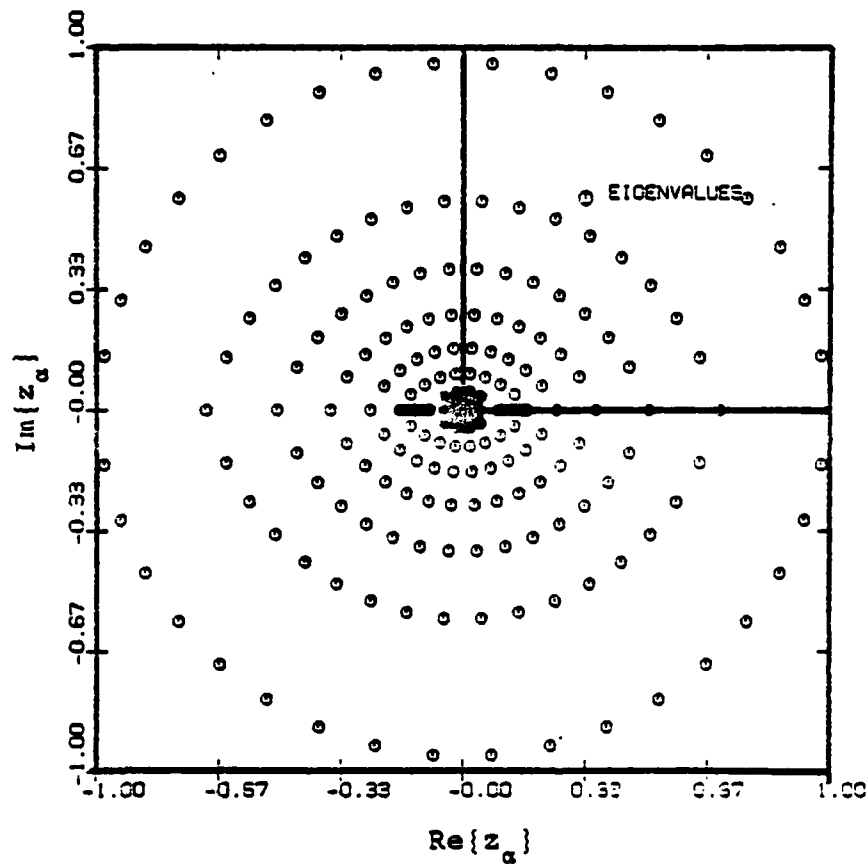


Figure 5.7: Eigenvalue structure for 18 unknowns. The length of the scatterer was 1 meter, and the radius was 0.005 meters.

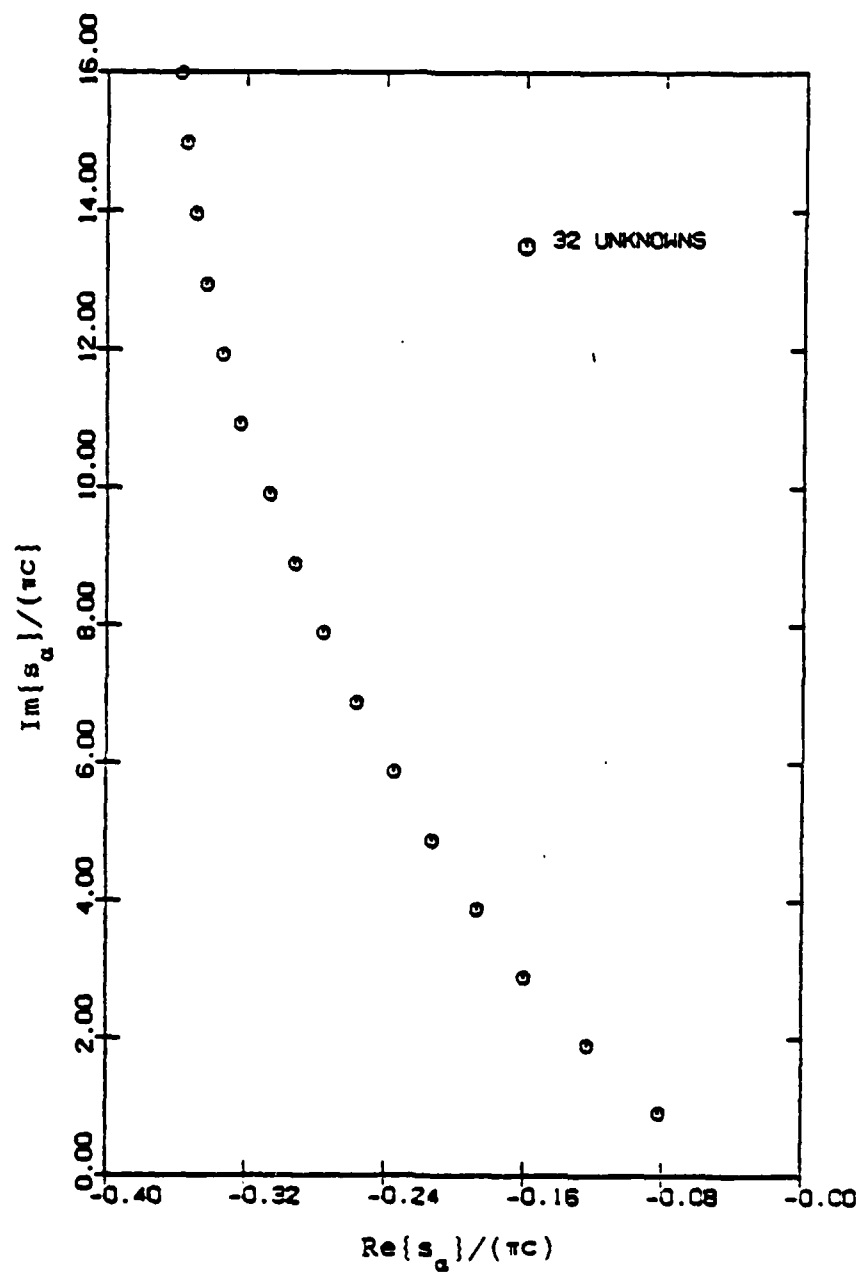


Figure 5.8: First layer pole distribution found by S.I. for 32 unknowns. The scatterer was 1 meter in length, and the radius was 0.005 meters.

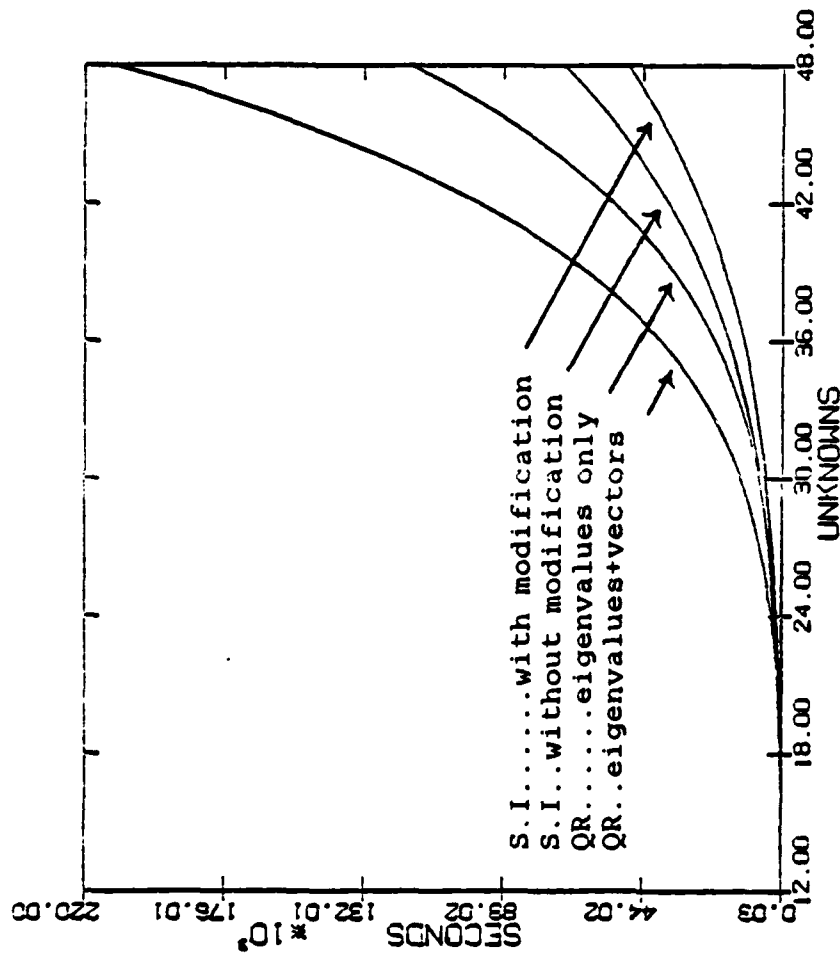


Figure 5.9: Execution time requirements on an IBM 3032 computer using FORTRAN H EXTENDED (OPT=2) for various eigensolution methods.

Figure 5.10 compares storage requirements with the transition matrix order for the cases above. The IBM double precision storage requirement for the QR algorithm, eigenvalues only, is $8n^2$ (where n denotes the order of \mathbf{A}). This requirement becomes $8n^2 + 16n^2$ when both the eigenvalues and all eigenvectors are desired. The single precision storage requirement of simultaneous iteration is $4(4k^2 + (3+2N)k + 2nk + 3((2N-1)N))$, where k denotes the number of eigenvectors sought, and N denotes the number of unknowns (for Figure 5.10, $k=2N$ was chosen; this defines the first layer).

5.3.2.1 Effect of Varying the Time Sampling Distance

The pole structure presented in Figures 5.6 and 5.7 is for the choice $c\Delta t = \Delta$. When $c\Delta t$ is chosen to be less than Δ , complications arise. Since each time step is smaller, more time steps are required for a wave to travel the length of the structure. This causes the size of the state transition matrix to increase, and thereby possess a larger number of eigenvalues. The relation of these extra eigenvalues to the true poles of the system is of interest. It has been found that the additional eigenvalues add additional 'poles' which may be divided into two types. The first type are complex poles with imaginary components which are conjectured to be of greater magnitude than the 'true system poles'; the sec-

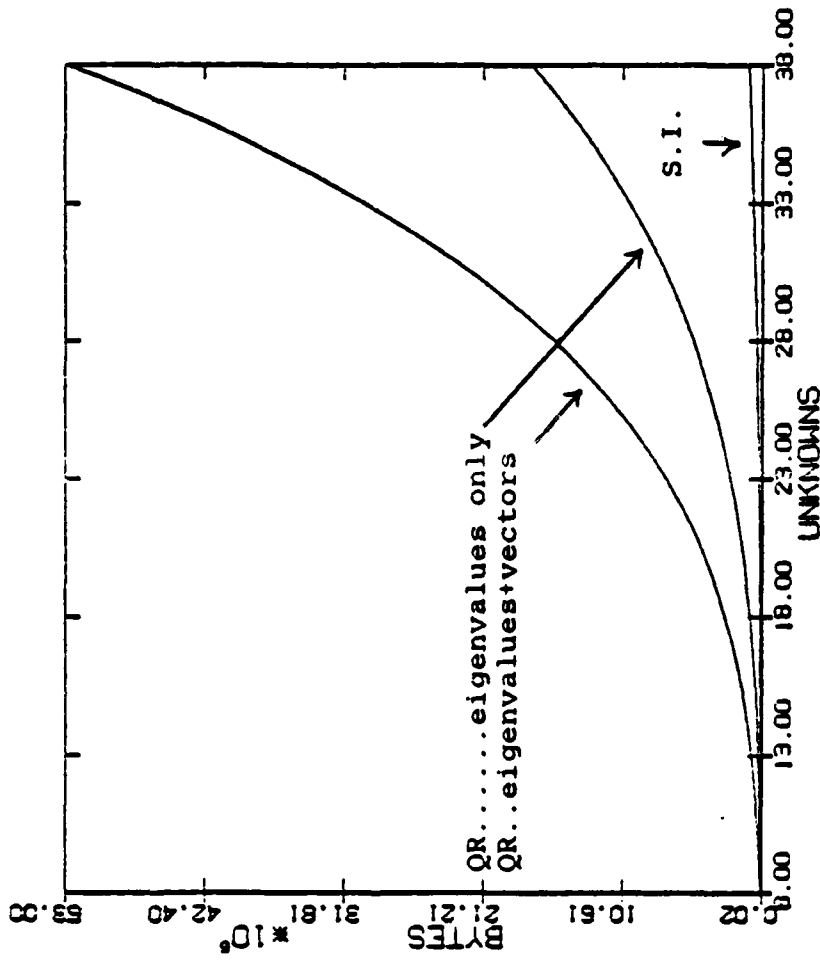


Figure 5.10: Storage requirements for various eigensolution methods.

ond type are purely real poles which are conjectured to extend further down the real axis than the true poles. Both of these conjectures and an elimination technique for the 'spurious' poles are discussed in the following paragraphs.

The angle associated with the polar representation of eigenvalues which possess positive real and imaginary components is at most $\pi/2$ radians (by symmetry, we may similarly consider the conjugate of these eigenvalues). The imaginary component of the poles corresponding to these eigenvalues, then, have a magnitude which is at most $1/(2c\Delta t)$ radians (recalling that the poles are scaled by $1/(\pi c)$). When the stability condition $c\Delta t = \Delta$ is valid, this maximum becomes $1/(2\Delta)$ radians. Since all thin-wire pole distributions obtained by frequency-domain techniques are bounded by $1/(2\Delta)$ radians, it is sensible to bound time-domain methods by that value as well. Hence, we conjecture that the true system poles obtained by TD-SEM are bounded on the imaginary axis by $1/(2\Delta)$ for arbitrary choice of $c\Delta t$ (note that this restriction eliminates the poles corresponding to eigenvalues with negative real components). This technique generates a simple criterion from which spurious poles off the real axis may be eliminated. We consider, next, the spurious poles which are situated on the real axis.

The second type of additional poles are not as simple to remove. No well defined method has been developed. These poles do not disturb the well defined layering structure since they appear past it. TD-SEM generates true poles past the layering structure (Figure 5.6) however, and therefore an ambiguity exists. One possible restriction would be to retain only those poles within the range 0 to approximately $-1/(2\Delta)$ on the real axis. Although this criterion is admittedly strict, it may be effectively used for arbitrary choices of $c\Delta t$.

To conclude this section, it should be noted that the left half plane pole structure obtained from an unstable algorithm has very little similarity with the pole structure obtained from a stable algorithm. Hence, one should be certain that a particular scheme is stable if the results obtained are to be considered meaningful and accurate.

5.3.3 Pole Shift by Kernel Decoupling

It was suspected a priori that a relation may exist between the sub-matrices of the transition matrix and the particular layering structure of the poles. In other words, the first few sub-matrices may contribute the poles of the first layer, the next few the poles of the second layer, and so on. To test this conjecture, the effect of zeroing the

kernel $G_{|n-n'|}$ of equation (5-16) for various values of the difference $|n-n'|$ was considered. This effectively removes element to element coupling and thereby zeros sub-matrices. Figure 5.11 depicts the movement of the pole distribution for a 1 meter antenna with a radius of 0.005 meters discretized with 10 unknowns ($N=10$). All layers tend to shift toward the imaginary axis (approaching a transmission line) as elements are zeroed from the extreme outer sub-matrices inward. Unfortunately, no relation between the block sub-matrices and particular layers can be inferred from this form of movement. Specifically, the results shown in Figure 5.11 may be interpreted as follows: full set denotes no decoupling, the level 1 set has the kernel evaluated at $|n-n'|=N+1$ set equal to zero, the level 2 set has the evaluation at $|n-n'|=N+1$ and N equal to zero, the level 3 set has the evaluation at $|n-n'|=N+1$, N , and $N-1$ equal to zero, and the level 7 set is similarly defined.

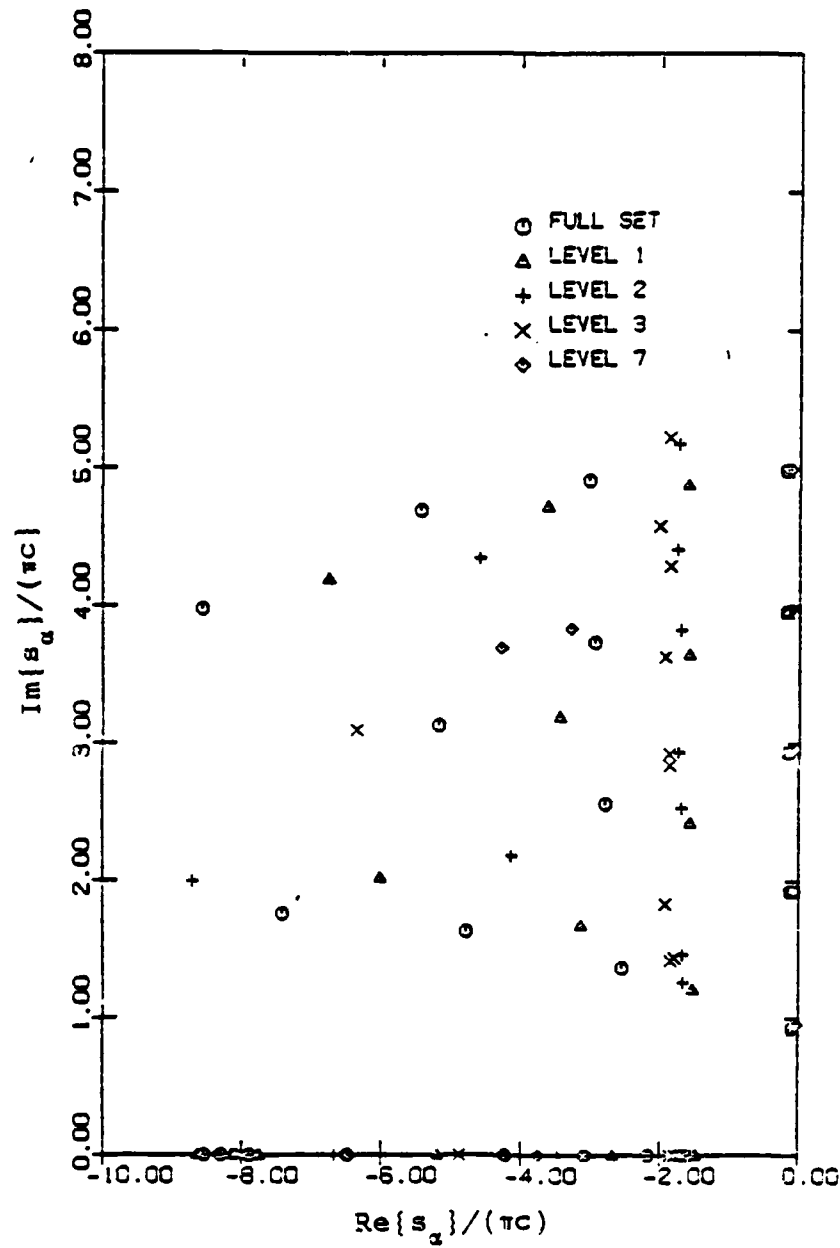


Figure 5.11: Pole movement due to kernel decoupling. The scatterer was 1 meter in length with a radius of 0.005 meters. The number of unknowns was 10.

Chapter VI

TRANSIENT ANALYSIS OF THIN, PERFECT CONDUCTING RECTANGULAR PLATES

6.1 INTRODUCTION

The rectangular plate falls within the class of structures known as open structures with edges. Structures with edges, and in particular corners, are difficult to analyze due to the singular behavior of the current component parallel to an edge, and the ambiguity of the current magnitude in a corner. These complications have generally restricted exact analytic solutions to infinite half-plane problems. In particular, we cite an exact, frequency-domain solution for the current density generated on an infinite half-plane by an edge on incident plane wave which may be found in Born and Wolf [41]; the transformed, time-domain result, may subsequently be found in Davis, et al [42].

Since the realm of problems which are solvable by analytic methods is quite narrow, interest has turned toward the numerical analysis of finite open structures. The advent of the method of moments [14] stimulated the frequency-domain study of these structures; while recent interest in transient methods was primarily stimulated by a study due to Bennett, et al [43]. In Bennett's study, both transient

numerical and experimental results for several canonic open structures were presented. Some of the techniques developed in this chapter are based on the latter contribution.

The study of the SEM parameters for open structures has been limited to rectangular geometries. A treatise on obtaining these parameters for rectangular apertures and structures using frequency-domain techniques has been presented by Pearson [44].

In this chapter, the transient numerical solution of the thin, perfect conducting rectangular plate problem is studied. In Section 6.2, the basic mathematical formulation of the problem using finite difference techniques is presented. The basic difference formulation is then applied to a 'standard' gridding scheme in Section 6.3, and a 'shifted' gridding scheme in Section 6.4. The shifted, or offset, scheme was initially introduced for the solution of rectangular problems in the frequency-domain by Glisson and Wilton [45]. Stability analysis and current distributions for each of these schemes are presented in the appropriate sections. In Section 6.5, the TD-SEM pole distribution for the square plate is introduced.

6.2 MATHEMATICAL FORMALISM

The electric field integral expression (2-12a) is the appropriate expression for describing thin, perfect conducting structures. For the geometry shown in Figure 6.1, this expression may be written, in vector potential notation, as the following coupled set:

$$\begin{aligned}\epsilon_0 \frac{\partial}{\partial t} E_x^{inc} &= \frac{1}{c^2} \frac{\partial^2}{\partial t^2} A^x - \left(\frac{\partial^2}{\partial x^2} A^x + \frac{\partial^2}{\partial x \partial y} A^y \right) \\ \epsilon_0 \frac{\partial}{\partial t} E_y^{inc} &= \frac{1}{c^2} \frac{\partial^2}{\partial t^2} A^y - \left(\frac{\partial^2}{\partial y^2} A^y + \frac{\partial^2}{\partial y \partial x} A^x \right)\end{aligned}\tag{6-1}$$

where $\bar{A} = (A^x, A^y, 0)$, and $\bar{E}^{inc} = (E_x^{inc}, E_y^{inc}, E_z^{inc})$.

The following representation of \bar{E}^{inc} will be used for all results presented in this chapter:

$$\bar{E}^{inc}(\bar{r}; t) = \hat{\theta} E_0 \exp(-g^2((t-t_{max}) + \hat{k} \cdot \bar{r}/c)^2)\tag{6-2}$$

where

$$\hat{\theta} = \hat{x} \cos\theta \cos\phi + \hat{y} \cos\theta \sin\phi - \hat{z} \sin\theta,\tag{6-2a}$$

$$\hat{k} = \hat{x} \sin\theta \cos\phi + \hat{y} \sin\theta \sin\phi + \hat{z} \cos\theta,\tag{6-2b}$$

$$\bar{r} = x\hat{x} + y\hat{y} + z\hat{z}.\tag{6-2c}$$

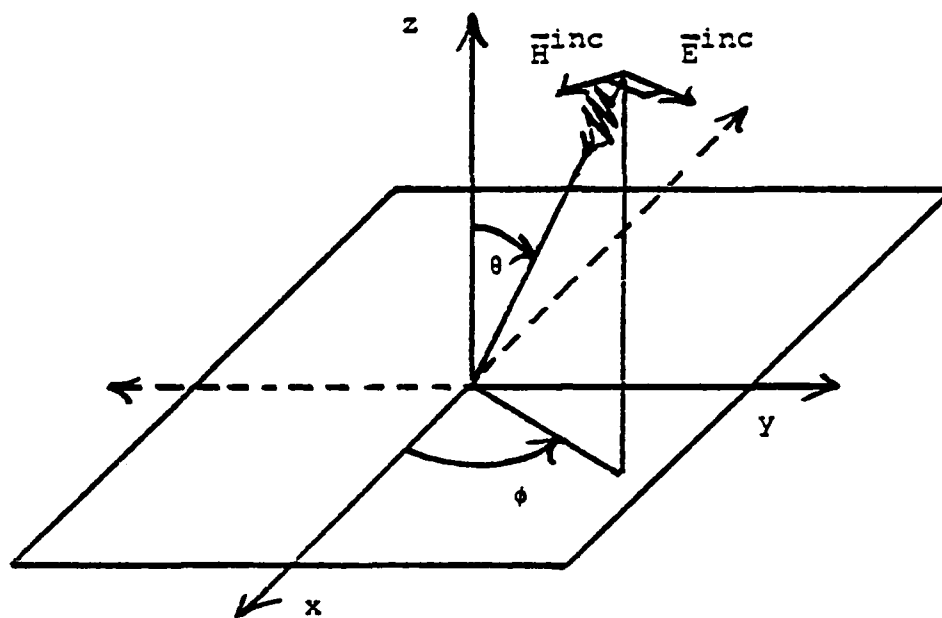


Figure 6.1: Plate geometry.

The value of E_0 was chosen to be the free space impedance, 120π , t_{\max} was chosen to be 2.45 light meters (LM), and g was chosen so that the magnitude of \bar{E}^{inc} at $t=0$ and $t=4.9$ LM would be 0.0001 volts/meter.

From expansion (3-17), the x and y components of the vector potential may be explicitly represented as

$$A_{m,n,p}^{x,y} = \sum_{m'=1}^M \sum_{n'=1}^N \sum_{p'=-\infty}^{\infty} \bar{J}_{m',n',p'}^{x,y} G_{|m-m'|, |n-n'|, (p-p')} \quad (6-3)$$

where

$$G_{\alpha,\beta,\delta} = \int_{(\alpha-\frac{1}{2})\Delta}^{(\alpha+\frac{1}{2})\Delta} \int_{(\beta-\frac{1}{2})\Delta}^{(\beta+\frac{1}{2})\Delta} \frac{p_{\Delta t} (\delta - (u^2 + v^2)^{1/2}/c)}{4\pi (u^2 + v^2)^{1/2}} dudv \quad (6-3a)$$

and $A_{m,n,p}^{x,y} = A^{x,y}(m\Delta, n\Delta; p\Delta t)$.

Unfortunately, the integral which appears may not be evaluated exactly due to the presence of the time pulse. Numerical integration or linear interpolation represent the possible methods of evaluation. In Figure 6.2, the physical interpretation of how the time pulse activates various annular regions which contribute to the integral is shown (causality allows us to only consider zero or positive values of the time difference $p-p'$). From this figure, the following linear interpolation formula may be derived:

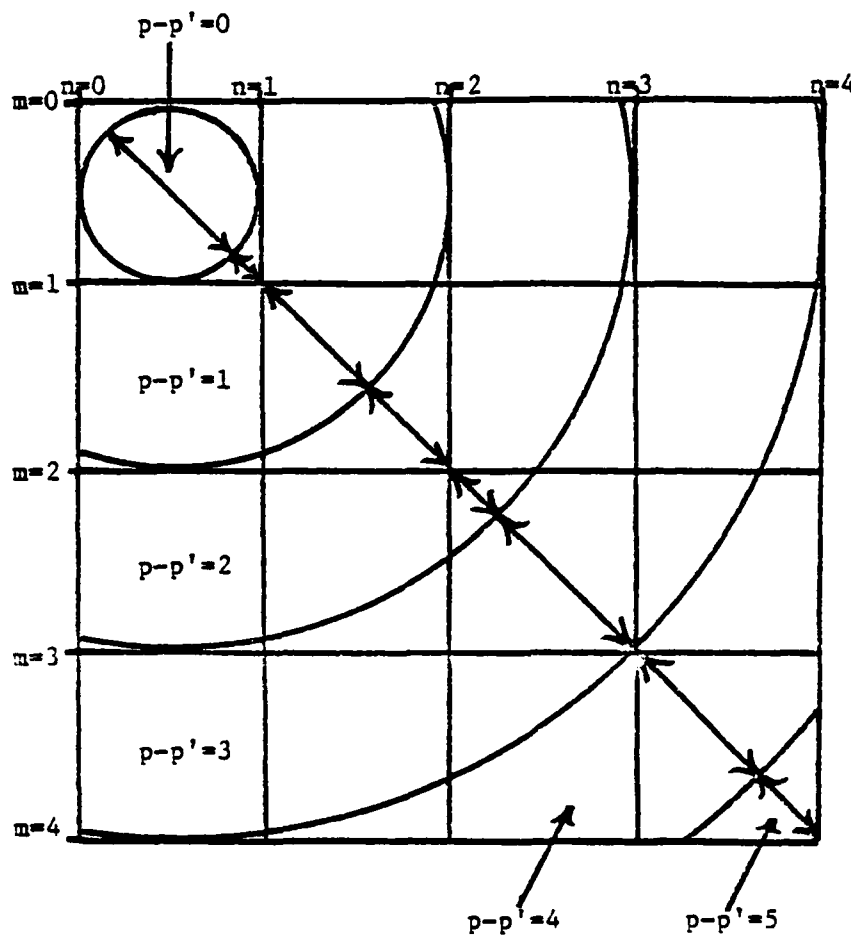


Figure 6.2: Annular propagation of active regions due to the time difference ($p-p'$).

$$G_{\alpha,\beta,\delta} = [P_{\Delta}[(\delta - \text{Int}(D))\Delta t] + (P_{\Delta}[(\delta - 1 - \text{Int}(D))\Delta t] \\ - P_{\Delta}[(\delta - \text{Int}(D))\Delta t])(D - \text{Int}(D))] G'_{\alpha,\beta}, \quad (6-4)$$

where

$$D = (\alpha^2 + \beta^2)^{1/2} / (c\Delta t), \quad (6-4a)$$

$\text{Int}(D)$ denotes 'integer part of', and

$$G'_{\alpha,\beta} = \int_{(\alpha-1/2)\Delta}^{(\alpha+1/2)\Delta} \int_{(\beta-1/2)\Delta}^{(\beta+1/2)\Delta} \frac{dudv}{4\pi(u^2+v^2)^{1/2}}. \quad (6-5)$$

By letting $a=(\alpha+1/2)$, $b=(\alpha-1/2)$, $c=(\beta+1/2)$, and $d=(\beta-1/2)$, we may evaluate this integral as

$$G'_{\alpha,\beta} = \frac{1}{4\pi} [\alpha \Delta \ln \left(\frac{c+(c^2+a^2)^{1/2}}{d+(d^2+a^2)^{1/2}} \right) \left(\frac{d+(d^2+b^2)^{1/2}}{c+(c^2+b^2)^{1/2}} \right)] \\ + \frac{\Delta}{2} \ln \left[\left(\frac{a+(c^2+a^2)^{1/2}}{b+(c^2+b^2)^{1/2}} \right) \left(\frac{a+(d^2+a^2)^{1/2}}{b+(d^2+b^2)^{1/2}} \right) \left(\frac{c+(c^2+a^2)^{1/2}}{d+(d^2+a^2)^{1/2}} \right) \left(\frac{c+(c^2+b^2)^{1/2}}{d+(d^2+b^2)^{1/2}} \right) \right] \\ + \beta \Delta \ln \left[\left(\frac{a+(c^2+a^2)^{1/2}}{a+(d^2+a^2)^{1/2}} \right) \left(\frac{b+(d^2+b^2)^{1/2}}{b+(c^2+b^2)^{1/2}} \right) \right]. \quad (6-5a)$$

Over the self patch region ($m=m'$, $n=n'$) the anti-derivative reduces to

$$G'_{\alpha,\beta} = \frac{\Delta}{\pi} \ln (1 + \sqrt{2}). \quad (6-5b)$$

A simple rectangular rule approximation may alternatively be used to evaluate integral (6-5) over all patches other than the self patch without introducing considerable error, i.e.,

$$G'_{\alpha,\beta} \approx \begin{cases} \frac{\Delta^2}{4\pi(\alpha^2+\beta^2)^{1/2}} & \alpha,\beta \neq 0 \\ \frac{\Delta}{\pi} \ln(1+\sqrt{2}) & \alpha=\beta=0 \end{cases} \quad (6-6)$$

Use of linear interpolation and approximation (6-6) is the recommended means for the evaluation of equation (6-3a). Numerical integration or use of equation (6-5a) have been found to introduce only slight amplitude shifts in the final results, and therefore their use is unjustified unless precise results are sought. The interpretation of precise is ambiguous, however, due to the vast number of models which may be applied to a particular problem, and hence the vast number of slightly different results which may be obtained.

6.3 STANDARD GRIDGING SCHEME

Figure 6.3 depicts a standard gridding scheme for a rectangular plate. The patches as shown are square due to the choice of a uniform sampling distance in both the x and y directions; this is typically, but not necessarily, done. Two complications are associated with this simple, commonly used, model. First, since the two current density components lie directly on top of one another, a smooth transition between components is not possible; and second, boundary conditions on the current density must be explicitly enforced.

For the standard grid, the following explicit finite difference scheme for the x component of the vector potential is appropriate:

$$\begin{aligned}
 A_{m,n,p+1}^x &= r^2 (A_{m+1,n,p}^x + A_{m-1,n,p}^x - 2A_{m,n,p}^x) \\
 &+ \frac{r^2}{4} (A_{m+1,n+1,p}^y + A_{m-1,n-1,p}^y - A_{m+1,n+1,p}^y - A_{m-1,n+1,p}^y) \\
 &+ A_{m,n,p-1}^x - 2A_{m,n,p}^x + (r^2 \epsilon_0) \frac{\partial}{\partial t} E_x^{\text{inc}} \begin{pmatrix} m=0,1,\dots,M \\ n=0,1,\dots,N \\ p=1,2,\dots \end{pmatrix}
 \end{aligned}
 \tag{6-7}$$

where $r^2 = (c\Delta t/\Delta)^2$. A^y may be similarly defined. An explicit difference scheme for the current density is obtained by substituting expansion (6-3) into the above difference equation and manipulating the indices of the summations.

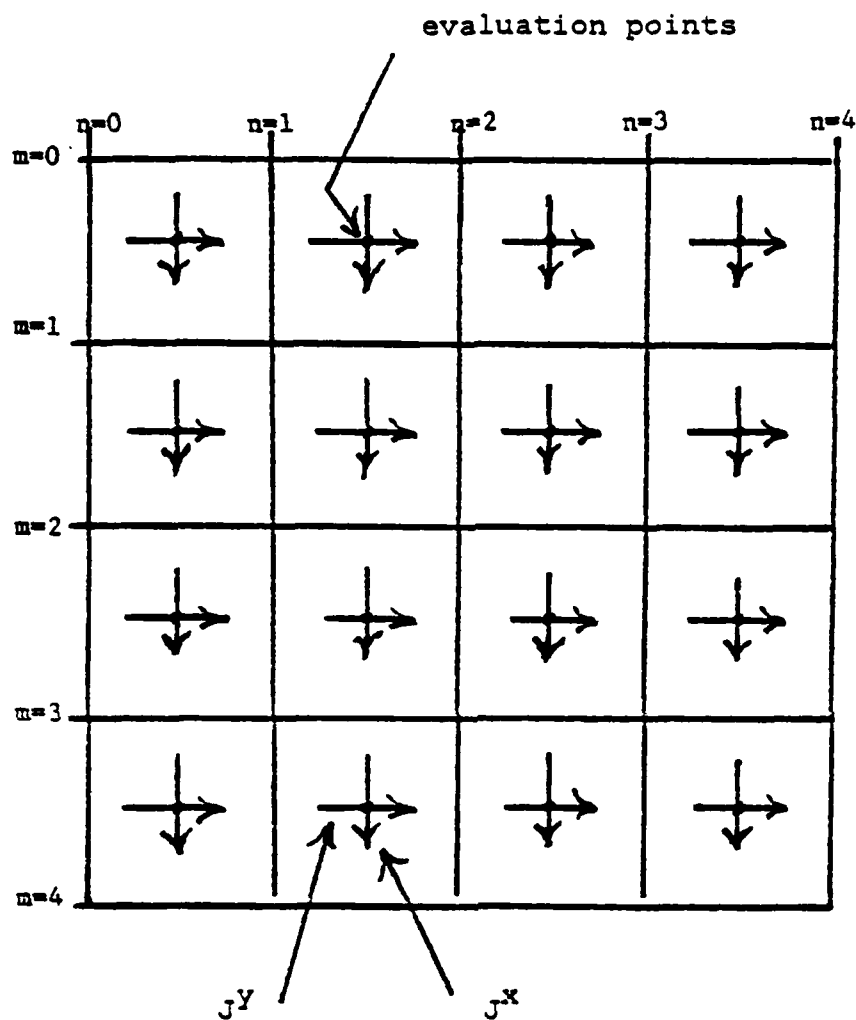


Figure 6.3: Standard gridding scheme.

An approximate stability criterion for the vector potential scheme may be obtained by the Fourier stability method (Sections 3.3.1, 5.3). Let

$$\begin{bmatrix} A^x \\ A^y \end{bmatrix} = \begin{bmatrix} a_x \\ a_y \end{bmatrix} \omega^p \exp \left\{ j(\alpha m \Delta + \beta n \Delta) \right\} \quad (6-8)$$

where a_x , a_y are arbitrary coefficients, $\omega = \exp\{s\Delta t\}$ (s is arbitrary and generally complex), and α , β are arbitrary real constants. By substituting the expression for A^x into equation (6-7) and the expression for A^y into a similar equation, we obtain

$$\begin{bmatrix} a_x \\ a_y \end{bmatrix} \omega^2 = \omega \begin{bmatrix} 2-4r^2 \sin^2(\alpha \Delta/2) & r^2 \sin(\alpha \Delta) \sin(\beta \Delta) \\ r^2 \sin(\alpha \Delta) \sin(\beta \Delta) & 2-4r^2 \sin^2(\beta \Delta/2) \end{bmatrix} \begin{bmatrix} a_x \\ a_y \end{bmatrix} + \begin{bmatrix} -1 & 0 \\ 0 & -1 \end{bmatrix} \begin{bmatrix} a_x \\ a_y \end{bmatrix}. \quad (6-9)$$

This matrix equation may be reduced to the following quartic equation in ω :

$$\omega^4 + (E+C)\omega^3 + (EC-BD+2)\omega^2 + (E+C)\omega + 1 = 0 \quad (6-10)$$

where

$$E = 4r^2 \sin^2(\alpha \Delta/2) - 2 \quad (6-10a)$$

$$B = r^2 \sin(\alpha \Delta) \sin(\beta \Delta) \quad (6-10b)$$

$$C = 4r^2 \sin^2(\beta\Delta/2) \quad (6-10c)$$

$$D = r^2 \sin(\beta\Delta) \sin(\alpha\Delta) . \quad (6-10d)$$

For any choice of real α , β , $|\omega| \leq 1$ for $r \leq 1$. Therefore, the choice $c\Delta t = \Delta$ may lead to a stable solution. Certainty cannot be obtained since boundary conditions cannot be included in the analysis. The matrix stability method must be used to verify this criterion for the current density coefficient difference formulation with arbitrary boundary conditions.

The enforcement of boundary conditions is an integral part of using the standard gridding scheme effectively. Figure 6.4 shows the current density component corresponding to the direction of polarization of the incident wave on the center patch of a one meter square plate discretized with four unknowns in each direction when no boundary conditions are enforced and choosing $c\Delta t = 0.7\Delta$. The result is highly oscillatory yet stable. Figure 6.5 depicts the effect of enforcing components of the current perpendicular to the edges to be zero. In Figure 6.6 an attempt has been made to enforce the form of the singular behavior of the current

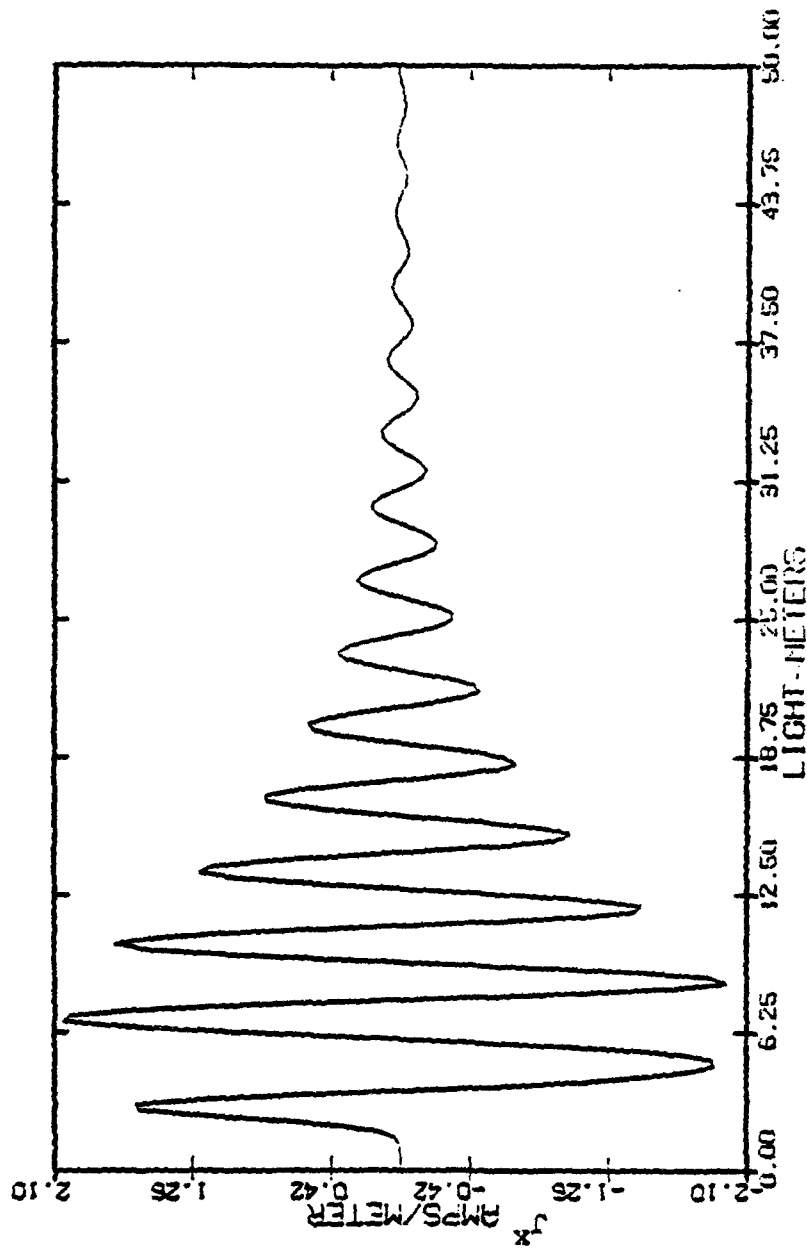


Figure 6.4: Current density component corresponding to the direction of incident polarization calculated on the center patch of a 1 meter square plate. No boundary conditions have been enforced. A standard gridding scheme has been used with 16 patches for each current component. The pulse width was 4.9 light meters, and the choice $\text{cat}=0.7\Delta$ was made.

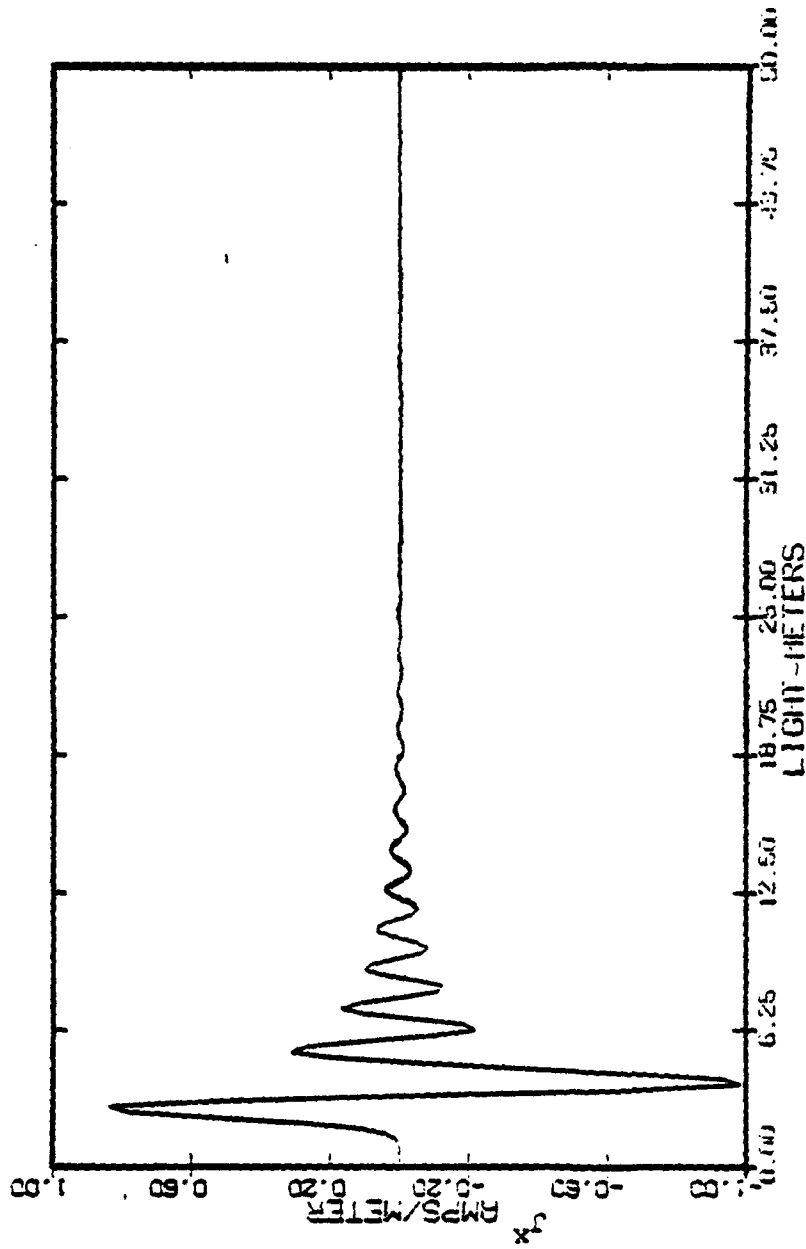


Figure 6.5: Current density component corresponding to the direction of incident polarization calculated on the center patch of a 1 meter square plate. The normal component of the current density has been set to zero at the edges. A standard gridding scheme has been used with 16 patches for each current component. The width of the incident pulse was 4.9 light meters, and the choice $\text{cat}=0.7\Delta$ was made.

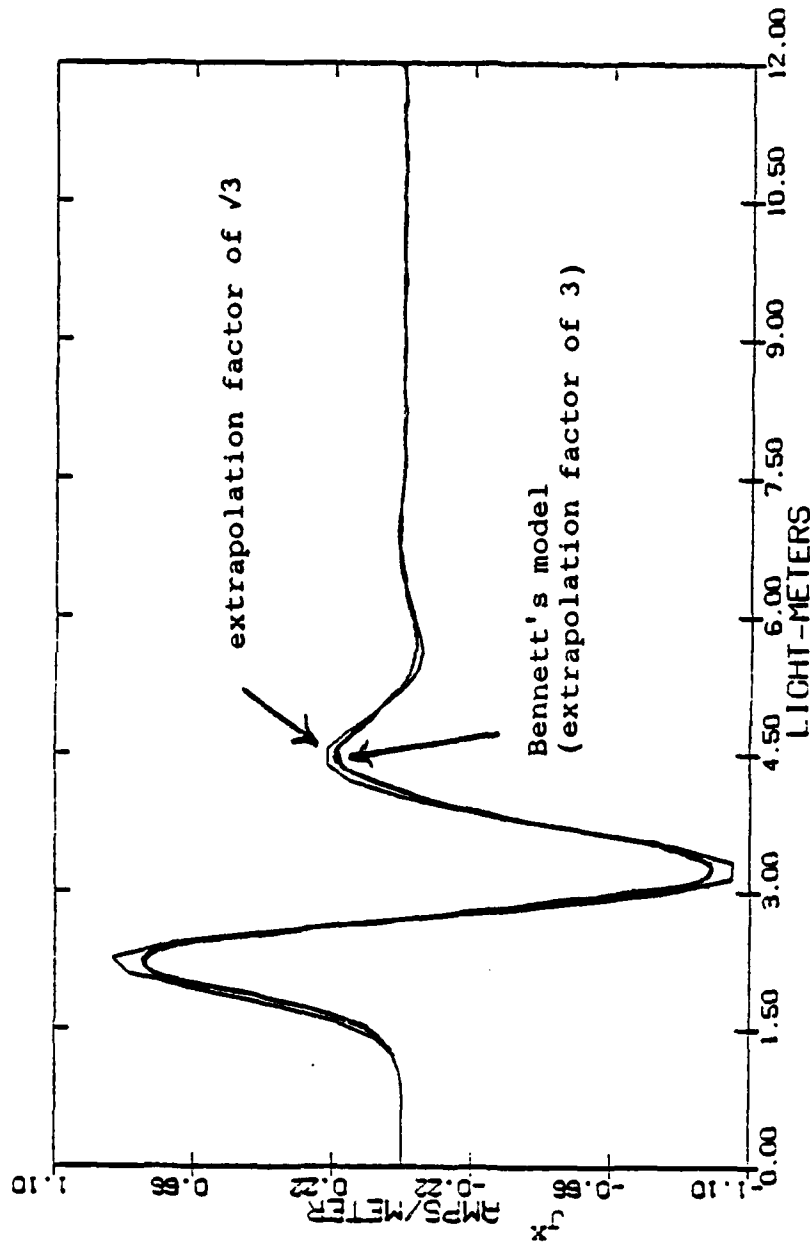


Figure 6.6: Current density component corresponding to the direction of incident polarization calculated on the center patch of a 1 meter square plate. Normal components of the current density have been set to zero at the edges; A standard gridding scheme has been extrapolated at the edges. A comparison has been made with 16 patches for each current component. A comparison has been made with Bennett's model. The incident pulse was 4.9 light meters wide, and the choice $c\Delta t = 0.7\Delta$ was made.

components parallel to an edge. This was accomplished by assuming a reciprocal square root of distance singularity as the edge is approached [42]. Hence, the value $\sqrt{3}$ was chosen as the extrapolation constant for the parallel current components $3\Delta/2$ from the edge, i.e., the parallel component at position $\Delta/2$ from the edge is $\sqrt{3}$ times the parallel current component evaluated at $3\Delta/2$ from the edge.

In Figure 6.6 a comparison has been made with a current density distribution obtained from the theoretical model used by Bennett [43]. Bennett's model and the model used here differ only in the extrapolation constant used for the current density component parallel to an edge. In the model used by Bennett, an extrapolation constant of 3 was used instead of $\sqrt{3}$. The factor of 3 was found to occasionally yield unstable results, whereas $\sqrt{3}$ was found to always yield stable results. Hence, the latter was preferred. The two curves agree quite closely within the twelve light meter frame which is shown. It should be noted that Bennett's model has been shown [43] to yield results quite similar to experimental measurements.

The use of either 3 or $\sqrt{3}$ as an extrapolation technique is somewhat unsatisfying since it does not permit a time fluctuation of the particular form which is being forced. The half plane problem which can be solved analytically

yields a reciprocal square root behavior for the current density which includes both a spatial and a time dependence under the root [42]. We would anticipate a similar dependence for the plate, and hence any extrapolation should reflect this. Further study is required.

Although theoretical results similar to experimental measurements may be obtained from a standard gridding scheme, it is difficult to know a priori when satisfactory results have been obtained due to the modifications which are required. In an effort to avoid these modifications (i.e., create a more natural model), we consider an offset or shifted gridding scheme.

6.4 SHIFTED GRIDDING SCHEME

Figure 6.7 depicts a shifted gridding scheme. Three desirable properties about this formulation are as follows: current is allowed to make a smooth transition between components, zero boundary conditions on the current are implicitly enforced, and it is not necessary to step off the structure for any finite difference evaluations.

The explicit difference representation of the x component of the vector potential is given by

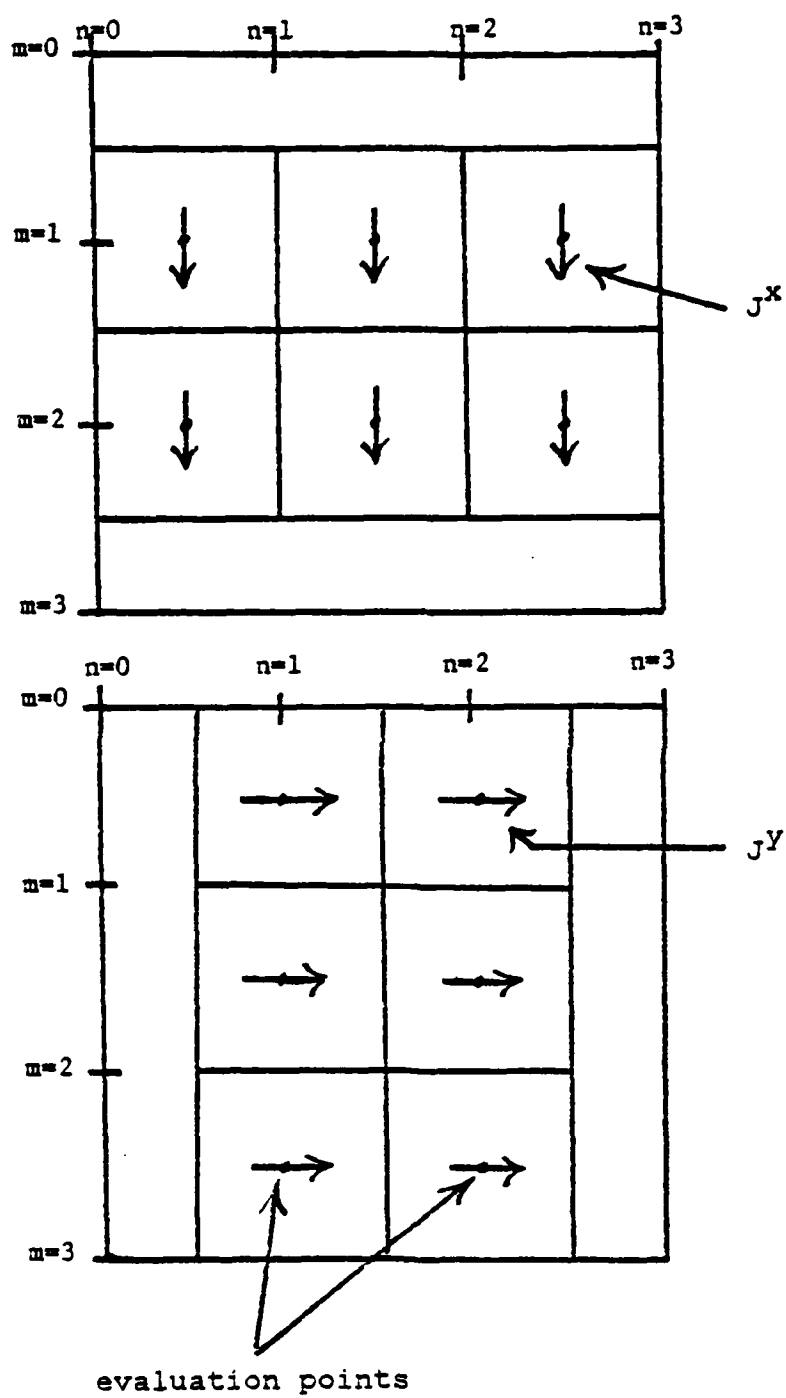


Figure 6.7: Shifted gridded scheme.

$$\begin{aligned}
A_{m,n-\frac{1}{2},p+1}^x &= r^2 (A_{m+1,n-\frac{1}{2},p}^x + A_{m-1,n-\frac{1}{2},p}^x - 2A_{m,n-\frac{1}{2},p}^x) \\
&+ r^2 (A_{m+\frac{1}{2},n,p}^y + A_{m-\frac{1}{2},n-1,p}^y - A_{m+\frac{1}{2},n-1,p}^y - A_{m-\frac{1}{2},n,p}^y) \\
&+ A_{m,n-\frac{1}{2},p-1}^x - 2A_{m,n-\frac{1}{2},p}^x + (r^2 \epsilon_0) \frac{\partial}{\partial t} E_x^{\text{inc}} \begin{pmatrix} m=0,1,\dots,M \\ n=0,1,\dots,N+1 \\ p=1,2,\dots \end{pmatrix}.
\end{aligned}
\tag{6-11}$$

A similar equation may be developed for A^y . An explicit scheme for the current density coefficients may be obtained by substituting equation (6-3) into the above equation and manipulating the indices of the summations.

A preliminary stability criterion for the vector potential scheme may be found by the Fourier stability method. By letting

$$\begin{bmatrix} A^x \\ A^y \end{bmatrix} = \begin{bmatrix} a_x \omega^p \exp \{j(\alpha m \Delta + \beta(n-\frac{1}{2})\Delta)\} \\ a_y \omega^p \exp \{j(\alpha(m-\frac{1}{2})\Delta + \beta n \Delta)\} \end{bmatrix}
\tag{6-12}$$

and substituting into the difference scheme (6-11), we obtain the following quartic equation in ω (similar to the unshifted development):

$$\omega^4 + (E+C)\omega^3 + (EC-BD+2)\omega^2 + (E+C)\omega + 1 = 0 \quad (6-13)$$

where

$$\begin{aligned} E &= 4r^2 \sin^2(\alpha\Delta/2) - 2 \\ B &= r^2(1 + e^{-j\alpha\Delta} e^{j\beta\Delta} - e^{-j\alpha\Delta} - e^{j\beta\Delta}) \\ C &= 4r^2 \sin^2(\beta\Delta/2) - 2 \\ D &= r^2(1 + e^{-j\beta\Delta} e^{j\alpha\Delta} - e^{-j\beta\Delta} - e^{j\alpha\Delta}). \end{aligned} \quad (6-13a)$$

For any choice of real α , β , $|\omega| \leq 1$ for $r^2 \leq (1/2)$ or $c\Delta t \leq (\sqrt{2}/2)\Delta$. This result may be established analytically by assuming four solutions of the form $\exp\{\pm j\theta_1\}$, $\exp\{\pm j\theta_2\}$ and noting that the product of all the roots must be unity, or it may be established numerically.

The basic result may be extended to accommodate three-dimensional problems with different spatial sampling distances in each of the three spatial directions, i.e., we have Δx , Δy , Δz instead of simply Δ . The stability requirement for shifted schemes, in general, is then

$$\frac{1}{(c\Delta t)^2} \geq \frac{1}{(\Delta x)^2} + \frac{1}{(\Delta y)^2} + \frac{1}{(\Delta z)^2} \quad (6-14)$$

The validity of these expressions for the analogous current density difference formulation must be confirmed by the matrix stability method.

Figure 6.8 shows the unstable result obtained by choosing $c\Delta t = \Delta$. By choosing $c\Delta t \leq (\sqrt{2}/2)\Delta$, however, we obtain the stable curves shown in Figure 6.9. A comparison of these curves with the curve generated by the standard gridding scheme has been made. Note that the amplitude of the curves obtained from the two schemes differ slightly. This is primarily due to the different techniques used to enforce the zero boundary condition in each scheme.

6.5 TD-SEM POLE DISTRIBUTION

In this section, we present pole distributions obtained by TD-SEM (Section 3.3.1) using the shifted gridding scheme on a one meter square plate. Figure 6.10 shows the distribution for a total of 2 unknowns ($\Delta=1/2$) for each current component, Figure 6.11 shows the distribution for a total of 6 unknowns ($\Delta=1/3$), and Figure 6.12 shows the distribution for a total of 12 unknowns ($\Delta=1/4$). The choice $c\Delta t = 0.7\Delta$ was made throughout.

As was discussed in Section 5.3.2.1, an ambiguity exists in the validity of all the 'poles' TD-SEM yields when $c\Delta t$ is chosen less than Δ due to an increase in the order of the transition matrix. A filtering scheme to remove poles which were conjectured to be a consequence of the numerical procedure was discussed in that section. For Figures 6.10-12

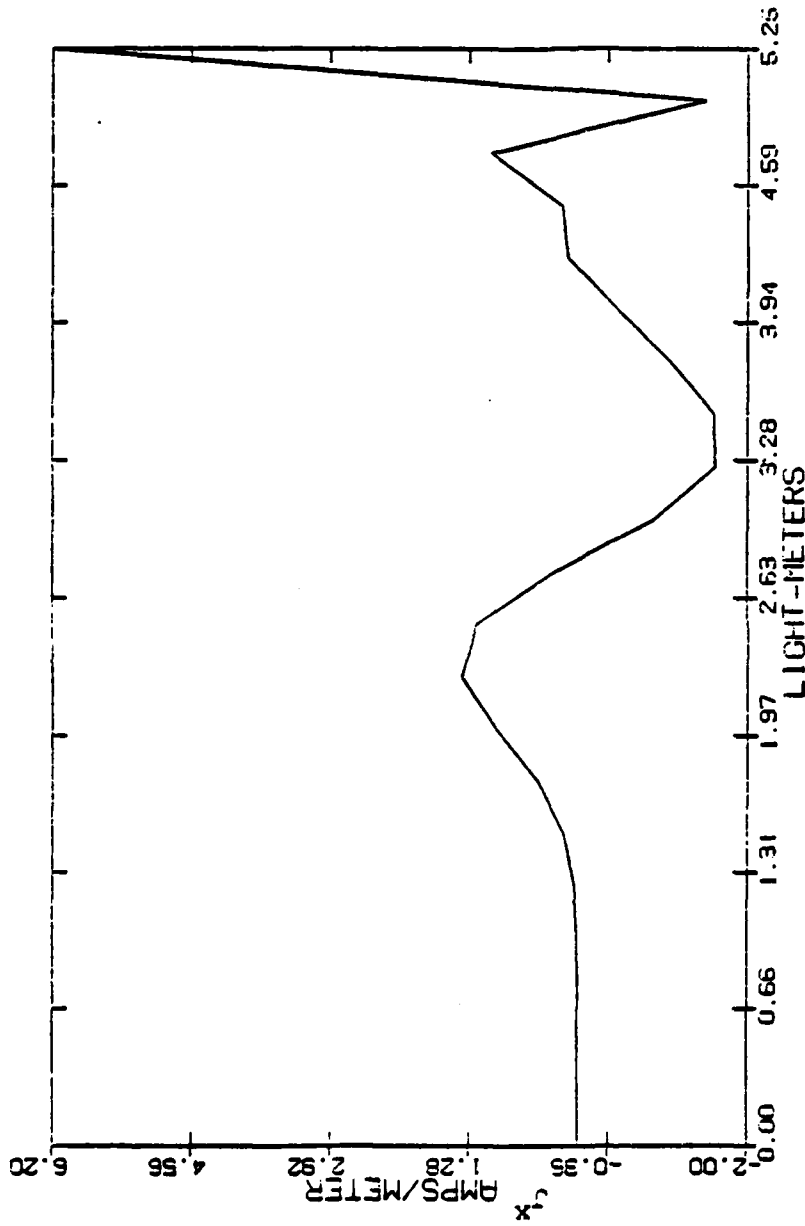


Figure 6.8: Unstable current density distribution obtained from the shifted gridding scheme for $cat=A$. The component corresponding to the direction of incident polarization on the center patch is shown. A total of 12 patches have been used for each current density component.

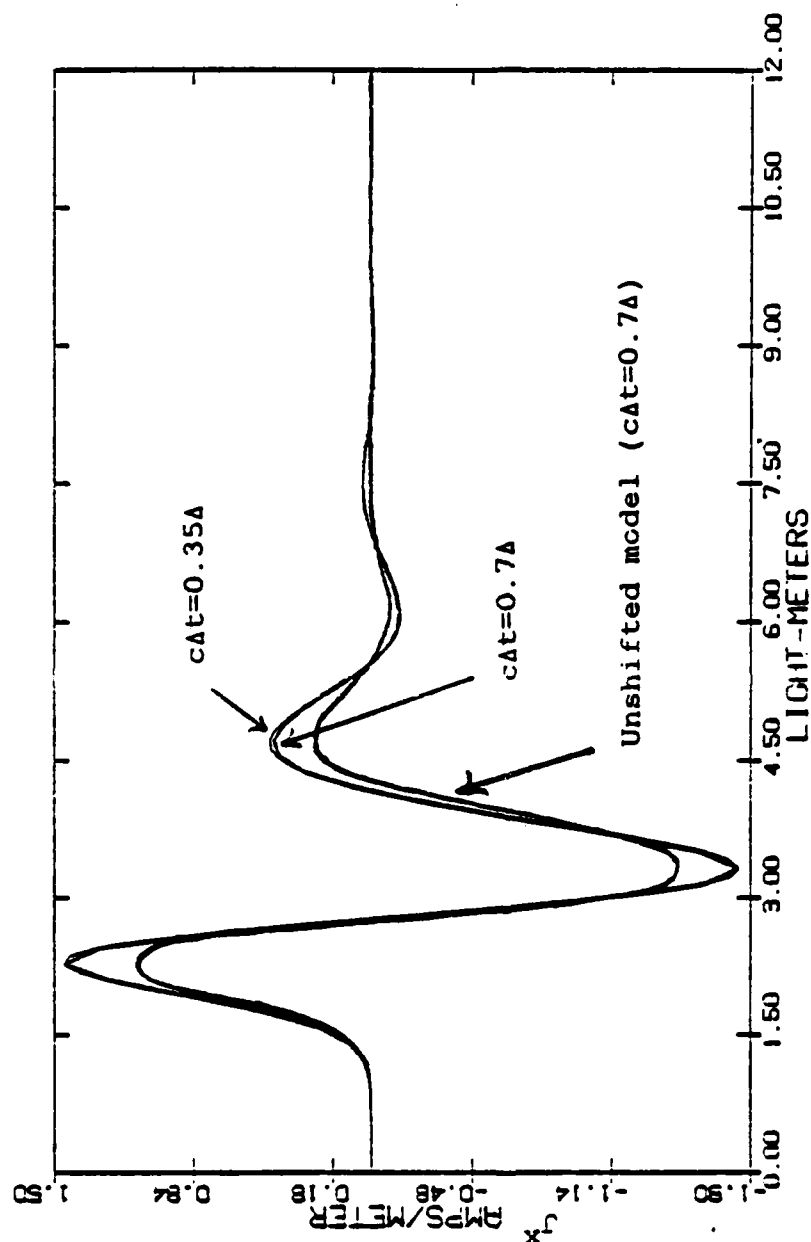


Figure 6.9: Current density component corresponding to the direction of incident polarization calculated on the center patch of a 1 meter square plate. A shifted gridding scheme has been used with 12 patches for each current component. The incident pulse was 4.9 light meters wide, and a comparison with the standard grid model has been made.

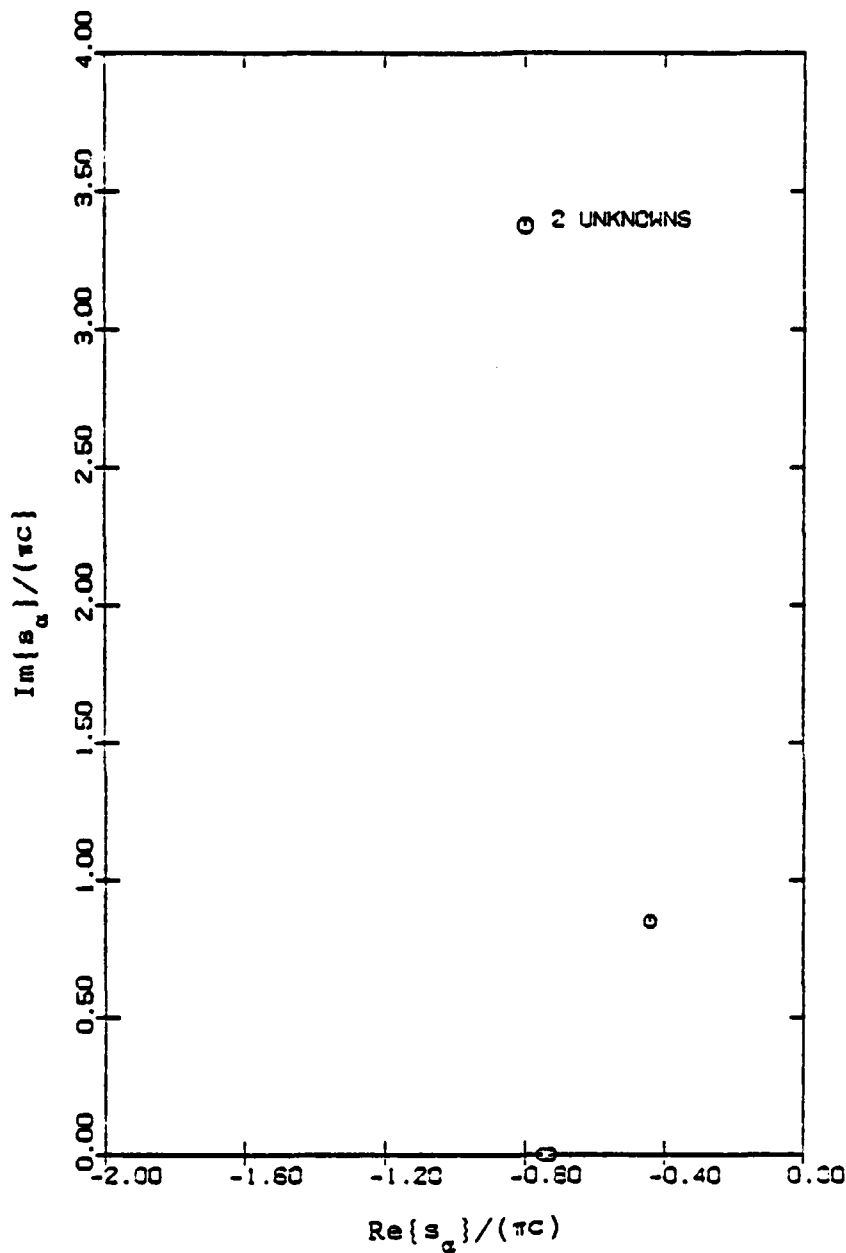


Figure 6.10: Poles for a 1 meter square plate discretized with a shifted gridding scheme. The total number of patches for each component of the current density was 2, and the choice $c\Delta t=0.7\Delta$ was made.

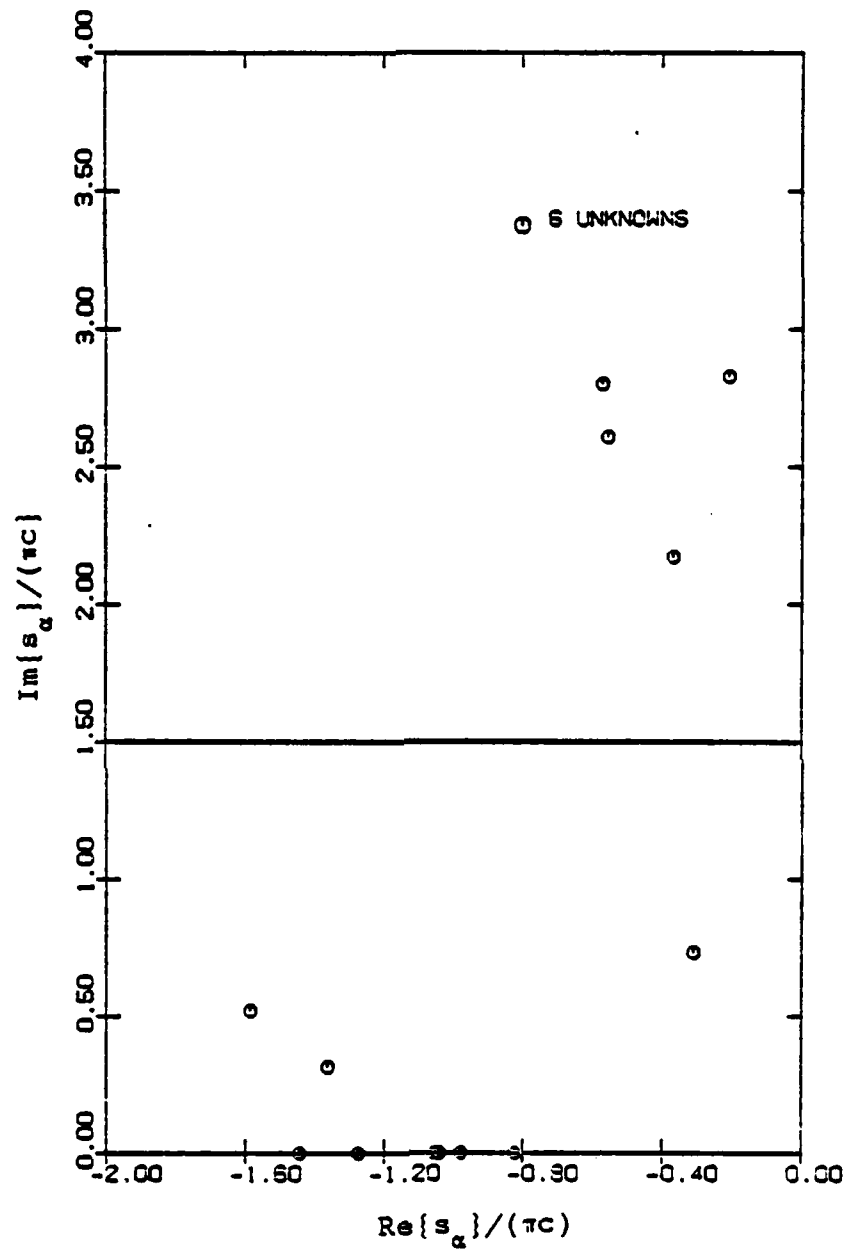


Figure 6.11: Poles for a 1 meter square plate discretized with a shifted gridding scheme. The total number of patches for each component of the current density was 6, and the choice $c\Delta t=0.7\Delta$ was made.

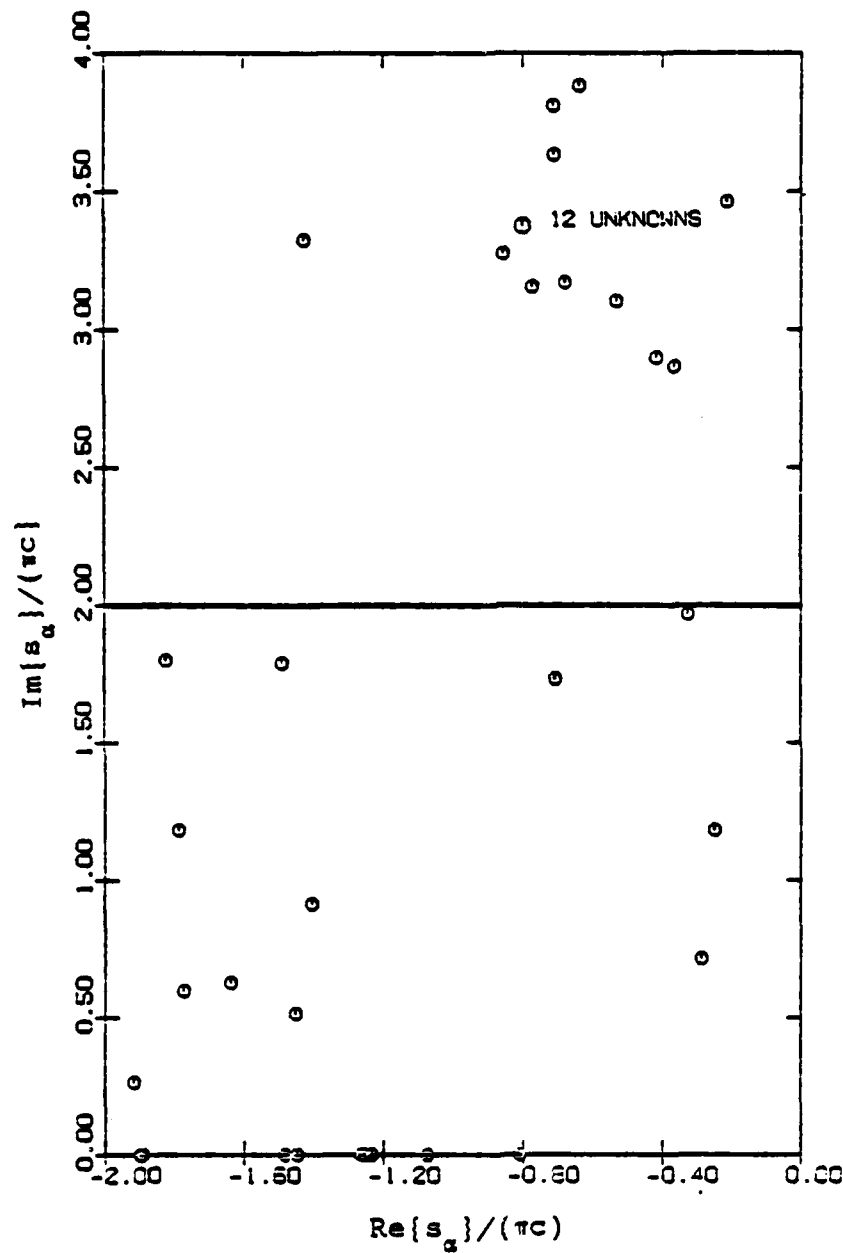


Figure 6.12: Poles for a 1 meter square plate discretized with a shifted gridding scheme. The total number of patches for each component of the current density was 12, and the choice $c\Delta t=0.7\Delta$ was made.

a similar, but slightly different, filtering scheme was used. The scaled poles corresponding to the eigenvalues with positive real components were restricted to a maximum magnitude on the imaginary axis of $1/(2\Delta)$ radians; the scaled poles corresponding to the eigenvalues with negative real components were restricted to the range $1/(2\Delta)$ to $1/\Delta$ radians. A line has been drawn on these figures to separate the two regions since the true physical meaning of the poles corresponding to eigenvalues with negative real components is not clear for rectangular geometries (although it was conjectured that these poles have no meaning for the wire problem). A sensible method to test the validity of the poles in both regions is to reduce the value of $c\Delta t$ below the initial choice of 0.7Δ and note shifts in the pole positions. For true poles, we suspect very little shift. It was experimentally observed that the lower set shifted only slightly, but the upper set experienced a considerable shift. Hence from this argument, we conjecture that only the lower set represents true system poles.

The lower pole cluster agrees reasonably well with the frequency-domain results. The lowest order pole from Figure 6.12 (12 unknowns) is explicitly $-0.284 + j0.715$; this pole was found by frequency-domain methods to be $-0.272 - j0.675$. The time-domain result should approach this (up to the similarity of the models used in each domain) as the number of

unknowns is increased. Figure 6.13 compares selected time-domain poles with available frequency-domain poles.

It is interesting to note that double poles were observed for the square plate, and a fill in of poles occurred as the number of unknowns increased. Both of these can be justified by considering the poles of an infinite rectangular waveguide.

The simultaneous iteration method presented in Chapter 4 may be used to obtain the natural frequencies and modes for the rectangular plate. Care is required in its implementation, however, due to the absence of the well defined layering structure which appeared with the wire problem.

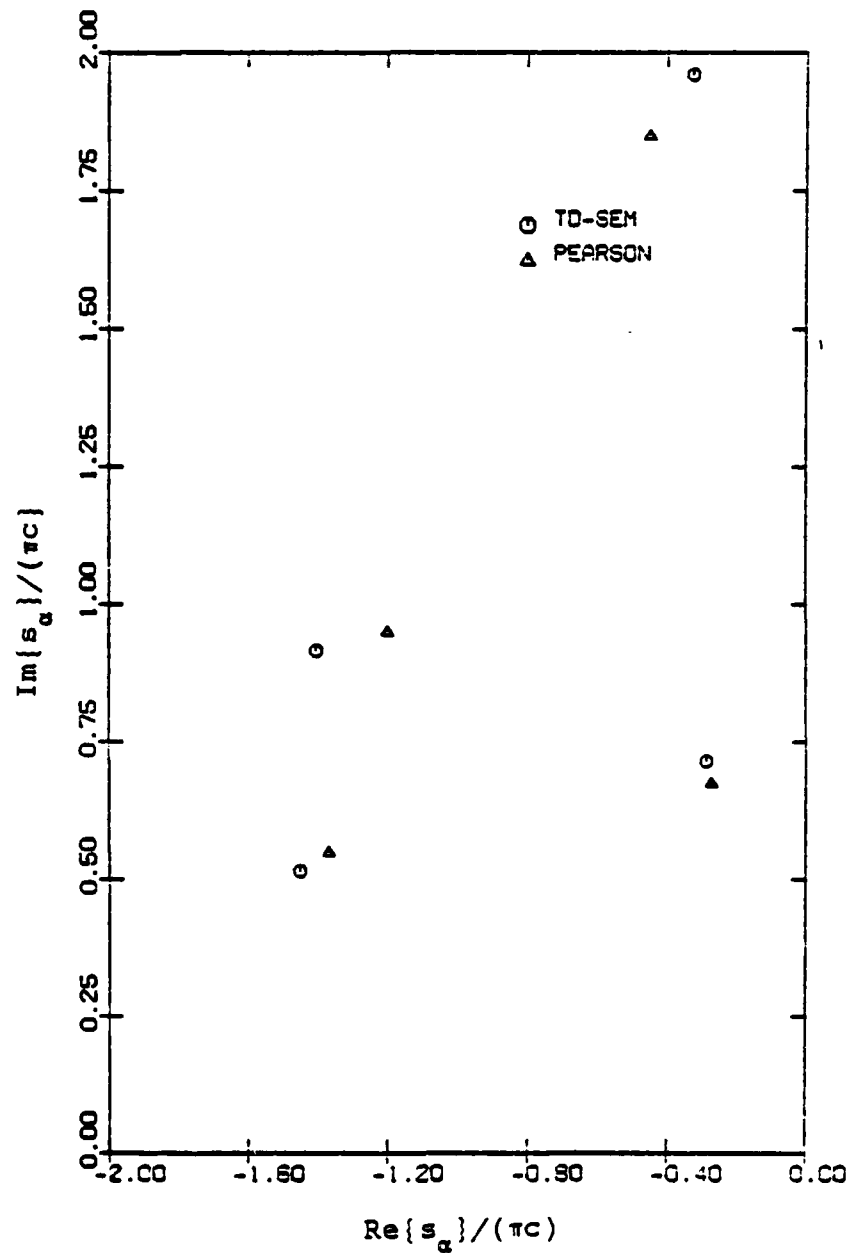


Figure 6.13: Comparison of TD-SEM poles (shifted grid, 12 patches for each current density component, and $c\Delta t=0.7\Delta$) with available frequency-domain poles. The results are for a 1 meter square plate.

Chapter VII

CONCLUSIONS

In this thesis, the fundamental integral equations of electromagnetic theory and the theoretical foundations of both the frequency-domain SEM and the time-domain SEM method of Cordaro and Davis were developed. It was observed from the development of TD-SEM that special sparse eigensolution routines were required to determine the eigenvalues of the transition matrix due to the excessive high speed storage requirements associated with certain problems. A modified simultaneous iteration algorithm was developed to satisfy this eigensolution requirement. The algorithm may be used to obtain partial pole solutions for a variety of geometries, and was explicitly shown to be effective on the thin-wire problem for an arbitrary number of unknowns.

Root searching methods which take advantage of the companion form of the transition matrix, such as Muller's method and the polynomial matrix reduction method of Woolivich, were found to be effective methods for obtaining the natural frequencies only for linear geometries discretized with relatively few unknowns. The contour integration technique of Singaraju, Giri, and Baum, which also takes advantage of this companion form, was not explicitly tested in this stu-

dy; however, the method may prove to be effective for problems discretized with a large number of unknowns provided the required integration operation can beneficially be used to numerically smooth the determinate evaluation. Further study is required to establish the utility of this method.

Time-domain techniques which provide convenient matrix methods for obtaining the SEM coupling coefficients have been developed. The time-domain form of these coefficients is much simpler than the equivalent frequency-domain form.

The effect of altering the sub-sectional coupling between unknowns in the numerical formulation of the thin-wire problem was also investigated. No relation between the specific layering structure of the poles and sub-matrices of the transition matrix was observed. This was unfortunate since it was hoped that if only a particular subset of the pole distribution was desired, then sub-matrices which did not influence this subset could be removed from the transition matrix and thereby yield a lower order problem.

A shifted gridding scheme was applied to the rectangular plate problem to obtain transient solutions. This scheme was found to represent a more natural discretization for the problem than the unshifted or standard gridding scheme which is typically used. The shifted scheme was then used in conjunction with TD-SEM to obtain pole distributions for the

square, perfect conducting plate. The results obtained were found to be quite similar to available frequency-domain results.

Fourier and matrix stability methods were applied to the finite difference representations of electromagnetic equations. These methods were found to provide accurate insight into the required relation between the time and spatial sampling distances that will yield a numerically stable solution for an arbitrary difference formulation.

The physical significance of the additional poles generated by choosing the time sampling distance smaller than the spatial sampling distance or the spatial sampling distance to be different in different directions remains an open question. These additional poles are conjectured to be false poles for which an elimination procedure has been presented.

REFERENCES

1. Baum, C. E., 'On the singularity expansion method for the solution of electromagnetic interaction problems,' Interaction Note 88, Dec., 1971.
2. Marian, L. and Latham, R. W., 'Analytical properties of the field scattering by a perfect conducting, finite body,' Interaction Note 92, 1972, also IEEE Trans. Antennas Propagat., AP-21, p.809, 1973.
3. Ramm, A. G., 'Mathematical foundations of the singularity and eigenmode expansion methods (SEM and EEM),' J. Math. Analysis and Applications, 86, p.562, 1982.
4. Tesche, F. M., 'On the singularity expansion method as applied to electromagnetic scattering from thin-wires,' Interaction Note 102, April, 1972, also IEEE Trans. Antennas Propagat., AP-21, Jan., 1973.
5. Baum, C. E., 'The singularity expansion method,' in Transient Electromagnetic Fields, chapter 3, Ed., Felsen, L. B., Springer-Verlag, Berlin, New York, 1976.
6. Van Blaricum, M. L., and Mittra, R., 'A technique for extracting the poles and residues of a system directly from its transient response,' Interaction Note 245, Feb., 1975.
7. Prony, R., 'Essai experimental et analytique, etc,' Paris J. l'Ecole Polytechnique, 1, cahier 2, 24, 1975.
8. Cordaro, J. T., and Davis, W. A., 'Time-domain techniques in the singularity expansion method,' IEEE Trans. Antennas Propagat., AP-29, p.543, May, 1981.
9. Poggio, A.J., and Miller, E.K., 'Integral equation solutions for three-dimensional scattering problems,' in Computer Techniques for Electromagnetics, chapter 4, Ed., Mittra, R., Pergamon Press, New York, 1973.
10. Stratton, J. A., Electromagnetic Theory, McGraw-Hill, New York, 1941.
11. Tei, C.T., Dyadic Green's Functions in Electromagnetic Theory, Intext Educational Publishers, Scranton, Pennsylvania, 1971.

12. Davis, W. A., Numerical Solutions to the Problems of Electromagnetic Radiation and Scattering by a Finite Hollow Cylinder, University of Illinois, Urbana, Illinois, 1974.
13. Hadamard, J., Lectures on Cauchy's Problem in Linear Partial Differential Equations, Dover Publications, New York, 1952.
14. Harrington, R.F., Field Computation by Moment Methods, Macmillan, New York, 1968.
15. Singaraju, B.K., Giri, D.V., and Baum, C. E., 'Further developments in the application of contour integration to the evaluation of the zeros of analytic functions and relevant computer programs,' Interaction Note 42, March, 1976.
16. Mittra, R., 'Integral equation methods for transient scattering,' in Transient Electromagnetic Fields, chapter 2, Ed., Felsen, L. B., Springer-Verlag, Berlin, New York, 1976.
17. Ames, W. F., Numerical Methods for Partial Differential Equations, Academic Press, New York, 1977.
18. Cordaro, J. T., Personal Communication, Oct., 1979.
19. Wilkinson, J. H., The Algebraic Eigenvalue Problem, Oxford University Press, Oxford, 1965.
20. Parlett, B., 'Applications of Laguerre's method to the matrix eigenvalue problem,' Tech. Report 21, Appl. Math. and Stat. Lab., Stanford Univ., 1962.
21. Stewart, G. W., 'The numerical treatment of large eigenvalue problems,' IFIP, 74, p.666, 1974.
22. Muller, D. E., 'A method for solving algebraic equations using an automatic computer,' MTAC, 10, p.208, 1956.
23. Woolivich, W. A., Linear Multivariable Systems, Springer-Verlag, New York, 1974.
24. Fulkerson, D., and Wolfe, P., 'An algorithm for scaling matrices,' SIAM Review, 4, 3, p.142, 1962.
25. Kelly, L. G., Handbook of Numerical Methods and Applications, Addison-Wesley, Reading, Mass., 1967.

26. Herstein, I. N., Topics in Algebra, Xerox, Lexington, Mass., Toronto, 1975.
27. Rutishauser, H., 'Solution of eigenvalue problems with the LR transformation,' Nat. Bur. Standards Appl. Math. Ser., 49, p.47, 1958.
28. Francis, J. G. F., 'The QR transformation, parts I and II,' Computer J., 4, p.265-271 and p.332-345, 1961, 1962.
29. Jennings, A., Matrix Computation for Engineers and Scientists, Wiley, Chichester, New York, Brisbane, Toronto, 1977.
30. Wilkinson, J. H., and Reinsch, C., Linear Algebra, Volume II, Springer-Verlag, New York, Heidelberg, Berlin, 1971.
31. Bauer, F. L., 'Das verfahren der treppeniteration und verwandte verfahren zur losung algebraischer eigenwert-probleme,' ZAMP, 8, p.214, 1957.
32. Rutishauser, H., 'Computational aspects of F. L. Bauer's simultaneous iteration method,' Numerical Math., 13, p.4, 1969.
33. Clint, M., and Jennings, A., 'A simultaneous iteration method for the unsymmetric eigenvalue problem,' J. Inst. Maths. Applics., 8, p.111, 1971.
34. Jennings, A., and Stewart, W. J., 'Simultaneous iteration for partial eigensolution of real matrices,' J. Inst. Maths. Applics., 15, p.351, 1975.
35. King, R. W. P., The Theory of Linear Antennas, Harvard University Press, Cambridge, Mass., 1956.
36. Poggio, A. J., and Mayes, P. E., 'Numerical solution of integral equations for dipole and slot antennas including active and passive loading,' Tech. Report AFAL-TR-69-180, Air Force Avionics Laboratory, Wright-Patterson AFB, Ohio, 1969.
37. Thiele, G. A., 'Wire antennas, in Computer Techniques for Electromagnetics, chapter 2, Ed., Mittra, R., Pergamon Press, New York, 1973.

38. Mittra, R., Numerical and Asymptotic Techniques in Electromagnetics, Springer-Verlag, Berlin, New York, 1975.
39. King, R. W. P., 'Cylindrical antennas and arrays,' in Antenna Theory, Part 1, chapter 9, Ed., Collin, R. E., and Zucker, F. J., McGraw-Hill, New York, 1969.
40. Popovic, B. D., Dragovic, M. B., Djordjevic, A. R., Analysis and Synthesis of Wire-Antenna Structures, Research Studies Press, Chichester, England, 1982.
41. Born, M., and Wolf, E., Principles of Optics, Pergamon Press, New York, 1964.
42. Davis, W. A., Itoh, T., Mittra, R., 'Electromagnetic pulse scattering from hollow cylinders and half-planes,' Interaction Note 97, March, 1972.
43. Bennett, C. L., Menger, K. S., Hieronymus, R., De Lorenzo, J., Peterson, D., and Maloy, C., 'Space time integral equation approach for targets with edges,' Sperry Res. Center, Tech. Rep. SCRC-CR-74-3, 1974.
44. Pearson, L. W., and Mittra, R., 'The singularity expansion representation of the transient electromagnetic coupling through a rectangular aperture,' Interaction Note 296, June, 1976.
45. Glisson, A. W., and Wilton, D. R., 'Simple and efficient numerical methods for problems of electromagnetic radiation and scattering from surfaces,' IEEE Trans. Antennas Propagat., AP-28, p.593, 1980.

END

FILMED

7-83

DTIC